

INFORMATION TO USERS

This manuscript has been reproduced from the microfilm master. UMI films the text directly from the original or copy submitted. Thus, some thesis and dissertation copies are in typewriter face, while others may be from any type of computer printer.

The quality of this reproduction is dependent upon the quality of the copy submitted. Broken or indistinct print, colored or poor quality illustrations and photographs, print bleedthrough, substandard margins, and improper alignment can adversely affect reproduction.

In the unlikely event that the author did not send UMI a complete manuscript and there are missing pages, these will be noted. Also, if unauthorized copyright material had to be removed, a note will indicate the deletion.

Oversize materials (e.g., maps, drawings, charts) are reproduced by sectioning the original, beginning at the upper left-hand corner and continuing from left to right in equal sections with small overlaps. Each original is also photographed in one exposure and is included in reduced form at the back of the book.

Photographs included in the original manuscript have been reproduced xerographically in this copy. Higher quality 6" x 9" black and white photographic prints are available for any photographs or illustrations appearing in this copy for an additional charge. Contact UMI directly to order.

UMI

**A Bell & Howell Information Company
300 North Zeeb Road, Ann Arbor MI 48106-1346 USA
313/761-4700 800/521-0600**

MILLIMETER-WAVE POLARIMETRY OF STAR FORMATION REGIONS
AND EVOLVED STARS

by
Jason Glenn

A Dissertation Submitted to the Faculty of the
DEPARTMENT OF ASTRONOMY
In Partial Fulfillment of the Requirements
For the Degree of
DOCTOR OF PHILOSOPHY
In the Graduate College
THE UNIVERSITY OF ARIZONA

1 9 9 7

UMI Number: 9806828

UMI Microform 9806828
Copyright 1997, by UMI Company. All rights reserved.

**This microform edition is protected against unauthorized
copying under Title 17, United States Code.**

UMI
300 North Zeeb Road
Ann Arbor, MI 48103

THE UNIVERSITY OF ARIZONA ®
GRADUATE COLLEGE

As members of the Final Examination Committee, we certify that we have
read the dissertation prepared by Jason Glenn

entitled Millimeter-Wave Polarimetry of Star Formation
Regions and Evolved Stars

and recommend that it be accepted as fulfilling the dissertation
requirement for the Degree of Doctor of Philosophy

<u>Christopher K. Walker</u> Christopher K. Walker	<u>6/24/97</u> Date
<u>Erick T. Young</u> Erick T. Young	<u>6/24/97</u> Date
<u>John H. Biegging</u> John H. Biegging	<u>6/24/97</u> Date
<u>Gary D. Schmidt</u> Gary D. Schmidt	<u>6/24/97</u> Date
_____	_____
	Date

Final approval and acceptance of this dissertation is contingent upon
the candidate's submission of the final copy of the dissertation to the
Graduate College.

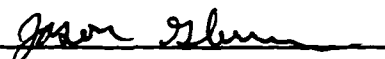
I hereby certify that I have read this dissertation prepared under my
direction and recommend that it be accepted as fulfilling the dissertation
requirement.

<u>Christopher K. Walker</u> Dissertation Director Christopher K. Walker	<u>6/24/97</u> Date
--	------------------------

STATEMENT BY AUTHOR

This dissertation has been submitted in partial fulfillment of requirements for an advanced degree at The University of Arizona and is deposited in the University Library to be made available to borrowers under rules of the Library.

Brief quotations from this dissertation are allowable without special permission, provided that accurate acknowledgment of source is made. Requests for permission for extended quotation from or reproduction of this manuscript in whole or in part may be granted by the head of the major department or the Dean of the Graduate College when in his or her judgment the proposed use of the material is in the interests of scholarship. In all other instances, however, permission must be obtained from the author.

SIGNED: 

ACKNOWLEDGMENTS

There are many people who have contributed to this thesis by sharing their ideas and wisdom. My advisers are at the top of this list. I thank Chris Walker for a constant flow of ideas and encouragement. I am grateful to Erick Young for sharing his infinite technical knowledge. Gary Schmidt has been a role model of efficiency and critical thinking. I thank John Bieging for serving on my committee and critical comments on this dissertation.

Chapters 2 and 7 of this dissertation contain sections from an International Journal of Infrared and Millimeter Waves paper (1997, 18, 285) on which Chris Walker and Erick Young were coauthors. Chris Walker and Phil Jewell were coauthors on the Astrophysical Journal paper (1997 ApJ 479 325) that is incorporated in Chapters 3 and 5. Chris Walker, John Bieging and Phil Jewell are coauthors on the paper to be published in the Astrophysical Journal Letters (in press) that is Chapter 6.

Chad Engelbracht, Craig Kulesa, Aimee Hungerford, and Greg Rudnick generously helped me make observations with Cyclops. I thank the staff of the Heinrich Hertz Telescope, including Bob Martin, Joe McMullin, Bob Hayward, Doug Officer, Dave Ashby, Dirk Muders, and John Casas for their support during the installation and testing of Cyclops. The HHT is a facility jointly operated by the University of Arizona and the Max-Planck-Institut für Radioastronomie.

I would like to thank Dan Clemens and Richard Barvainis for useful discussions regarding Rexolite waveplates. Thanks also go to Richard Chamberlain and Jeff Kingsley for useful discussions about fabricating aluminum mirrors. Jeff Capara, Ivan Lanum, Mike Orr, and Jim Izlar taught me some practical aspects of mechanical design.

I also thank Hua Chen and Gopal Narayanan for many helpful discussions about star formation, and the referee for useful comments on the protostellar outflow spectropolarimetry paper. I gratefully acknowledge Darren Dowell, David Schleuning, and Roger Hildebrand for making their DR 21 polarimetry available to me in advance of publication. I thank the staff of the NRAO 12 meter telescope for observing support, especially Phil Jewell and Darrel Emerson for helpful discussions. The National Radio Astronomy Observatory is a facility of the National Science Foundation, operated under cooperative agreement by Associated Universities, Inc.

I thank NASA for the GSRP fellowship NGT-51328 that made the timely completion of this dissertation possible.

DEDICATION

I dedicate this dissertation to Meredith for teaching me equilibrium.

TABLE OF CONTENTS

LIST OF FIGURES	9
LIST OF TABLES	11
ABSTRACT	12
1 INTRODUCTION	14
1.1 Why Study Magnetic Fields in Molecular Clouds and Stellar Envelopes?	14
1.2 Dust Emission Polarization Mechanism and the State of Observations	16
1.3 Millimeter-Wave Molecular Emission Line Polarization Mechanism and the State of Observations	20
2 CYCLOPS: A SINGLE BEAM 1.3 MM POLARIMETER	24
2.1 Introduction	24
2.2 Instrument Design	25
2.3 Polarization Modulator and Analyzer	26
2.4 Observations, Data Acquisition, and Data Analysis	27
2.4.1 Performance	30
2.4.2 Observations at the HHT	31
2.5 Improved Observing Scheme	35
2.6 Conclusion	37
3 DUST CONTINUUM POLARIMETRY OF DR 21	39
3.1 Introduction	39
3.2 Observations and Calibrations	40
3.2.1 $\lambda = 1.3$ mm Observations	40
3.2.2 $\lambda = 2$ mm Observations	40
3.3 Discussion	42
3.3.1 Spatial Structure	42

3.3.2	Wavelength Dependence	49
3.3.3	Magnetic Field Strength	51
3.4	Summary	55
4	DUST CONTINUUM POLARIMETRY SURVEY OF STAR FORMATION REGIONS	57
4.1	Introduction	57
4.2	Observations and Calibrations	58
4.3	Discussion	60
4.3.1	Interpreting Dust Polarimetry: The Effects of Large Optical Depths	62
4.3.2	NGC1333 IRAS4A	63
4.3.3	Polarization Position Angles and Molecular Outflows	64
4.3.4	Polarization Position Angles and Cloud Core Elongations	68
4.3.5	Polarization Percentages and Cloud Core Elongations	75
4.3.6	Distribution of Polarization Position Angles in the Plane of the Galaxy	76
4.3.7	Distribution of Polarization Percentages	79
4.4	Summary	82
5	HCO ⁺ AND CS SPECTROPOLARIMETRY OF MOLECULAR OUTFLOWS FROM PROTOSTARS	84
5.1	Introduction	84
5.2	Observations and Calibrations	86
5.3	Results	87
5.4	Discussion	92
5.4.1	The Lack of Emission Line Polarization	92
5.4.2	Magnetic Field Strength in DR 21	98
5.5	Summary	99

6	MILLIMETER-WAVE SPECTROPOLARIMETRY OF EVOLVED STARS: EVIDENCE FOR POLARIZED MOLECULAR LINE EMISSION	101
6.1	Introduction	101
6.2	Observations and Data Analysis	103
6.3	Discussion	110
6.4	Summary	116
7	CONCLUSIONS AND FUTURE WORK	118
7.1	Conclusions	118
7.2	Questions That Remain and Strategies to Answer Them	120
7.3	Cyclops Upgrade	123
7.3.1	Continuous Waveplate Rotation	123
7.3.2	800 μm to 1300 μm Achromatic Rexolite Half-Waveplate . . .	124
	APPENDIX A. MIRROR FABRICATION	128
A.1	Motivation	128
A.2	Materials	128
A.3	Reflective Surface Shape Derivation and CNC Program	129
A.4	Testing	133
A.5	Conclusion	136
	REFERENCES	138

LIST OF FIGURES

2.1	A schematic of the major components of the 1.3 mm polarimeter. . .	28
2.2	Systematic polarization measured by observing Jupiter.	33
3.1	1.3 mm linear polarization map of DR 21.	45
3.2	Radial dependence of the DR 21 polarization.	47
3.3	Continuum polarization as a function of beam size.	48
3.4	Continuum polarimetry of DR 21 as a function of wavelength.	52
4.1	Wavelength dependence of the NGC1333 IRAS 4A linear polarization. . .	65
4.2	Cumulative distribution of the difference between cloud core elongation angles and polarization position angles.	73
4.3	Percentage polarization versus cloud elongation.	77
4.4	Distribution of the difference between the polarization position angles and the local normals to the Galactic plane.	80
4.5	800 μm and 1.1-1.3 mm percentage polarization histograms.	81
5.1	$\text{HCO}^+ J = 1-0$ (89.188518 GHz) spectropolarimetry toward the southwestern outflow lobe of DR 21.	89
5.2	$\text{HCO}^+ J = 1-0$ spectropolarimetry of Mon R2.	90
5.3	$\text{CS } J = 2-1$ spectropolarimetry of IRAS16293-2422.	91
6.1	$\text{CS } J = 2-1$ spectropolarimetry of IRC+10216.	108
6.2	$\text{HCN } J = 1-0$ spectropolarimetry of CRL 2688.	111
6.3	$\text{CS } J = 2-1$ spectropolarimetry of CRL 2688.	112
7.1	Composite Rexolite half-waveplate retardation.	126
A.1	Setup of the blank on the mill.	131
A.2	Schematic for calculating the path of the endmill.	132

A.3 Schematic for calculating the step distance of the mill.	134
--	-----

LIST OF TABLES

2.1	Instrument Parameters	36
2.2	Sample of Observations	36
3.1	Cyclops 1.3 mm Polarimetry of DR 21	44
3.2	Continuum Polarimetry of DR 21	44
4.1	Cyclops 1.3 mm Polarimetry Survey	59
4.2	Continuum Polarimetry from the Literature	61
4.3	Cloud Core Elongation Angles	70
5.1	Outflow Spectropolarimetry	88
6.1	Instrumental Polarization	106
6.2	Observations of Evolved Stars	106
A.1	Mirror Test Results	137

ABSTRACT

A new $\lambda = 1.3$ mm polarimeter, Cyclops, was constructed to make observations of dust continuum emission from star formation regions. The polarization of the inner arcminute of DR 21 was mapped with Cyclops. The polarization percentage and position angle are remarkably constant, indicating a uniform magnetic field throughout the cloud. Turbulent gas motions are a more significant source of support against self gravity in the cloud core than thermal pressure or magnetic fields. The polarization toward the cloud core increases slightly from $\lambda = 100 \mu\text{m}$ to $\lambda = 2$ mm and is consistent with the standard dust composition of silicates and graphite.

A small continuum polarization survey of cloud cores with embedded protostars was made with Cyclops and combined with observations from the literature. There is no clear tendency for any preferred alignment of cloud core elongations with respect to magnetic field lines, especially for the bright, high mass star forming regions. This confirms that the massive cloud cores are magnetically supercritical. The magnetic field lines appear randomly oriented with respect to the local Galactic plane position angles, implying that the random component of the Galactic magnetic field dominates the spiral component in this sample.

Three- σ upper limits of 0.4%, 1.2%, and 1.2% were placed on the polarization of the HCO^+ $J = 1-0$ emission line from the DR 21 and Mon R2 molecular outflows, and the CS $J = 2-1$ line from the IRAS 16293-2422 molecular outflow, respectively. These polarizations are an order of magnitude lower than predicted by theoretical models. In the case of DR 21, the lack of polarization is probably due to a disordered magnetic field in clumpy, turbulent gas, although multiple

scattering may also diminish the polarization.

CS $J = 2-1$ polarizations of $0.9\% \pm 0.1\%$ and $5.1\% \pm 1.5\%$ were observed from the envelopes of the evolved stars IRC+10216 and CRL 2688, respectively. An anisotropic optical depth to escape of infrared photons from the central star, perhaps caused by a toroidal dust distribution, could generate the IRC+10216 polarization.

CHAPTER 1

INTRODUCTION

Polarimetry is an observational tool that allows us to probe asymmetries in radiative transfer. In the interstellar medium and stellar atmospheres, magnetic fields introduce asymmetry by providing preferred axes for dust grain rotation and splitting energy levels of atoms and molecules. Consequently, it is possible to measure magnetic fields using polarimetry. In this thesis I report polarimetry of millimeter-wave thermal dust emission from molecular clouds undergoing star formation. I also report spectropolarimetry of millimeter-wave molecular line emission from protostellar outflows and the extended atmospheres of evolved stars. The purpose of these observations is to analyze the role of magnetic fields in these objects.

1.1. Why Study Magnetic Fields in Molecular Clouds and Stellar Envelopes?

Why study magnetic fields in molecular clouds? Theories of star formation suggest that magnetic fields may play an important role in cloud collapse, angular

momentum transport, and the generation of outflows (e.g., Mouschovias 1976, Basu and Mouschovias 1995, Nakajima and Hanawa 1996). In particular, star formation theory (reviewed by Shu, Adams, and Lizano 1987) suggests that star formation is bimodal. In the case of low mass, subcritical star formation, self gravity is weak enough that magnetic field lines retain their structure in the initial phase of infall. Collapse proceeds by ambipolar diffusion, in which neutrals slip by the ions that are tied to magnetic field lines. Thus, magnetic field line geometries may affect the shapes of cloud cores. In high mass star formation, theory predicts that collapse is supercritical and self gravity overwhelms support provided by magnetic fields. Hence, magnetic field lines have little effect on cloud collapse and are entrained in infalling material.

Numerical simulations of isolated star formation incorporating magnetic fields suggest that large (100-1000 AU) psuedo-disks form (Galli & Shu 1993). The principal axes of these disks are parallel to the assumed uniform magnetic field lines in the parent cloud. Simulations of smaller size scales incorporate magnetic fields to channel material and angular momentum from accretion disks to molecular outflows (Pudritz and Norman 1986, Shu et al. 1988, Shu et al. 1994). These theories can be tested by observing magnetic field line geometries and comparing them to cloud core elongations and outflow orientations.

Why study magnetic fields in extended stellar atmospheres? Except for the well studied cases of the Sun, magnetic white dwarfs, pulsars, and interacting binaries, there are few observations of magnetic fields in stellar atmospheres. It is quite possible that magnetic fields play a small role in the evolution of most stars after they begin their main sequence lives, but this remains to be tested by observations.

1.2. Dust Emission Polarization Mechanism and the State of Observations

Dust grains¹ in dense molecular clouds are heated by radiation from protostars, embedded stars, and stars near the clouds. Grains cool by reemitting this radiation at wavelengths characteristic of their temperatures, similarly to blackbodies. For an ensemble of grains at a temperature T , the specific intensity emitted by the ensemble is given by a modified blackbody spectrum:

$$I_\nu(T) = B_\nu(T)(1 - e^{-\tau}), \quad (1.1)$$

where $B_\nu(T)$ is the Planck function and $\tau = (\nu/\nu_0)^\beta$ is the optical depth. ν_0 is the frequency at which the optical depth is 1, and $\beta \approx 2$ (Gordon 1995). For $\lambda \geq 200 \mu\text{m}$, τ is almost always much less than 1 (Hildebrand 1983). Since dust in cloud cores forming stars is typically heated to $\sim 50 \text{ K}$, the emission peaks at $\lambda \sim 100 \mu\text{m}$. Dust emission is usually brighter than bremsstrahlung emission to wavelengths as long as a few millimeters.

Dichroic absorption (selective absorption or scattering of one sense of linear polarization) of background starlight by dust in molecular clouds is observed in the optical and near infrared, and dichroic emission (selective emission of one sense of linear polarization) is observed in the far infrared. We know, therefore, that at least some dust grains are not spherical and are aligned. Hildebrand and Dragovan (1995) investigated grain shapes in the OMC-1 and AFGL 2591 clouds with $100 \mu\text{m}$

¹Dust grains have refractory cores containing silicates and graphite, and those in dense molecular clouds have icy mantles. The ice is composed of solid H_2O , CO_2 , and more complex species. Interstellar dust grain composition is reviewed by Sandford (1996) and the optical properties are reviewed by Draine (1996).

polarimetry and spectropolarimetry of the $9.7\ \mu\text{m}$ silicate resonance. They found that grains are typically oblate with an axial ratio of $2/3$. Despite the fact that many mechanisms have been proposed to align grains (e.g., Davis and Greenstein 1951, Gold 1951, Purcell 1979; many variations are reviewed by Roberge 1996), the alignment mechanism in dense clouds is not yet satisfactorily understood. This has little impact on far infrared polarimetric mapping of magnetic fields however, because the Barnett effect operates even if alignment efficiency is low. The Barnett effect endows spinning grains with a magnetization parallel to the spin axis, which is usually the principal axis of greatest moment of inertia (see, e.g., Roberge 1996). This causes the angular momenta of grains to precess about magnetic field lines. Therefore, the largest average projection of grains is orthogonal to magnetic field lines, and thermal radiation from dust is linearly polarized orthogonal to field lines. In the optically thin limit, to observe magnetic field line projections on the plane of the sky, one has only to observe the polarization of dust emission and rotate the position angle 90° .

The first detection of far infrared polarization was made by Cudlip et al. (1982) toward the Orion KL region. Since then a handful of polarimeters have been used both from ground based telescopes and the Kuiper Airborne Observatory, with wavelengths ranging from $\lambda = 60\ \mu\text{m}$ to $1.3\ \text{mm}$. (From here forward, far infrared refers to $\lambda \leq 100\ \mu\text{m}$, submillimeter refers to $100\ \mu\text{m} < \lambda < 1\ \text{mm}$, and millimeter refers $\lambda \geq 1\ \text{mm}$. Thermal dust emission refers to all three.) The evolution of the instrumentation is listed in Chapter 2.

The primary conclusions of dust emission polarimetry to date are:

1. The inferred magnetic field lines are much more ordered in dense molecular clouds than the magnetic field lines inferred from optical and near infrared

polarimetry of cloud peripheries (e.g., Goodman 1996, Vrba, Strom, and Strom 1976).

2. It has been possible to construct plausible three dimensional models of magnetic fields in a few regions by combining dust emission polarimetry and Zeeman observations (e.g., Hildebrand 1996 and Roberts et al. 1993 in the case of W3).
3. Dust emission polarization has been shown to decrease in the core of OMC-1 with respect to the immediate surroundings. This has been interpreted to mean that the field lines have been pinched in by gravitational collapse (Leach et al. 1991, Schleuning, Dowell, and Platt 1996).
4. Some constraints were placed on dust grain shapes and alignment efficiencies when far infrared observations were combined with near infrared polarimetry (Hildebrand and Dragovan 1995).
5. Kane et al. (1993) found weak evidence that projected magnetic field line position angles and cloud core elongation position angles derived from enhanced resolution IRAS maps are correlated.
6. In a small sample of inhomogenous data (including low and high mass star forming regions), there appears to be no obvious correlation between magnetic field line projections and molecular outflow orientations from protostars (Minchin, Bonifacio, and Murray 1996).
7. Greaves, Holland, and Ward-Thompson (1997) compiled a set of 800 μm polarization observations of seven Class 0 protostars to place constraints on magnetized outflow models. Class 0 protostars have bolometric luminosities that exceed their 1.3 mm luminosities by less than a factor of 20,000 and

consequently are presumably the youngest protostellar sources (André, Ward-Thompson, and Barsony 1993). Greaves, Holland, and Ward-Thompson report various correlations: the level of polarization is anticorrelated with the age of the protostars (and therefore magnetic fields are more ordered in younger protostars), polarization increases with distance to the protostar, which they suggest is a selection effect that actually implies magnetic fields are more ordered in more massive (brighter) sources, and finally that the difference in the angles between the outflows and the magnetic field lines are correlated with the angles the outflows make with the line of sight. The sense of this last correlation is that if the outflow is in the plane of the sky, the magnetic field tends to be perpendicular to the outflow, and if the outflow is nearly along the line of sight, the magnetic field tends to be parallel to the outflow. They can explain the angle correlation in the context of some theoretical models, but theories do not explain the other correlations. It should be noted that only four of the seven polarization detections are greater than 3σ , so the correlations should be considered with caution.

What needs to be done to improve our understanding of magnetic fields in cloud cores? A larger sample of magnetic field line observations will make it possible to better test for correlations with cloud properties, such as outflow orientations and cloud core elongations. With magnetic field line maps of cloud cores toward which magnetic field strength maps can be made from Zeeman observations, it will be possible to make three dimensional models of the magnetic fields. Resolving these issues completely is beyond the scope of this thesis, but the availability and large collecting area of the Heinrich Hertz Telescope make it possible to appreciably increase the number of polarization observations.

Why millimeter observations? Goodman et al. (1995) showed that because it is optically thin, thermal dust emission is the only way to reliably probe magnetic field lines in dense cloud cores ($A_V \sim 10$ or more). Interpolating from optical and near infrared observations on the cloud peripheries (e.g., Vrba, Strom, and Strom 1976, see the review by Goodman et al. 1996) is inadequate. Near infrared polarimetry has been very useful in studying the late stages of star formation, i.e., T Tauri stars (see Bastien 1996 for a recent review of this work), but is of less use for studying magnetic fields in deeply embedded objects. Further, submillimeter and millimeter observations are complementary to far infrared observations: polarization caused by dichroic absorption of aligned grains has been observed at $\lambda = 60 \mu\text{m}$ toward Sgr B2 (Dowell et al. 1996)!

1.3. Millimeter-Wave Molecular Emission Line

Polarization Mechanism and the State of Observations

Linear and circular polarization are produced in absorption and emission lines from molecules when a magnetic field is present to lift the degeneracy in the rotational levels². The splitting of energy levels of angular momentum J into sublevels m_J is given by $\Delta W = -\boldsymbol{\mu} \cdot \mathbf{B}$, where $\boldsymbol{\mu}$ is the magnetic moment of the molecule and \mathbf{B} is the magnetic field. The selection rules for electric dipole allowed rotational transitions are $\Delta J = \pm 1$ and $\Delta m = 0, \pm 1$. σ components arise from $\Delta m = 0$ transitions and are elliptically polarized (circularly polarized along the magnetic field and linearly polarized perpendicular to the magnetic field). π components

²Masers are another mechanism of millimeter-wave polarization, but they are not considered here because none were observed in this thesis.

arise from $\Delta m = \pm 1$ transitions and are linearly polarized. For small magnetic fields, the splitting between the σ components is proportional to the magnetic field strength. So, 15

observations of the splitting yield measures of the line of sight component of the magnetic field. In molecular clouds and the extended atmospheres of AGB stars, the line widths are typically of order one and a few tens of kilometers per second, respectively. A magnetic field of $100 \mu\text{G}$ corresponds to a splitting of much less than a kilometer per second, so Zeeman splitting cannot be directly observed in millimeter transitions.

Several models have been developed, however, that predict linear polarization from molecular rotational emission lines when the magnetic sublevels, m_J , are differentially populated. If the spatial separation of regions of differential population is large enough to resolve with a millimeter-wave telescope, polarization can be observed. This is useful since the polarization position angles should be related to the projections of the magnetic field lines on the plane of the sky.

Of the three models that have been developed, two were intended for stellar atmospheres and one is more appropriate for molecular clouds. Goldreich and Kylafis (1981, 1982) developed a model of polarized emission from molecules in stellar winds, however this model could also apply to outflows from protostars. They assumed a large velocity gradient (LVG) and used the Sobolev treatment. The detailed assumptions of this and the other two models are discussed in Chapter 5. In the model, the slow, smooth gradient of the stellar wind velocity causes the optical depth of each m_J sublevel to depend on the radial distance from the star. Therefore, the observed excitation of the sublevels, and consequently the net polarization observed, depends on the radial distance of the observation from

the central star. Only a simple, hypothetical, two J -level molecule was considered. Polarizations of up to 15% were predicted for the optimum optical depth of ~ 1 . Deguchi and Watson (1985) extended the calculation to a multilevel molecule and found that polarizations of up to 7% could be observed.

Lis et al. (1988) abandoned the LVG model and instead assumed a slow, smooth excitation gradient to produce differential population of m_J sublevels. This model is most appropriate for molecular clouds with a temperature or density gradient. Either no magnetic field or a radial magnetic field was assumed. Polarization was predicted to be maximum for small optical depths and for molecules with large permanent dipole moments. Large dipole moments ensure that the radiative decay rates exceed the collisional deexcitation rates.

Morris, Lucas, and Omont (1985) tailored their model to AGB stars with a compact, infrared-emitting central star surrounded by an extended molecular envelope. In this scheme, the infrared photons propagate radially outward from the center and excite molecules, which then emit vibrational and rotational transition lines. The infrared photons, since they are propagating radially from the central star, always deposit angular momenta with radial vectors to molecules. Therefore, there are preferred rotation axes for excited molecules in the envelope. Since the polarization should be symmetric about the central star, to observe polarization the telescope beam should be offset from the central star. Polarizations of up to 5% are predicted for beams with angular diameters small compared to the envelope.

Other investigators have searched for polarization in molecular clouds and the envelope of IRC+10216. They did not make any detections and the upper limits were $\sim 1\%$ or more. These surveys are discussed in Chapters 5 and 6.

New observations made to detect line polarization are reported in this thesis.

Millimeter receiver technology has improved significantly in the last decade. Noise temperatures are a factor of a few lower than when the previous observations were made and consequently it is now possible to achieve polarization uncertainties as low as 0.1% for bright objects. Further, before this thesis polarization had not been searched for toward protostellar outflows or toward evolved stars in transitions of molecules with high dipole moments.

The design and testing of Cyclops, a polarimeter constructed to observe thermal dust emission from molecular clouds, are described in Chapter 2. Observations and analysis of polarization from star forming regions made with Cyclops are presented in Chapters 3 and 4. In Chapters 5 and 6, the observations and analysis of a small survey of millimeter line polarization toward protostellar outflows and evolved stars is presented. These observations were made at the NRAO 12 m telescope with the facility polarimeter. In Chapter 7 the results of the thesis are summarized, some remaining questions and strategies to address them are listed, and improvements to Cyclops are suggested. Appendix A describes a process to fabricate ellipsoidal aluminum mirrors for submillimeter and millimeter applications. Ellipsoidal mirrors fabricated with this process were used to test Cyclops.

CHAPTER 2

CYCLOPS: A SINGLE BEAM 1.3 MM POLARIMETER

2.1. Introduction

The single channel 1.3 mm polarimeter, Cyclops, has been constructed to be used on the HHT. The combination of a 10 m aperture, very accurate surface, and high elevation (3178 m) make the HHT well suited for submillimeter and millimeter polarimetry. Cyclops will perform observations complementary to other polarimeters operating at shorter wavelengths.

The scientific purpose of this instrument is to observe magnetic fields in molecular clouds within the Milky Way Galaxy. Dust grains heated by starlight reemit thermal radiation in the far infrared, submillimeter, and millimeter portion of the electromagnetic spectrum. In the presence of ordered magnetic fields, the ensembles of dust grains in cloud cores emit polarized radiation which is perpendicular to the magnetic field (Hildebrand 1988). Polarimetry reveals the

projections of the magnetic fields on the plane of the sky. Understanding magnetic fields is important for theories of star formation and molecular cloud dynamics because magnetic support may be an important component of the total pressure in many clouds (Mouschovias 1976, Shu, Adams, & Lizano 1987).

Our design and techniques were significantly influenced by the designs and successes of previous polarimeters. The first detection of submillimeter polarization was by Cudlip et al. (1982) using a balloon borne instrument with a broad bandpass of 40-350 μm . Since that detection the instrumentation and techniques of submillimeter polarimetry have matured considerably. Hildebrand, Dragovan, and Novak (1984) used a dual polarization polarimeter aboard the Kuiper Airborne Observatory (KAO). Increasingly complex polarimeters have flown aboard the KAO, culminating in dual polarization arrays of bolometers. That work (Dragovan 1986, Novak et al. 1989, Gonatas et al. 1989, Platt et al. 1991, Platt et al. 1995) has resulted in a much improved understanding of submillimeter polarization systematics and cures. Submillimeter and millimeter polarimetry has also been successful from ground based telescopes. Polarimetric observations with heterodyne receivers include Barvainis and Predmore (1984), Novak, Predmore, and Goldsmith (1990), Barvainis, Clemens, and Leach (1988), and Clemens et al. (1990). Submillimeter polarimeters with broadband bolometers have also been operated from ground based telescopes (Flett & Murray 1991, Scheuning et al. 1996).

2.2. Instrument Design

The technical goal of Cyclops is to observe celestial sources with flux densities of $\gtrsim 5$ Jy within the 33" FWHM beam of the HHT to a polarization sensitivity of $\sim 0.25\%$ (1σ) at the rate of a few per day. There are several constraints on the

design of Cyclops. The HHT has an $f/13.8$ Nasmyth focus, and the physical size of the beam requires large optics: the waveplate must be nearly 10 cm in diameter. Also, the waveplate and wire grid have to operate at room temperature. Finally, the polarimeter should have stand alone hardware control and data acquisition, and be a slave to the telescope such that clock signals from the telescope control the states of the polarimeter.

A schematic of the polarimeter is presented in Figure 2.1. It consists of a rotating half-waveplate for polarization modulation and a parallel wire grid as a polarization analyzer. The HHT facility ^3He cooled (300 mK) bolometer was used for the observations. A 60 GHz bandpass centered at 1.3 mm is produced by a single mode waveguide and a low-pass filter (Kreysa 1996). Inside the dewar, the radiation is concentrated by a conical horn. A dedicated computer and additional electronics provide hardware control, data acquisition, and data analysis.

2.3. Polarization Modulator and Analyzer

The sheer size of the beam dictates that the waveplate should be made of an inexpensive material. Rexolite is a cross-linked polystyrene and not intrinsically birefringent. However, parallel grooves cut in the Rexolite create different dielectric constants for electric fields parallel to and perpendicular to the grooves. With grooves of the appropriate depth, a $\lambda/2$ retardation can be generated to produce a half-waveplate. Barvainis (1984) and Kirschbaum and Chen (1957) derived formulas for groove depth as a function of wavelength to make waveplates. Rexolite has a dielectric constant of 2.51, so at $\lambda = 1.3$ mm a groove depth of 5.0 mm yields a π retardation. The groove width (and spacing) must be $\leq \lambda/3$ so that the DC approximation is valid for calculating the dielectric constants. The groove spacing

and width of our half-waveplate are both 0.36 mm.

The wire grid polarization analyzer consists of parallel 25 μm diameter, gold-coated tungsten wires with an inter-wire spacing of 90 μm . This wire configuration provides a maximum polarization efficiency (observed polarization of a 100% polarized source) of 99% (Lesurf 1990).

Rotating the half-waveplate rotates the sense of the incoming linear polarization at four times the plate rotation rate. The wire grid analyzes the polarization by reflecting one sense of polarization (with the electric vector parallel to the wires) out of the optical path and transmitting the other sense to the detector. The equation for the radiation incident on the detector (neglecting losses) is given by

$$I = 0.5 I_0 \{1 - P \cos [4(\psi + \phi) + 2\delta] + P_{sys}(\psi, \delta)\}. \quad (2.1)$$

In this equation I is the flux density emerging from the wire grid, I_0 is the signal flux density, P is the linear polarization ($P = 1$ for 100% polarization), ψ is the fast axis position angle of the waveplate, δ is the constant phase offset of the waveplate, ϕ is the sum of the other phase offsets of the system (i.e., parallactic angle, elevation angle), and P_{sys} is the systematic polarization (a function of ψ and δ). The normalized Stokes parameters Q and U (e.g., Serkowski 1974) are derived from differences in I observed at four different angles ψ separated by $22^\circ 5$.

2.4. Observations, Data Acquisition, and Data Analysis

Hardware control, data acquisition, and data analysis are done with a dedicated personal computer. The waveplate is moved in 16 steps of $22^\circ 5$ per rotation

1.3 Millimeter Polarimeter

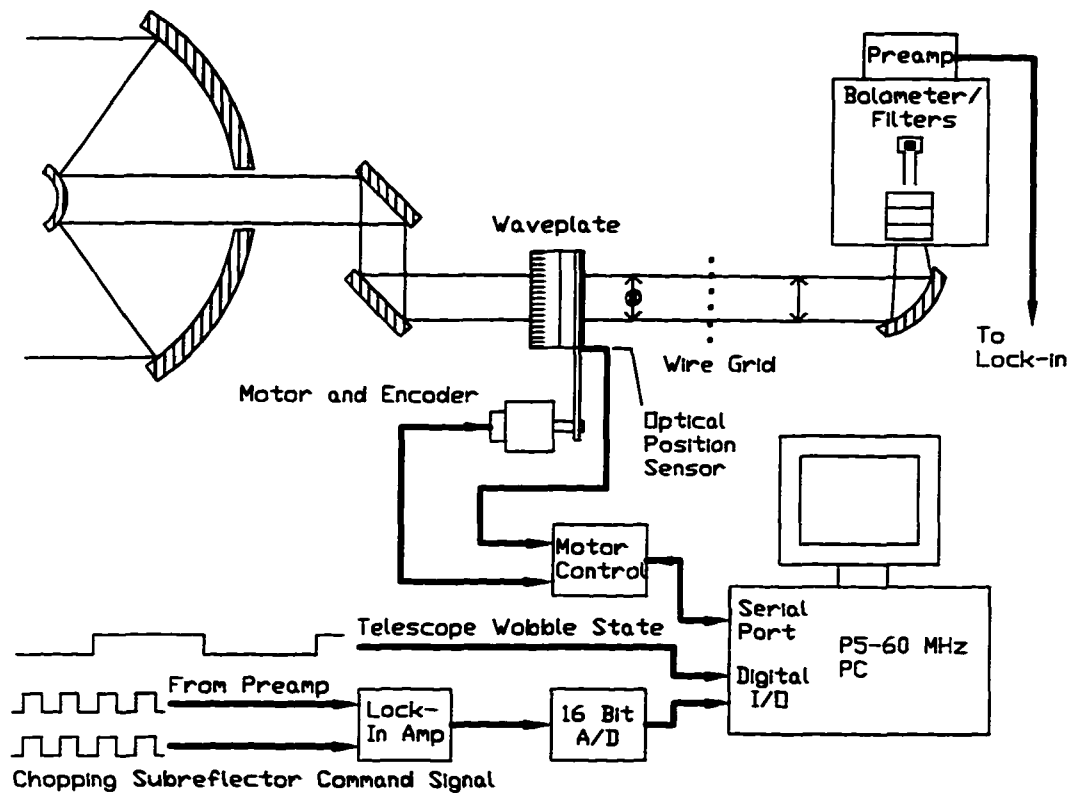


Figure 2.1 A schematic of the major components of the 1.3 mm polarimeter. Radiation is reflected from the telescope primary reflector to the secondary, tertiary, and quaternary mirrors of the Nasmyth focus telescope. The beam passes through the half-waveplate, then the wire grid, and only one sense of polarization is incident on the bolometer. The double-headed arrows in the beam denote polarization in the plane of the page and the circle circumscribing the x denotes polarization perpendicular to the plane of the page. The waveplate and wire grid operate at room temperature. After emerging from the preamp, the signal goes to a lock-in amplifier that multiplies it by the subreflector motion command signal. A 16 bit A/D digitizes the signal and the data are stored and analyzed with the computer. A stepper motor, which is controlled by an indexer and the computer, rotates the waveplate in 16 discrete steps per 360° revolution.

(sampling Q and U four times per rotation) by a stepper motor and timing belt. An optical encoder on the motor shaft and an independent optical switch mounted to the waveplate are used to ensure positional accuracy. The initial observing mode was one in which the secondary mirror of the HHT was continually chopping in azimuth at 5 Hz between the source and sky with a throw of $60''$ during each observation. The telescope was wobbled to place the source alternately in the positive and negative beams for alternating waveplate rotations, yielding a total throw of $\pm 120''$. Approximately 10 seconds were spent in each waveplate position giving a wobble period of 5–6 minutes. A new mode was used in all the observing runs following the initial engineering run. In this mode, the telescope was wobbled between the positive and negative positions for each position of the waveplate to eliminate sky noise more effectively.

After emerging from the preamplifier, the AC coupled bolometer signal is sent to a lock-in amplifier. The position command signal for the chopping secondary supplies the reference for the lock-in amplifier to enable background subtraction and noise rejection. The output signal from the lock-in amp is piped to a termination panel and into a 16 bit A/D board resident in the computer. For the first 5 lock-in amplifier time constants after each waveplate step, the data are flagged and not included in the analysis.

After subtracting the sky and telescope background, the data are converted to normalized Stokes parameters Q and U . The linear polarization and polarization position angle are given by $P = \sqrt{Q^2 + U^2}$ and $\theta = 0.5 \tan^{-1}(U/Q)$, respectively. Systematic polarization induced by the instrument and telescope adds constant contribution to the normalized Stokes parameters Q and U . The observed Q_{obs} and

U_{obs} can be written

$$Q_{obs} = Q_{source} + Q_{sys} \quad (2.2)$$

$$U_{obs} = U_{source} + U_{sys}. \quad (2.3)$$

Q_{source} and U_{source} are the Stokes parameters of the observed source, and Q_{sys} and U_{sys} are the Stokes parameters of the systematic polarization. Q_{sys} and U_{sys} are determined by observing a source for which Q_{source} and U_{source} are zero, i.e., an unpolarized source. Once the systematic contributions to the Stokes parameters are measured, they are subtracted from the normalized Stokes parameters of each observation to yield the source polarization. Finally, the polarization and position angle are calculated. The parallactic angle, field rotation caused by tracking with the Nasmyth focus telescope, and phase offset of the waveplate are all removed from the position angle.

2.4.1. Performance

Different bolometers were used for the laboratory tests of the polarimeter and the astronomical observations at the HHT. Both bolometers are ^3He cooled devices. The only relevant differences between the bolometers are: 1) the bandpasses are slightly different (the central wavelength is 1.25 mm in the laboratory instrument), and 2) the responsivity of the HHT facility instrument is a factor of several better.

The waveplate causes power loss by absorption and reflection. For a waveplate blank (before the grooves were cut) this was measured to be 19% using an external blackbody source. Application of the Fresnel equations for reflection and transmission, including multiple reflections, indicates that 9.5% is reflective with the remaining 9.5% absorptive. Cutting the grooves reduces both the reflective losses (by index matching) and the absorptive losses (by removing absorptive

material). The finished waveplate should have a total loss of 16%. A test at the telescope with celestial sources (reported below) verified the expected loss. Clemens et al. (1990) reported an insertion loss of 15% for a similar Rexolite waveplate at $\lambda = 1.3$ mm.

A dichroic waveplate introduces a systematic polarization with a sinusoidal form and a modulation frequency of 2ψ (eq. (2.1)). In fact, a nearly sinusoidal systematic polarization with an amplitude of 1.5% and a frequency of 2ψ was observed in the laboratory. This polarization arises because the waveplate is in a converging beam. Rays incident on the sides of the grooves due to the beam convergence (at an angle of up to $\sim 4^\circ$ for the HHT f/13.8 beam) are partially reflected out of the optical path. Indeed, the systematic polarization was observed to be greater in the laboratory, where a faster beam was used than at the telescope.

2.4.2. Observations at the HHT

The results of observations made on 1 June 1996 to 4 June 1996 are reported in Table 2.1. The beam size was measured by observing Jupiter, whose diameter was 44" in early June of 1996. The deconvolved beam size was 33" FWHM (33."5 \times 32."6; Az \times El), which is the diffraction limit of the 10 m diameter HHT at $\lambda = 1.3$ mm. An analysis of the pointing data, primarily Jupiter, Venus, 3C273, and W3(OH), indicated that the pointing was accurate to within 5".

The noise equivalent flux density (NEFD) of the system, without the waveplate and wire grid in the optical path, was measured by observing W3(OH). From Sandell (1994), W3(OH) has a size of 14" \times 10" (right ascension \times declination). We interpolate the expected flux in our bandpass to be 11.5 Jy. A representative NEFD, derived from a variety of elevation angles and generally good observing

conditions, is $\sim 0.7 \text{ Jy/Hz}^{-\frac{1}{2}}$. Because 1) W3(OH) is a secondary calibrator, 2) the fluxes reported in Sandell (1994) were observed with beam sizes and bandpasses different from ours, and 3) our NEFD was derived from observations at various atmospheric optical depths, we estimate an uncertainty in the NEFD of 50%. The insertion loss caused by the waveplate was measured by observing Jupiter and 3C273 with and without the waveplate in the beam path. Our observations are consistent with the 16% loss predicted from laboratory measurements despite the differences in the spectral energy distributions. The NEFD is 2.4 times larger for unpolarized sources with the waveplate and wire grid installed.

Phase averaged A/D counts from observations of Jupiter are displayed in Figure 2.2 for twelve waveplate rotations. Jupiter is less than 0.1% polarized at 1.3 mm (Clemens et al. 1990), so the observed polarization of Jupiter is the systematic polarization. The systematic polarization is dominated by the waveplate, has a sinusoidal form with an amplitude of 1.1%, and a frequency of 2ψ . Jupiter was observed with a second wire grid inserted into the optical path preceding the waveplate to determine the polarization efficiency. The observed efficiency was $98\% \pm 4(1\sigma)\%$ and therefore no corrections for efficiency were made to the data¹.

There are several reflections and beam rotations caused by the telescope, instrument optics, and the Earth's rotation that modulate the position angle and

¹The HHT facility bolometer (with its filters and focusing optics) has since been replaced and the new efficiency is $84\% \pm 1\%$. The difference between this efficiency and the previous one probably arise because the uncertainty of the first measurement was large and the bandpasses of the two bolometer systems may be different. All data presented after this chapter are corrected for the new efficiency.

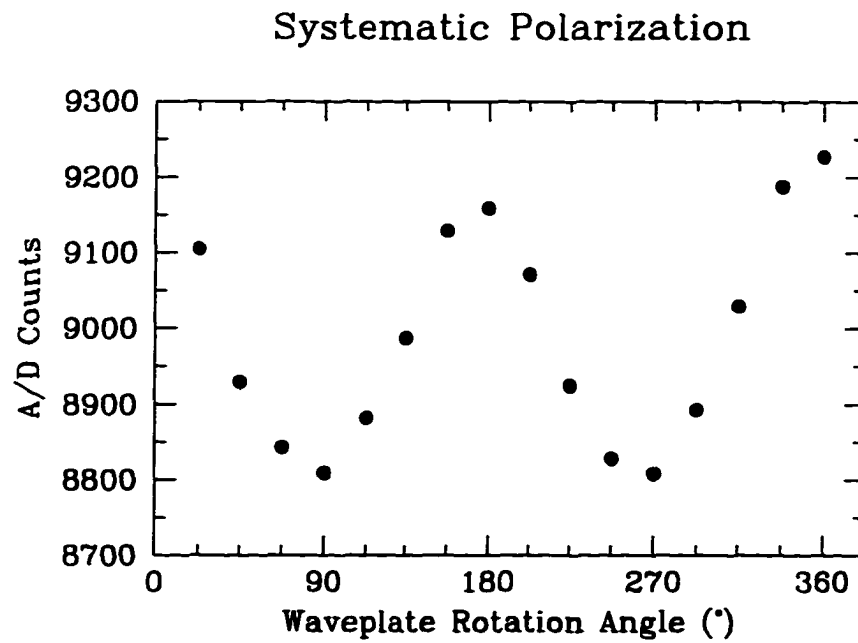


Figure 2.2 Systematic polarization measured by observing Jupiter. The points are the A/D counts for each waveplate position averaged over 12 observations of Jupiter. The 1σ uncertainties for each point have an amplitude of approximately 15 A/D counts.

contribute to ϕ in equation (2.1). These include: the parallactic angle changes because the Earth rotates, the field rotates with elevation angle for a Nasmyth focus telescope, there are reflections between the subreflector and waveplate, and the waveplate itself causes a phase change. Position angle corrections for all but the elevation and parallactic angle were determined to within 5° by placing a polarizing wire grid in the beam path (preceding the quaternary mirror) and observing Jupiter. We also used the Moon for position angle calibration since its limb is radially polarized at the level of a few percent (Clemens et al. 1990). Time permitted observations of only the eastern limb of the Moon, for which our observed position angle is $95^\circ \pm 2^\circ$ (1σ internal error). This compares well to the expected angle of 90° .

Our position angle calibration was checked by observing DR 21, a bright star formation region in the Milky Way which has a known polarization position angle. The previously derived position angles include: $\sim 21^\circ$, an average of three positions at $800 \mu\text{m}$ by Flett and Murray (1991), $\sim 26^\circ$, an average of 11 positions by Minchin and Murray at $800 \mu\text{m}$ (1994), $26^\circ \pm 3^\circ$ at $1100 \mu\text{m}$ by Tamura et al. (1995), and $15^\circ \pm 7^\circ$ at $1300 \mu\text{m}$ by Kane et al. (1993). We derived a calibrated position angle of $16^\circ \pm 3^\circ$ from a set of observations ranging 180° in parallactic angle and 60° in elevation angle. This verifies the accuracy of our corrections.

The statistical uncertainty in the observed polarization can be expressed in terms of the NEFD, the source flux density F , the efficiency of the polarimeter η , and the integration time T_{int} :

$$\sigma_p = \frac{\sqrt{2}(\text{NEFD})}{F\eta T_{\text{int}}^{\frac{1}{2}}} \quad (2.4)$$

(Novak 1989). We must scale η by 0.43 because the wire grid rejects one sense of polarization and the waveplate introduces losses. Following Platt et al. (1995), we

derive an expression for the integration time required to reach a desired σ_P from equation (2.4) and our observational data. We find

$$T_{int}(\text{hours}) = t(\text{hours}) \left[\frac{5(\text{Jy}/33'')}{F(\text{Jy}/33'')} \cdot \frac{1\%}{\sigma_P(\%)} \right]^2, \quad (2.5)$$

where t was 3 hours during the first engineering run².

A sample of the scientific observations from the engineering run is listed in Table 2.2 with the emission mechanisms that produce the polarization. Scientific implications of the observations are discussed in Chapters 3 and 4. The polarimetric bias has been subtracted to first order from the polarization of DR 21 and 3C273 using $P = \sqrt{P_{obs}^2 - \sigma_P^2}$ (see e.g., Wardle & Kronberg 1974). 3C273 is a quasar and variable in polarization. Our observations fall within the previously observed ranges for both the polarization and position angle observed at 3.4 mm (Barvainis 1984). This is the first reported 1.3 millimeter polarization observation of Cepheus A. The 3σ upper limit on the polarization is 0.9%. Like DR 21, Cepheus A is a site of star formation within the Milky Way Galaxy.

2.5. Improved Observing Scheme

A new observing scheme has been implemented for the observations reported in Chapters 3 and 4. Initially an observation consisted of four waveplate rotations. The subreflector was chopped between the source and sky at 5 Hz for each waveplate position angle, and the telescope was wobbled to place the source in the opposite beam (“on” as opposed to “off”) for the second waveplate rotation. The third and fourth waveplate rotations were then “on” followed by “off”. The

²With the improved observing scheme T_{int} is reduced slightly. However, T_{int} has been found to depend heavily the stability of the atmosphere at any optical depth.

Table 2.1. Instrument Parameters

Parameter	Performance
NEFD ^a	$\sim 0.7 \text{ Jy Hz}^{-\frac{1}{2}}$
Beam Size	33"
Systematic Polarization	1.1%
Polarization Efficiency	$84\% \pm 1\%$
Waveplate Insertion Loss	16%

^aThe waveplate and wire grid were removed from the optical path for this test.

Table 2.2. Sample of Observations

Source	RA ^a	Dec ^b	P(%)	$\theta(^{\circ})^c$	Pol. Mech.
DR 21	20:37:14.5	+42:09:00	1.65 ± 0.14	16 ± 2	Therm. Dust
3C273	12:26:33.3	+02:19:43	3.6 ± 0.8	-3 ± 6	Synchrotron
Cep A	19:59:50.0	+33:24:18	$< 0.9(3\sigma)$

^aRight Ascension (B1950)

^bDeclination (B1950)

^cEast of North

time between on and off measurements at the same waveplate position angle was 5 minutes. This observing scheme was not completely effective in minimizing sensitivity to sky noise because the sky varied between on and off observations. Now the telescope is wobbled (off-on-on-off) for each waveplate position angle with a period of 50 seconds (the subreflector is still chopped at 5 Hz). A full waveplate rotation takes just over 10 minutes. Sky noise is eliminated more effectively since both beams are sampled twice in less than a minute for each waveplate position angle. This mode was implemented by triggering waveplate steps with transitions in the telescope wobble status signal.

2.6. Conclusion

Cyclops was constructed to observe magnetic fields in dusty molecular cloud cores using the HHT. The primary practical constraints of the design were that the polarimeter operate with the facility detector and that the cost be minimal. We achieved a level of 1σ polarization uncertainty of 0.25% on 5 Jy sources in a few hours of integration time. Polarization sensitivity is primarily limited by sky noise and secondarily by the sensitivity of the facility 1.3 mm bolometer. The system can be used to measure the magnetic field structure toward numerous protostellar sources and bright molecular cloud cores in the Milky Way. The brightest HII regions and blazars can be observed at the rate of a few per day.

On the first engineering run we performed calibration and scientific observations. The systematic polarization of the instrument plus telescope is 1.1% and is correctable. DR 21 was observed and the polarization is consistent with previous measurements. The polarization of 3C273 is also consistent with previous observations. Our 0.9% upper limit on the polarization of Cepheus A is the first

1.3 mm measurement reported for that source.

CHAPTER 3

DUST CONTINUUM POLARIMETRY OF DR 21

3.1. Introduction

In this Chapter we report polarimetry of extended dust emission from DR 21. The DR 21 molecular cloud core has a mass of $\sim 20,000 M_{\odot}$ (Richardson, Sandell, and Kriscuinas 1989) and is undergoing formation of massive stars. It is at a distance of ~ 3 kpc (Campbell et al. 1982). There are at least two bipolar outflows emerging from the core region, and the primary one has the largest mass and mechanical luminosity of any protostellar outflow in the Galaxy ($> 3000 M_{\odot}$ and $> 2 \times 10^{48}$ ergs; Garden and Carlstrom 1992). DR 21 is a good candidate for continuum polarimetry because it is one of the few sources for which polarization observations have been made at several wavelengths and spatial resolutions.

3.2. Observations and Calibrations

3.2.1. $\lambda = 1.3$ mm Observations

We observed the 1.3 mm continuum polarization of DR 21 during observing runs on 1996 June 1-4, 1996 November 25-30, and 1997 March 14-15 at the Heinrich Hertz Telescope. The polarimeter design, calibration, performance, and data reduction are described in Chapter 2. A systematic, instrumental polarization of 1.1% was detected and removed from the observations. The position angle was indexed by: 1) observing Jupiter with a polarizing wire grid of known orientation in the beam path preceding the waveplate, 2) with observations of the (radially polarized) limb of the Moon, and 3) observing OMC-1, for which the polarization position angle is well known.

A nine point polarization map of DR 21 was made with the observations spaced one beamwidth (FWHM=33") apart. The observations are listed in Table 3.1. The right ascension and declination entries following the first entry are the offsets in arcseconds from the emission peak. The fourth and fifth columns are the percentage polarization and position angles.

3.2.2. $\lambda = 2$ mm Observations

We made $\lambda = 2$ mm observations toward the DR 21 emission peak with the facility polarimeter and dual polarization receivers at the NRAO 12 m telescope (Emerson, Jewell, & Payne 1995; Prigent, Abba, & Cheudin 1988). They were performed on 1995 October 26-28. Polarization modulation was achieved by rotating a parallel mirror and wire grid unit. The spacing between the wire grid and reflector was tuned to provide $\lambda/2$ modulation at 2 mm. The continuum observations were beam-switched for each of the 16 modulator positions per rotation and had a

bandpass of 600 MHz. Before making the observations, spectra were taken to confirm there were no prominent emission lines in the bandpasses. Jupiter and Saturn were used as flux calibrators.

For each continuum scan the normalized Stokes parameters, Q and U , were calculated and the parallactic angle was removed. The Stokes parameters were calculated and averaged in blocks of relatively constant parallactic angle for each orthogonal receiver independently, then the data from the two receivers were coadded with a weighted average. The polarimetric efficiency was measured by “observing” the polarized calibration noise tube mounted at the secondary mirror of the telescope. Since the observed polarization was nearly 100%, no corrections for efficiency were applied to the data.

Several factors could contribute to systematic instrumental polarization. Two obvious ones are imperfect differential reflection by the wire grid in the modulator and multiple off-axis reflections preceding the polarization modulator in the optical path. The expected level of the polarization induced by differential reflection of the wire grid is nearly zero because the wire spacing is essentially ideal at $\lambda = 2$ mm. Likewise, the instrumental polarization caused by inclined reflections should be much less than 1%. We observed Jupiter to determine the instrumental polarization and found $P=0.21\%\pm0.13\%$. Subtracting the bias yields $P=0.16\%\pm0.13\%$. Clemens et al. (1990) reported a polarization of $\sim 0.04\%$ for Jupiter at $\lambda = 1.3$ mm. We did not reach this precision with our observations and we conclude that no instrumental polarization was detected.

We determined the position angle (PA) zero point registration in several ways. First, the PA of the noise tube, known to $\sim 4^\circ$, was used to index the PA. Second, OMC-1 has been observed by many investigators (e.g., Scheuning, Dowell, & Platt

1996), and all derive a PA of $\sim 32^\circ$. We obtain $34^\circ \pm 1^\circ$. Additionally, the north and south points of the limb of the moon were observed. Our observations are consistent to an uncertainty of a few degrees with previous lunar observations (e.g., Clemens et al. 1990) that indicate a radial polarization. Observations of the Crab Nebula, which is polarized by synchrotron radiation, yielded $P=18.4\%\pm0.5\%$ with $PA=147^\circ \pm 1^\circ$. This measurement is to be compared with $P=15.7\%\pm0.3\%$ and $PA=155^\circ \pm 1^\circ$ at $\lambda = 3.4$ mm observed by Barvainis (1984). The difference between our observed PA and that of Barvainis (5σ) is not surprising given that his beam was 1.5 times larger and the frequencies of the observations were different. Indeed, the high spatial resolution optical polarization images of Schmidt, Angel, & Beaver (1979) reveal that there is significant structure in the magnetic field in the vicinity of the pulsar at the $20''$ scale. Given the different beam sizes and wavelengths of the observations, the $2.7\%\pm0.6\%$ difference in the observed polarizations is not a concern.

3.3. Discussion

3.3.1. Spatial Structure

By combining our $\lambda = 1.3$ and 2 mm observations with earlier observations (Table 3.2), we can analyze the continuum polarization of DR 21 as a function of wavelength and size scale. A comparative analysis of the continuum polarimetry of DR 21 must be performed with caution, however. The observations probe not only different spatial distributions, but possibly also different dust populations. Shorter wavelengths will preferentially probe warmer dust that is presumably nearer sources of heat. The Minchin and Murray (1994) polarization map of DR 21 is composed of 11 positions centered on the right ascension and declination given

in Table 3.2. They extend $\sim 14''$ north and south, and $\sim 7''$ east and west. The polarization and position angle are fairly uniform throughout their map. The unweighted average of those observations is listed in Table 3.2. Similarly, the Flett and Murray (1991) data are the unweighted average of 3 positions, one at the right ascension and declination listed, and one each at $\Delta\delta = \pm 8''$.

The 1.3 mm polarization map of DR 21 obtained with Cyclops is displayed in Figure 3.1. The percentage polarization and position angle are fairly uniform throughout the cloud. Because the telescope beam has a gaussian profile and the source is centrally peaked, the flux weighted centroid of each observation is displaced slightly toward the emission peak from the location denoted in Figure 3.1. This may contribute slightly to the uniformity of the polarization observed throughout the cloud. The polarization position angles are neither parallel to nor orthogonal to either of the molecular outflows.

Leach et al. (1991) and Schleuning et al. (1996) found that the polarization position angles from their maps of OMC-1 are uniform, but the percentage polarization is reduced at the emission peak. Minchin and Murray (1994) claimed the percentage polarization is reduced at the emission peak of DR 21, but the reduction is only marginally statistically significant. In both cases it was suggested that the polarization may be reduced because uniform field lines were dragged into a radial configuration by infall into the cloud core. The polarization observations from Figure 3.1 have been binned into radial bins using unweighted averages and displayed in Figure 3.2. Except for the DR 21SS point, the polarization does not depend on radial distance from the core. DR 21 is extended several arcminutes in the north-south direction, so although the offsets to the negative beams were $\pm 120''$, it is possible that the DR 21SS observation was corrupted by emission in

Table 3.1. Cyclops 1.3 mm Polarimetry of DR 21

Source	RA ₁₉₅₀	Dec ₁₉₅₀	P(%)	$\theta(^{\circ})$
DR 21	20 37 14.5	+42 09 00	2.0±0.1	23±2
DR 21N		+33	2.8±0.7	17±8
DR 21S		-33	1.7±0.6	32±11
DR 21E	+33		1.6±0.4	21±8
DR 21W	-33		2.5±0.7	26±10
DR 21NW	-33	+33	2.5±0.7	37±7
DR 21SW	-33	-33	2.1±0.8	-2±11
DR 21NE	+33	+33	2.3±0.7	9±11
DR 21SS		-66	6.6±0.7	49±4

Table 3.2. Continuum Polarimetry of DR 21

$\lambda(\mu\text{m})$	$\Omega_{FWHM}('')$	$\alpha(1950)$	$\delta(1950)$	P(%)	PA($^{\circ}$)	Ref. ^a
115	35	20:37:14.0	42:09:12	1.1±0.3	25±7	1
350	17	20:37:14.0	42:09:12	1.5±0.6	21±11	1
450 ^b		20:37:14.5	42:09:00	2.3±0.4	46±5	2
800	19	20:37:14.5	42:09:00	~ 2.4	~ 21	2
800	14	20:37:14.5	42:09:00	~ 2.3	~ 26	3
1100	19	20:37:14.3	42:08:55	3.3±0.3	26±3	4
1300	27	20:37:14.5	42:09:15	4.5±1.1	15±7	5
1300	33	20:37:14.5	42:09:00	2.0±0.1	23±2	6
2000	42	20:37:14.8	42:08:56	0.77±0.13	2±5	6

^a1. Dowell, Schleuning, and Hildebrand 1996. 2. Flett and Murray 1991.
3. Minchin and Murray 1994. 4. Tamura et al. 1993. 5. Kane et al. 1993.
6. This thesis.

^bBeam size not reported.

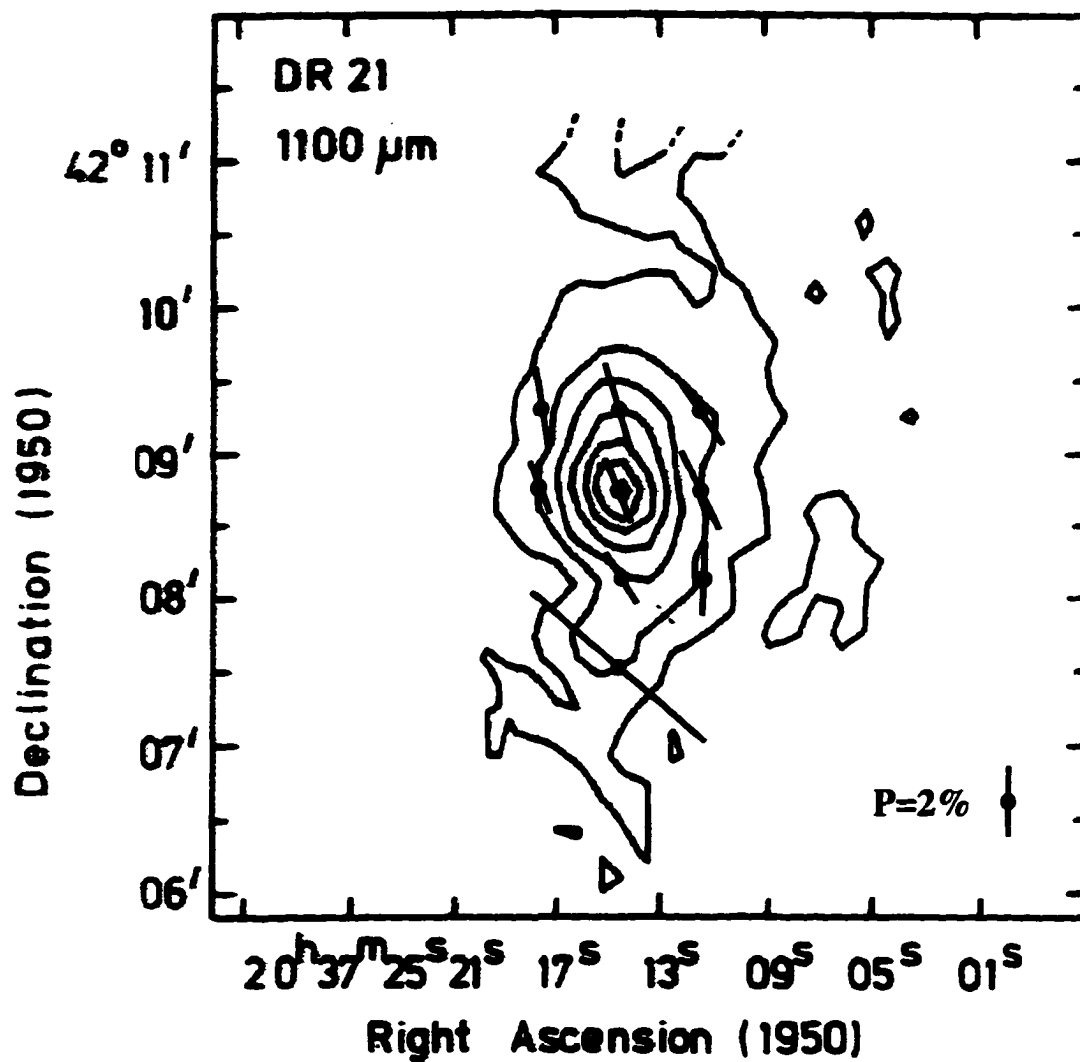


Figure 3.1 1.3 mm linear polarization map of DR 21. The 1.1 mm continuum contour map is from Richardson, Sandell, and Krisciunas (1989). The points indicate the positions of the observations, which are spaced one beamwidth (33" FWHM) apart. The length of the line segments is proportional to the percentage polarization and the position angles of the line segments are the polarization position angles. The line segment in the lower right corner represents $P = 2\%$.

the negative beam. Therefore, we do not consider the DR 21SS polarization to be indicative of radial structure.

Assuming the polarization does not depend on wavelength, we can test for a radial dependence of polarization in the core by comparing observations made with different beam sizes. Polarization is plotted versus beam size in Figure 3.3 (excluding the low S/N, offset position of Kane et al. 1993). There is no convincing evidence for a simple trend in polarization as a function of beam size. Since the region emitting polarized radiation is larger than the largest beam (FWHM), this seems to suggest that the beam integrated magnetic field collimation and grain alignment efficiency do not vary dramatically in the inner 30'' of the core (0.4 pc at a distance of 3 kpc; Campbell et al. 1982). This conclusion is supported by the uniformity of the polarization seen in the map of Minchin and Murray. In fact, since the polarization percentage and position angle are approximately constant throughout the cloud as indicated by the Cyclops map, the line of sight integrated magnetic field lines appear to be uniform over the inner square parsec of DR 21.

Since stars are forming, at least part of the DR 21 cloud core must be undergoing infall. If the field lines have indeed been dragged in, why do we not observe a radial polarization dependence? The most likely reason is the large distance to DR 21. OMC-1 is at a distance of ~ 400 pc (Anthony-Twarog 1982). If OMC-1 were at the distance of DR 21, the radial dependence of the polarization would be detectable out to 10'' from the emission peak. Even with the spatial resolution of the 800 μm map made by Minchin and Murray (1994), only a marginally statistically significant polarization decrement would have been detected in the core.

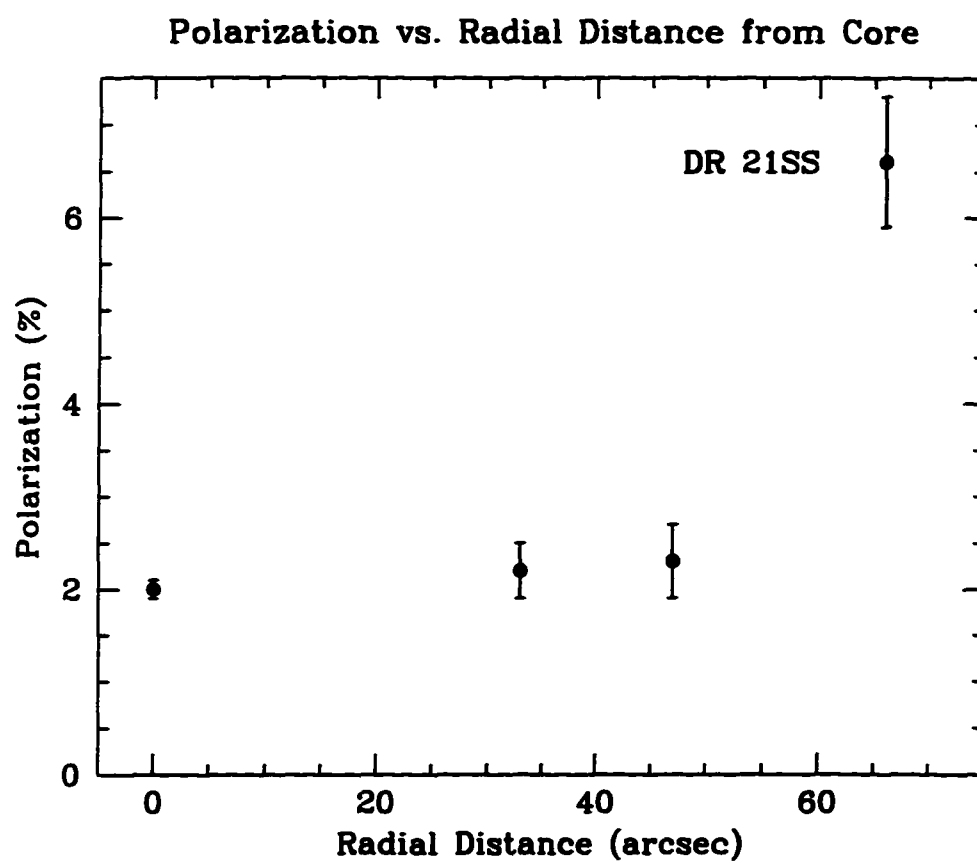


Figure 3.2 Radial dependence of the DR 21 polarization. The data points are unweighted radial averages from the map in Figure 3.1 and the error bars are 1σ uncertainties. The DR 21SS data point is labeled.

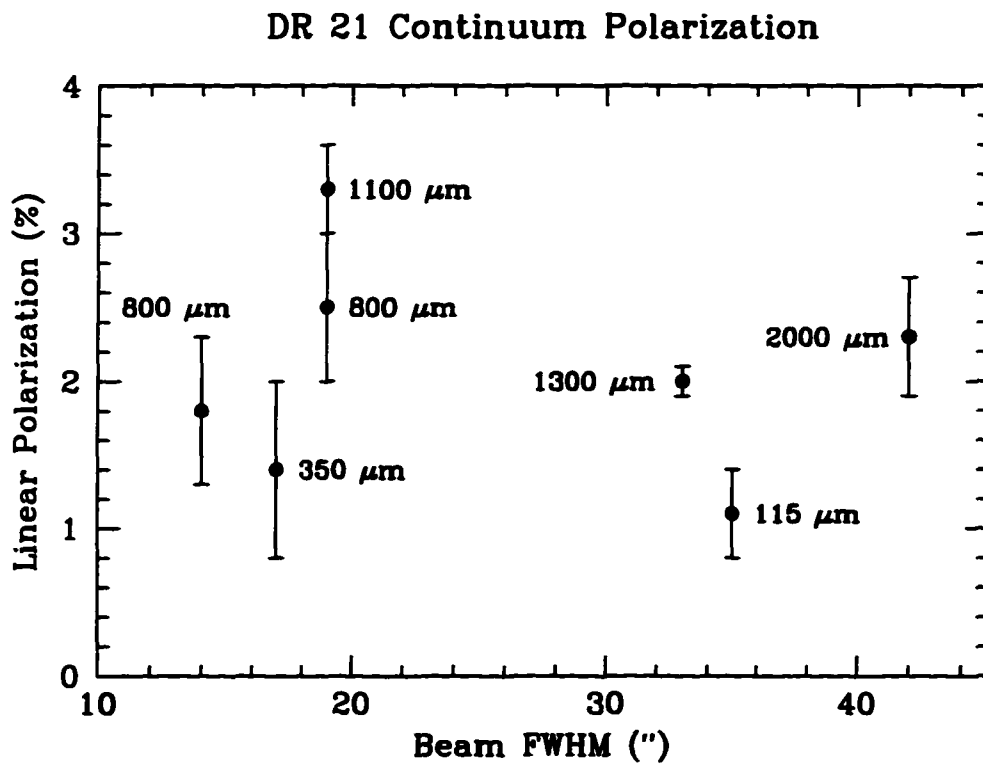


Figure 3.3 Continuum polarization as a function of beam size. The 2 mm data point is the free-free corrected dust polarization. The 450 μm observation of Flett and Murray (1991) is not plotted because the beam size is not reported and the position angle is not consistent with the other observations. Error bars are 1σ statistical uncertainties.

3.3.2. Wavelength Dependence

It is possible to use the wavelength dependence of polarized thermal dust grain emission, $dP/d\lambda$, as a diagnostic of grain composition, however $dP/d\lambda$ should be very small in most cases. For grains with dielectric functions $\epsilon(\lambda) = \epsilon_1(\lambda) + i\epsilon_2(\lambda)$, polarization is independent of wavelength if: 1) the wavelength is much larger than grain sizes, 2) ϵ_1 is constant, and 3) $\epsilon_2^2 \ll (\epsilon_1 - 1)^2$. All these conditions are satisfied for grains at far infrared and longer wavelengths (Hildebrand 1988) unless grains are metallic, i.e., condition (2) is not satisfied. Since grains are much smaller than the wavelength of radiation impinging on them, $dP/d\lambda$ is independent of grain shape and size¹ (see Mathis, Rumpl, and Nordsieck 1977 and Draine and Lee 1984).

Polarization of dust continuum emission from DR 21 is diluted by molecular line emission and thermal bremsstrahlung radiation from the H II regions. The observed polarization can be described by

$$P_{obs} = \frac{P_{dust} \cdot F_{dust}}{F_{total}}, \quad (3.1)$$

where P_{obs} is the observed polarization, P_{dust} is the true dust polarization, F_{dust} is the flux density of the dust, and F_{total} is the combined flux density of the dust, free-free emission, and line emission ($F_{total} = F_{dust} + F_{ff} + F_{le}$). The contribution from line emission was not significant in our $\lambda = 2$ mm observations, but it dilutes the polarization in the other observations. Groesbeck (1995) performed a survey of

¹Schleuning et al. (1996) found that the ratio of 1.3 mm polarization to 100 μ m polarization of Orion KL is too large to be explained by the dielectric properties of a single population of grains. They therefore suggest that the ratio could be large because different wavelengths sample different grain populations or radiative transfer effects preferentially reduce the 100 μ m polarization.

line emission from 330 to 360 GHz to determine the line contribution to the fluxes in these bands for the Orion-KL, Orion S, and IRAS 16293-2422 star forming regions. Being a site of massive star formation, Orion-KL is presumably the most like DR 21 and has the highest contribution by line emission of the three, at $\sim 50\text{--}60\%$. Sutton et al. (1984) showed that lines are responsible for $\sim 40\%$ of the flux from 215 to 247 GHz in Orion-KL. From models based on these observations, Groesbeck (1995) concluded that the line contributions were maximum from 300 to 600 GHz, and not significant compared to the dust emission for $\nu > 600$ GHz. We conclude that 1) the observed polarization for $\lambda = 800 \mu\text{m}$ to 1.3 mm are lower limits to the true dust polarization, 2) it is likely that $P_{obs} < P_{dust} \leq 2P_{obs}$ for these wavelengths, and 3) the dilution of polarization by line emission is similar from 800 μm to 1.3 mm.

The free-free emission (mapped by Harris 1973 and Gordon et al. 1986) extends to $20''$ from the position of our $\lambda = 2$ mm observations (FWHM = $42''$). The dust emission, mapped at $\lambda = 800$ and $1100 \mu\text{m}$ by Richardson et al. (1989), drops rapidly from the peak and extends at a low level to $\sim 2'$. Therefore, by subtracting the expected free-free emission contribution to the continuum, an estimate of the intrinsic dust polarization at $\lambda = 2$ mm can be derived. No similar correction is necessary at the shorter wavelengths because the free-free contribution is smaller than the uncertainties in the measurements.

Assuming the free-free emission is optically thin and extrapolating from 3.5 mm (Gordon et al. 1986) implies $F_{ff,2mm} = 15$ Jy. Assuming 1) the dust is optically thin at 800 and $1100 \mu\text{m}$ (Richardson, Sandell, & Krisciunas 1989) and 2) the dust temperature (T_{dust}) is 47 K (Kane et al. 1993; derived from *IRAS* observations), and subtracting the free-free contributions from the integrated

800 μm and 1100 μm flux densities of 435 and 100 Jy, we derive a dust opacity spectral index of $\beta \sim 2.4$ ($\sigma_{\nu, \text{dust}} \propto \nu^{-\beta}$). This implies $(F_{\text{dust}, 2\text{mm}}) \sim 8$ Jy. Our 2 mm photometry of DR 21 is imprecise, but is consistent with the expected F_{total} . Substitution in equation (3.2) yields $P_{\text{dust}} = 2.3\% \pm 0.4\%$. P_{dust} is dependent on β : for β ranging from 2.0 to 2.7 (consistent with the photometry of Richardson, Sandell, & Kriscuinas 1989), P_{dust} varies from 2.0% to 2.6%. P_{dust} is not sensitive to the assumed T_{dust} : reducing T_{dust} by 50% changes P_{dust} by only a few tenths of a percent.

Based on their 800 μm polarimetry, plus the 1100 μm (Tamura, Hough, & Hayashi 1995) and 1300 μm (Kane et al. 1993) measurements, Minchin and Murray (1994) concluded there is a large rise in polarization with wavelength toward the DR 21 dust core, and that the composition of the dust cannot be purely silicates² (see Hildebrand 1988). Our $\lambda = 1300$ μm and (free-free corrected) $\lambda = 2$ mm observations are plotted in Figure 3.4 with the other observations listed in Table 3.2. These new observations refute the conclusion of Minchin and Murray. Instead, they are consistent with the “standard” grain composition of silicates and graphite based on model fits to interstellar extinction and polarization curves along many lines of sight (Mathis, Rumpl, and Nordsieck 1977).

3.3.3. Magnetic Field Strength

Although it is not possible to derive magnetic field strengths directly from dust continuum polarimetry, it is possible to place limits under some assumptions.

²Complicating this multi-wavelength comparison, the Kane et al. measurement was 15" north of the submillimeter flux peak, and the far infrared and submillimeter emission peaks are displaced by 20" (Colomé et al. 1995).

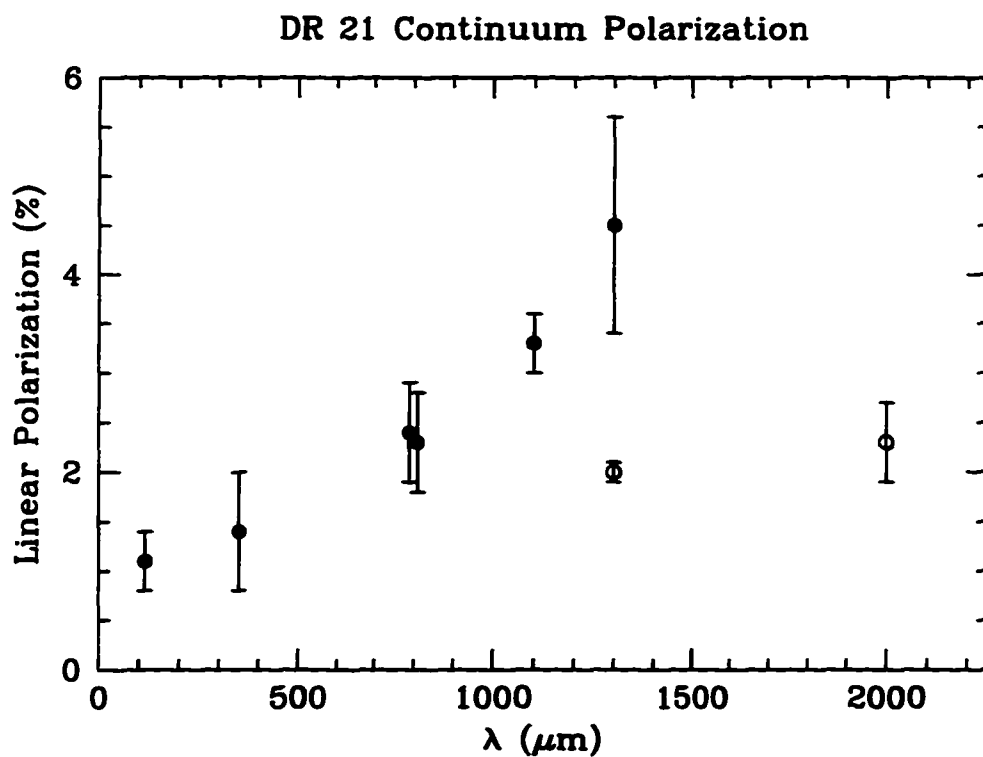


Figure 3.4 Continuum polarimetry of DR 21 as a function of wavelength. Error bars are 1σ statistical uncertainties. The open circles are the new 1.3 mm and 2 mm data points. The 2 mm data point is the free-free corrected dust polarization. The 800 μm points are displaced slightly in wavelength for clarity.

Based on the lack of HCO^+ emission line polarization, an upper limit of 4 mG is placed on the component of the magnetic field orthogonal to the outflow in Chapter 4.2.2. Richardson, Sandell, & Krisciunas (1989) derived a field strength of ~ 3 mG assuming that the cloud core is magnetically supported against self gravity. Since there are other support mechanisms, such as thermal pressure and molecular outflows, this is an upper limit.

Chandrasekhar and Fermi (1953) estimated the average local magnetic field in the disk of the Galaxy from rms gas velocities in the interstellar medium and the dispersion in position angles of starlight polarized by transmission through interstellar dust. They assumed an equipartition of energy between random gas motions and Alfvén waves in the interstellar magnetic field. The dispersion in the polarization position angles represents the bending of magnetic field lines by gas motions. The magnetic field strength is given by

$$B_{\perp} = \sqrt{4\pi\rho} \langle \Delta V_{\parallel}^2 \rangle^{\frac{1}{2}} / \langle \theta^2 \rangle^{\frac{1}{2}} \quad (3.2)$$

where \perp means projected onto the plane of the sky, \parallel means along the line of sight, and ρ is the mass density of the medium (Zweibel 1996).

It is audacious to apply this technique to DR 21 for at least a few reasons. First, gravitational potential energy has not been included in equation 3.2, which will cause the magnetic field strength to be over estimated. Second, the magnetic field will be overestimated because gas motions include infall and outflow. Third, excluding DR 21SS, there are only 8 data points in the map, which is not adequate to derive a precise dispersion. The impact of the second concern is minimized by using the line width observed away from the cloud core, where non-random gas motions contribute least to the line width. A representative average velocity dispersion of C^{18}O is ~ 1.3 km/s (Dickel, Dickel, and Wilson 1978). The dispersion

in the 1.3 mm position angles is 12° . Since the average position angle 1σ uncertainty is 9° the true dispersion is less than 12° , and consequently the field strength will be somewhat underestimated. Nevertheless, inserting these values into equation 3.2 indicates the average magnetic field strength in DR 21 projected onto the plane of the sky is less than ~ 4 mG.

Roberts, Dickel, and Goss (1997) observed HI Zeeman absorption toward DR 21. They detected a strong line of sight magnetic field of $-442 \pm 62 \mu\text{G}$ in the negative velocity gas associated with the star forming region. An average field of $-400 \mu\text{G}$ was detected at $> 3.5\sigma$ over a region extending approximately $10''$ north-south and $5''$ east-west of RA(B1950) $20^h 37^m 14.8^s$ and Dec(B1950) $+42^\circ 09' 06''$. This region is coincident with the dust emission peak. They interpreted their observations to indicate that the gas in which they detected the magnetic field is outflowing in front of the HII region. Since the magnetic field in the outflowing gas is not representative of the DR 21 average field, it should not be directly compared to the magnetic field lines inferred from the 1.3 mm continuum polarimetry. A field strength of $400 \mu\text{G}$ in this compact region is not in conflict with the 4 mG upper limit derived above. Rather, it indicates that the upper limit is at least an order of magnitude too large to be useful. More extensive HI Zeeman maps and higher resolution dust continuum polarimetry are required to construct a three dimensional model of the magnetic field in DR 21.

A simple comparison of the average thermal, turbulent, and magnetic pressures in the DR 21 core can be made with the observed quantities. For $n = 10^6 \text{ cm}^{-3}$ (Richardson, Sandell, & Krisciunas 1989) and $T = 50 \text{ K}$ (from the CO observations of Phillips et al. 1981 and IRAS photometry of Kane et al. 1993) in the core of DR 21, the thermal pressure nkT is $\sim 7 \times 10^{-9} \text{ dyn cm}^{-2}$. The pressure due to

turbulence $P_{turb} = 0.5mn\sigma_v^2$, with $\sigma_v \sim 4.6$ km/s in the core (Dickel, Dickel, and Wilson 1978), is $\sim 3.5 \times 10^{-7}$ dyn cm $^{-2}$. The magnetic pressure $P_B = B^2/8\pi$ for $B < 4$ mG is $P_B < 6 \times 10^{-7}$ dyn cm $^{-2}$. This approximate calculation indicates that the primary support mechanism of the DR 21 cloud is turbulent gas motion. Since the average magnetic field is really probably ≤ 400 μ G, magnetic pressure is probably the least significant support mechanism and the cloud has undergone supercritical collapse.

3.4. Summary

The principal results of the investigation of DR 21 continuum polarization are:

- 1) Our $\lambda = 1.3$ mm and 2.0 mm continuum polarimetry of the DR 21 dust core indicate polarization levels lower than previous millimeter measurements. The polarization does not exhibit a strong wavelength dependence and is consistent with the standard grain composition of silicates and graphite.
- 2) The polarization percentage and position angle vary remarkably little in the inner arcminute of the cloud. There is no dependence of polarization on beam size for the observations toward the core. This suggests the magnetic field collimation and grain alignment efficiency do not vary dramatically in the inner parsec.
- 3) Based on the small dispersion of the 1.3 mm polarization position angles, an approximate upper limit of 4 mG is placed on the component of the average magnetic field in the plane of the sky. This is similar to the upper limit derived by assuming the magnetic field supports the cloud against gravitational collapse. Turbulent gas motions are a more significant source of

support against self gravity in the molecular cloud core than thermal pressure or magnetic fields.

CHAPTER 4

DUST CONTINUUM POLARIMETRY SURVEY OF STAR FORMATION REGIONS

4.1. Introduction

Magnetic fields are an important parameter in the physics of molecular clouds. They are probably partially responsible for cloud support and affect star formation, especially in the case of low mass stars (e.g., Mouschovias 1976; Shu, Adams, & Lizano 1987). Despite their fundamental importance, there are few observations of magnetic fields in molecular clouds. Projections of magnetic field lines on the plane of the sky can be determined with polarization observations of optically thin dust emission. Non-spherical grains aligned in magnetic fields emit thermal radiation polarized perpendicular to the field lines (see, e.g., Hildebrand 1988). In this Chapter we report a small polarimetry survey of cloud cores with embedded protostars to investigate magnetic fields in star formation regions.

4.2. Observations and Calibrations

We observed the 1.3 mm continuum polarization of several bright star forming regions during observing runs on 1996 June 1-4, 1996 November 25-30, and 1997 March 14-15 at the Heinrich Hertz Telescope. The polarimeter design, calibration, performance, and data reduction are described in Chapters 2 and 3. The observations are listed in Table 4.1. The first column is the list of objects, the second and third columns are the right ascension and declination (B1950) of each object, and the fourth and fifth columns are the percentage polarization and position angles.

A five point polarization map was made of Cep A with the observations spaced half a beam width FWHM ($17''$) apart. There is no evidence for polarization structure in the Cep A cloud. The signal to noise ratio of the outer observations is poor, however, and the spatial structure is not well sampled since the angular size of the emission region is comparable to the beam size.

It is possible that the last five observations in Table 4.1 were corrupted by an instrumental polarized flux. Except for Mon R2, for which the polarization was observed to be consistent only at the 3σ level during the latter two runs, these objects were only observed in November 1996 and are fainter than the others. They all have raw¹ U Stokes parameters in the range $\sim .015 - .035$. Additionally,

¹Raw means the Stokes parameters are not corrected for parallactic angle rotation, telescope elevation angle, and systematic polarization. Several of the DR 21 map observations in Chapter 3 (DR 21N, NW, SW, NE, W) are also faint and were observed in both of the latter two runs. All of these except DR 21NW have U_s in the range given above, however the observations from the second run agree with the

Table 4.1. Cyclops 1.3 mm Polarimetry Survey

Source	RA ₁₉₅₀	Dec ₁₉₅₀	P(%)	$\theta(^{\circ})$
W3(OH)	02 23 16.5	+61 38 57	0.7 ± 0.5	
NGC1333 IRAS 4A	03 26 04.8	+31 03 14	4.5 ± 0.8	-26 ± 6
L1551 IRS5	04 28 40.2	+18 01 45	$< 3.6(3\sigma)$	
OMC-1	05 32 46.7	-05 24 16	2.2 ± 0.1	34 ± 2
Sgr B2	17 44 10.2	-28 22 02	0.8 ± 0.5	
W58	19 59 50.0	+33 24 18	0.7 ± 0.5	
GL2591	20 27 35.8	+40 01 15	1.6 ± 0.5	-6 ± 10
DR 21	20 37 14.5	+42 09 00	2.0 ± 0.1	23 ± 2
S140	22 17 41.0	+63 03 41	$< 1.2(3\sigma)$	
Cep A	22 54 20.2	+61 45 55	0.8 ± 0.2	81 ± 9
Cep AN		+17"	1.3 ± 0.6	72 ± 15
Cep AS		-17"	4.6 ± 1.6	54 ± 11
Cep AE	+17"		$< 0.9(3\sigma)$	
Cep AW	-17"		$< 1.3(3\sigma)$	
00494+5617	00 49 27.8	+56 17 28	2.4 ± 0.4	-90 ± 5
NGC1333 IRAS 4B	03 26 06.5	+31 02 51	2.1 ± 0.9	10 ± 13
05338-0624	05 33 52.6	-06 24 02	4.2 ± 0.9	-87 ± 7
Mon R2	06 05 20.3	-06 22 31	1.1 ± 0.3	44 ± 8
21391+5802	21 39 10.2	+58 02 29	2.2 ± 0.6	22 ± 9

IRC+10216, a carbon rich evolved star, was observed to have a polarization of $3.7\% \pm 1.2\%$ (with raw $U=.03$), in contrast to the upper limit of 2% at $350 \mu\text{m}$ of Dowell (1997). The raw Q s are randomly distributed around zero. These observations suggest that there could be a systematic, instrumental polarized flux. This could be tested with observations of blank sky, but unfortunately none were made during the November 1996 run. Observations of blank sky were made during the first and third runs and no instrumental polarized flux was detected. Such a polarized flux could occur if the beam were significantly misaligned from the center of the subreflector. This instrumental polarized flux does not affect the observations of the brighter objects. The faint objects will be reobserved at the first opportunity. Special mention is made where they are included in the following analyses.

4.3. Discussion

To analyze the submillimeter and millimeter polarization of molecular cloud cores, we combined the observations reported in this thesis with the $800 \mu\text{m}$, 1.1 mm , and 1.3 mm polarimetry observations reported in the literature. This list is not exhaustive: only those observations in the literature that satisfy the criterion of one or more of the subsets listed in the following analyses are included. The observations are listed in Table 4.2. For the sources that were mapped with polarimetry, only the observations toward the emission peaks of the cores were included in Table 4.2. For example, the $800 \mu\text{m}$ observation of $\rho \text{ Oph SM1}$ is included, but the observation of VLA 1623 (same reference) is not.

first run, so they are probably not corrupted.

Table 4.2. Continuum Polarimetry from the Literature

Source	RA ₁₉₅₀	Dec ₁₉₅₀	λ (mm)	P(%)	$\theta(^{\circ})$	Ref. ^a
W3IRS5	02:21:53.2	+61:52:21	0.8	0.5 ± 0.3	47 ± 18	1
NGC1333IRAS4A	03:26:04.8	+31:03:14	0.8	3.2 ± 0.3	132 ± 3	2
NGC1333IRAS4A	not	given	1.1	4.6 ± 0.8	145 ± 5	3
NGC1333IRAS4A	03:26:05.0	+31:03:14	3.4	4.0 ± 0.7	103 ± 6	4
NGC1333IRAS4B	03:26:06.5	+31:02:51	0.8	1.5 ± 0.6	100 ± 10	2
L1551 IRS5	not	given	1.1	3.3 ± 0.6	145 ± 5	3
L1551 IRS5	not	given	0.8	$< 1.5(3\sigma)$		3
Orion KL	05:32:46.7	-05:24:16	1.3	2.7 ± 0.3	34	5
OMC-1	05:32:46.9	-05:24:26	0.8	1.2 ± 0.2	44 ± 5	6
Mon R2	06:05:19.8	-06:22:41	0.8	1.3 ± 0.3	2 ± 6	7
Mon R2	06:05:19.8	-06:22:41	1.1	2.5 ± 0.4	171 ± 4	7
ρ Oph SM1	16:23:26.0	-24:17:06	0.8	1.9 ± 0.7	146 ± 10	8
IRAS16293-2422	not	given	1.1	2.8 ± 0.5	144 ± 5	9
IRAS16293-2422	not	given	0.8	1.4 ± 0.5	62 ± 11	6
Sgr B2(N)	17:44:08.8	-28:21:15	1.3	0.8 ± 0.3	22 ± 9	10
Sgr B2(S)	17:44:09.2	-28:22:07	1.3	0.6 ± 0.2	-26 ± 7	10
Sgr B2(N)	17:44:09.9	-28:21:15	0.8	$< 1.1(1\sigma)$		11
Sgr B2(M)	17:44:10.2	-28:22:02	0.8	0.8 ± 0.4	35 ± 13	11
IRAS18162-2048	18:16:13.2	-20:48:46	0.8	1.6 ± 0.4	97 ± 7	12
M17-SW	18:17:28.1	-16:14:00	0.8	$< 0.9(3\sigma)$		13
W49	19:07:49.6	+09:01:24	1.3	0.9 ± 0.4	35 ± 12	10
W51	19:21:25.9	+14:24:34	1.3	0.5 ± 0.2	-31 ± 11	10
S106 IR	20:25:34.3	+37:12:50	0.8	3.1 ± 0.8	173 ± 7	8
GL2591	20:27:35.7	+40:01:15	0.8	2.6 ± 0.5	30 ± 5	14
W75N-IRS1	20:36:49.6	+42:26:56	0.8	0.7 ± 0.2	55 ± 5	15
DR21	20:37:14.5	+42:09:00	0.8	1.8 ± 0.3	17 ± 4	16
S140-SMM1	22:17:39.5	+63:03:35	0.8	1.4 ± 0.4	99 ± 7	14
NGC7538IRS11	23:11:36.8	+61:10:37	0.8	2.5 ± 0.2	58 ± 2	16

^a1. Greaves, Murray, & Holland 1994. 2. Minchin, Sandell, & Murray 1995. 3. Tamura, Hough, & Hayashi 1995. 4. Akeson et al. 1996. 5. Leach et al. 1991. 6. Flett & Murray 1991. 7. Greaves, Holland, & Murray 1995. 8. Holland et al. 1996. 9. Tamura et al. 1993. 10. Kane et al. 1993. 11. Greaves et al. 1995. 12. Greaves, Holland, & Ward-Thompson, 1997. 13. Vallee & Bastien 1996. 14. Minchin, Bonifácio, & Murray 1996. 15. Vallee & Bastien 1995. 16. Minchin & Murray 1994.

4.3.1. Interpreting Dust Polarimetry: The Effects of Large Optical Depths

It is generally assumed that far infrared, submillimeter, and millimeter polarization is caused by the dichroic emission from aligned grains. In support of this, Tamura et al. (1995) showed for IRAS 16293-2422, L1551 IRS 5, and NGC1333 IRAS 4, that the inferred magnetic field lines from submillimeter/millimeter observations tend to align with the field lines of the embedding cloud interpolated from observations of background starlight. This validity of this method is debatable however, see Chapter 1.2 and Goodman et al. (1995).

It has been shown that the dust emission from L1551 IRS 5 and IRAS 16293-2422 probably has two components: an optically thin envelope and an unresolved, optically thick ($\tau \sim 1$) core (Mezger, Wink, and Zylka 1990). These components contribute similar amounts to the observed emission. NGC 1333 IRAS 4A is also optically thick for $\lambda < 1.1$ mm (Sandell et al. 1991). Further, there is evidence that the cores are not spherically symmetric, i.e. they are disks (Tereby, Chandler, and André 1993). The consequences of optically thick cores must be considered to interpret polarimetry.

Can scattering of submillimeter/millimeter radiation by dust grains contribute to the observed polarization? This can be tested by calculating the ratio of the scattering cross section, σ_s , to the absorption cross section, σ_a , for dust grains. Because dust grains are probably not much larger than $1 \mu\text{m}$ (Mathis, Rumpl, and Nordsieck 1977, Kim, Martin, and Hendry 1994), Rayleigh scattering is appropriate for calculating scattering cross sections. The cross section is given by:

$$\sigma_s = \frac{128\pi^5 a^6}{3\lambda_0^4} \left(\frac{\epsilon\mu - 1}{\epsilon\mu + 2} \right)^2, \quad (4.1)$$

where a is the grain radius, and ϵ and μ are the electrical permittivity and magnetic

susceptibility of the grains (Lang 1980). Hildebrand (1983) gives the absorption cross section for grains:

$$\sigma_a = \pi a^2 Q_{250} (250/\lambda_0)^\beta, \quad (4.2)$$

where Q_{250} is the grain emissivity at 250 μm and β is typically between 0 and 2. For $Q_{250} = 1/2666$ (Hildebrand 1983), $(\epsilon\mu - 1)/(\epsilon\mu + 2)$ of order (but less than) 1, and λ and a in μm :

$$\frac{\sigma_s}{\sigma_a} = 1.1 \times 10^7 (250)^{-\beta} \lambda_0^{\beta-4} a^4. \quad (4.3)$$

Choosing $\beta = 2$ and $a = 1 \mu\text{m}$ optimistically in favor of scattering, $\sigma_s/\sigma_a \sim 1.8 \times 10^{-4}$ at $\lambda_0 = 1 \text{ mm}$. Therefore, scattering probably does not contribute significantly to the polarization and we will interpret $\lambda = 1.3 \text{ mm}$ polarization as arising from dichroic emission.

Can dichroic absorption by aligned grains contribute to observed polarizations? Probably only in cases of extremely high optical depth at far infrared wavelengths. Dowell et al. (1997) mapped the 60 and 115 μm polarizations of Sgr B2. They found that polarization by dichroic absorption in the cloud core was necessary to explain their results. The 100 μm optical depth of Sgr B2 could be as large as $\tau \sim 10$. They concluded that Sgr B2 is an unusual case because of the extremely high optical depth and that previous interpretations of far infrared polarization observations did not have to be revised. So, although there are no other clouds for which the far infrared polarization observations imply dichroic absorption, it might have to be considered in cases where the optical depth is much greater than one.

4.3.2. NGC1333 IRAS4A

Polarimetric observations of NGC1333 IRAS4A have been made at 0.8 mm (Minchin, Sandell, and Murray 1995), 1.1 mm (Tamura, Hough, and Hayashi

1995), 1.3 mm (this thesis), and 3.4 mm (Akeson and Carlstrom 1996). NGC1333 IRAS4A is a deeply embedded protostar in the Perseus cloud complex. It has been resolved into a binary system with single dish submillimeter observations by Sandell et al. (1991). The two components of the binary are connected by a bridge of emission. Lay, Carlstrom, and Hills (1995) showed that each component is itself a multiple system. The polarization, which is plotted versus wavelength in Figure 4.1, is remarkably independent of wavelength and beamsizes, although Akeson and Carlstrom (1996) showed that there is some polarization structure detectable at 5'' resolution. The observations are consistent with the polarization being dominated by a region smaller than $\sim 10''$ (3500 AU at 350 pc; Herbig and Jones 1983), or the polarization being uniform over a region larger than the largest beam of 33'' (12,000 AU). The latter condition would imply the magnetic field projection on the plane of the sky is the same in the envelope and the dense core. The polarization could increase with wavelength if thermal bremsstrahlung emission dilutes the 3.4 mm polarization. As in the case of DR 21, the lack of a strong dependence of polarization on wavelength does not allow silicates to be ruled out as a significant component of the dust.

4.3.3. Polarization Position Angles and Molecular Outflows

An obvious question to ask is: are polarization position angles related to molecular outflow orientations? Bonifácio and Emerson (1996) modelled the probability density function of the angle between linear polarizations and outflow directions accounting for projection onto the plane of the sky. They assumed uniform magnetic fields threading protostellar systems at varying angles to the outflows. They found that the probability density function can be broad and peaks at an angle approximately complementary to the angle the magnetic field and outflow

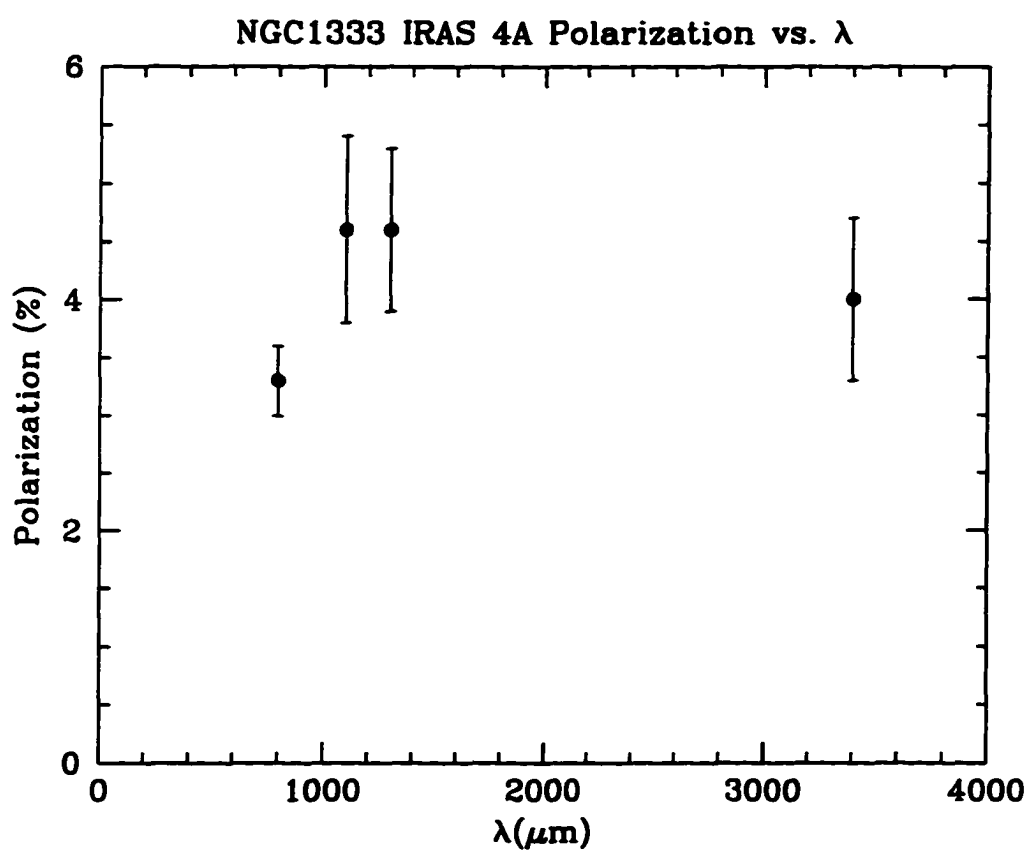


Figure 4.1 Wavelength dependence of the NGC1333 IRAS 4A linear polarization. The data are from Tables 4.1 and 4.2. The error bars are 1σ uncertainties.

make in space.

Minchin, Bonifácio, and Murray (1996) compiled sixteen submillimeter polarization observations from the literature of cloud cores with protostellar outflows. They determined the position angles of the outflows from molecular tracers, such as CO and H₂. Seven of the sixteen sources had outflow position angles that differed by 80°-90° from the polarization position angles and the remaining sources were distributed approximately evenly from 0° to 80°. By comparing the angle distribution to the model of Bonifácio and Emerson, they concluded that the observed distribution could be explained if all outflows for which the outflow direction and polarization position angle differ by $\leq 10^\circ$ have poloidal fields ($B \parallel$ outflow), and all the others have toroidal fields ($B \perp$ outflow).

One must be cautious interpreting these data. NGC1333 IRAS 4A and IRAS 4B are both in the group of seven with outflow position angles nearly orthogonal to the polarization position angles. NGC1333 IRAS4 is a binary and each component has an outflow. The outflow from 4A is bent however, and changes position angle by nearly 40° (Blake et al. 1995). The outflow from 4B is bipolar, but it is compact and the position angle is difficult to determine. Excluding 4B, 6/15 of the outflows are approximately orthogonal to the polarization position angles. Another binary, IRAS16293-2422, has two outflows with bipolar axes that differ by 40° (Walker et al. 1988). The two polarization position angles at 800 μm and 1.1 mm in Table 4.2 differ by 7σ and are not consistent since the polarization should depend very little on wavelength. Minchin, Bonifácio, and Murray (1996) compared the 800 μm polarization to either the 1629a outflow axis or the average of the outflow axes. The 1.1 mm polarization observation actually has a much higher S/N, 5.6σ compared to 2.8σ for the 800 μm observation.

If we make the null hypothesis that the polarization and outflow position angles are unrelated, a Kolmogorov-Smirnov test (see Press et al. 1992) can determine the probability that the observed cumulative distribution of the difference in polarization and outflow position angles from Minchin, Bonifácio, and Murray (1996) is different from the distribution of polarization and outflow position angles randomly oriented with respect to each other. Such a test yields a probability of 0.4 that the observed distribution is consistent with a set of 15 differences between random polarization and outflow position angles². Including IRAS05338-0624 and IRAS2139+5802 (bipolar outflow position angles of $\sim 5^\circ$ and $\sim 75^\circ$, respectively, Wilking, Blackwell, and Mundy 1990)³, for which it is possible the polarizations have instrumental contributions, increases the number of outflows approximately orthogonal to the polarization position angles to 7/17 and decreases the KS probability to 0.3. Therefore, this sample of observations does not rule out the possibility that the outflows are randomly oriented with respect to the magnetic fields. We concur with Minchin, Bonifácio, and Murray that more observations are needed.

Because star formation regions have multiple outflows, it is perhaps not surprising that there is not a tight correlation between outflow position angles and inferred magnetic field lines. For example, DR 21 has two major outflows with nearly orthogonal projections on the plane of the sky (Garden et al. 1991). Observers simply choose the largest outflow to compare to the polarization position

²This technique is described in detail in the next section.

³IRAS00494+5617, also known as NGC281-West, may have an outflow but it is not clear if it is bipolar (Snell, Dickman, and Huang 1990), so it is not included in this analysis.

angle. Further, the protostars were chosen because they are bright, hence many of them are also massive. Massive protostars probably form from supercritical cores, in which case infall might be unrelated to the magnetic field configurations.

4.3.4. Polarization Position Angles and Cloud Core Elongations

Perhaps a better relationship to investigate is between the position angles of maximum cloud elongation and the polarization position angles. If molecular cloud cores have uniform magnetic field lines threading them that provide substantial pressure support, one might expect cloud cores to be elongated (oblate) orthogonal to field lines. There is theoretical evidence that cloud cores do initially collapse along field lines (e.g., Galli and Shu 1993). Indeed, the simple, elongated cores, such as DR21, OMC-1, and ρ Oph A are elongated nearly orthogonal to the uniform magnetic fields threading them (at least in the plane of the sky). In addition, the dust emission joining the binary components of NGC1333 IRAS4 and IRAS16293-2422 is approximately orthogonal to the inferred magnetic field lines. It is also possible, however, that cloud cores could be prolate and elongated parallel to the uniform component of the field if anisotropic support arises from the propagation and dissipation of nonlinear Alfvén waves (Shu, Adams, and Lizano 1987).

Kane et al. (1993) compared IRAS maps of star forming cloud cores to 1.3 mm polarization observations. They found that there was a tendency for cloud cores to be elongated orthogonal to the inferred magnetic field lines, but there were only four polarization detections with a significance of $> 3\sigma$ in their sample. Their results must be interpreted with caution because the 100 μm morphologies differ from those observed at submillimeter and millimeter wavelengths. Since submillimeter and millimeter observations probe cooler dust than far infrared

observations, and the emission is more optically thin at the longer wavelengths, submillimeter/millimeter morphologies are more appropriate for comparison to submillimeter/millimeter polarization observations. Comparative analyses have shown (e.g., Ladd et al. 1991, Fuller et al. 1995) that cloud core morphologies traced by dust emission and optically thin molecular species are similar.

Table 4.3 lists the position angles of the dust core elongations (hereafter elongation angles) for the combined sample of polarization observations reported in this thesis and compiled from the literature. Column 2 contains the wavelengths used to make the maps. For objects with maps at multiple wavelengths, the maps with: 1) map wavelengths closest to the polarimetry wavelengths, 2) the highest signal to noise ratios, and 3) the best spatial resolution were chosen for comparison to the polarimetry. The distances to the objects in the table range over an order of magnitude and the maps were made with angular resolutions from $\sim 5''$ to $27''$. Since the spatial resolutions are so inhomogenous and many of the data are not available in electronic format, it is not appropriate to attempt to fit ellipses to the contour maps to derive elongation angles. Consequently, the elongation angles listed in column 3 of Table 4.3 are the position angles of greatest elongation at the contour midway between the peak and the noise level. The clouds were separated by morphology into one of the five rather subjective categories: not elongated (or not resolved), moderately elongated, elongated, double, or disk if the dust emission has been shown to arise largely from a disk. The morphology of M17 is too complex to include it in this analysis.

What is the expected probability density function for the difference between the polarization position angles and the elongation angles projected onto the plane of the sky? The answer to this question depends on the expected relationship

Table 4.3. Cloud Core Elongation Angles

Source	$\lambda(\text{mm})$	Elong. Ang. ($^\circ$)	Morphology	Ref. ^a
W3(OH)	0.8	88 ± 10	Mod. Elong.	1
NGC1333IRAS4	0.8	133 ± 5	Double	2
L1551 IRS5	0.7	N/A	Disk	3
OMC-1	1.3	24 ± 5	Elongated	4
Mon R2	1.3,0.8	50 ± 10	Mod. Elong.	5,6
ρ Oph A	0.8	6 ± 5	Elongated	7
IRAS16293-2422	3.0	-40 ± 10	Double	8
Sgr B2	1.1	-1 ± 5	Double	9
IRAS18162-2048	1.1	N/A	Not. Elong.	10
M17	1.3	N/A	Complex	11
S106 IR	0.8	84 ± 5	Elongated	12
GL2591	1.3	-55 ± 10	Mod. Elong.	6
W75N-IRS1	0.8	32 ± 15	Not Elong.	13
DR 21	1.1	7 ± 10	Elongated	14
S140	1.3,0.8	46 ± 10	Mod. Elong.	6,15
Cep A	1.3	84 ± 15	Not Elong.	6
NGC 7538	0.8	62 ± 10	Mod. Elong.	16
IRAS00494+5617	1.3	N/A	Not Elong.	17
IRAS05338-0624	1.3	N/A	Not Elong.	6
IRAS21391+5802	1.3	-80 ± 15	Not Elong.	6,18

^a1. Oldham et al. 1994. 2. Sandell et al. 1991. 3. Ladd et al. 1995. 4. Mezger, Wink, and Zylka 1990. 5. Greaves, Holland, and Murray 1995. 6. Walker et al. 1990. 7. André, Ward-Thompson, and Barsony 1993. 8. Walker, Carlstrom, and Bieging 1993. 9. Goldsmith et al. 1990. 10. McCutcheon et al. 1995. 11. Hobson et al. 1993. 12. Richer et al. 1993. 13. Valleé and Bastien 1995. 14. Richardson, Sandell, and Krisciunas 1989. 15. Minchin, Sandell, and Murray 1995. 16. Sandell unpublished. 17. Henning et al. 1994. 18. Wilking et al. 1993.

(or relationships) between magnetic field orientations and cloud core elongations. Rather than assume a particular relationship (i.e., cloud cores are oblate, shortest along the field lines), we make the null hypothesis that the magnetic field lines in the cloud cores are not related to the elongation angles. Then we estimate the probability that the distribution arising from the difference between unrelated field line and elongation angles is different from the observed distribution. Because the sample is composed mostly of high mass cores that we expect to be magnetically supercritical, we expect a random distribution between the magnetic field lines and cloud elongation angles.

What is the probability distribution of the difference between the field line angles and the elongation angles if they are random with respect to each other? Let the origin of coordinates be at the location of a hypothetical object on the celestial sphere. Let the x - y plane be the plane of the sky and the z axis be the line of sight. In spherical coordinates θ is the angle between the line of sight and a vector originating from the object. ϕ is the angle a vector rotated about the z -axis makes with the x -axis. With this choice of coordinates ϕ is the projection onto the plane of the sky of a vector originating from the object.

Let ϕ_{PPA} be the sky plane projection of the polarization position angle and ϕ_{EA} be the sky plane projection of the elongation angle. Next, we write the distribution of the difference of random (ϕ_{PPA}, ϕ_{EA}) pairs, $\Delta\phi = \phi_{PPA} - \phi_{EA}$, given that the difference is always chosen by the observer to be between 0 and $\pi/2$. The probability density function $P(\Delta\phi)$ has two components:

$$P_1(\Delta\phi) = P(|\phi_{PPA} - \phi_{EA}|) \quad \text{for} \quad |\phi_{PPA} - \phi_{EA}| < \pi/2, \quad (4.4)$$

$$P_2(\Delta\phi) = P(|\phi_{PPA} - \phi_{EA}| - \pi) \quad \text{for} \quad |\phi_{PPA} - \phi_{EA}| > \pi/2. \quad (4.5)$$

These normalized distributions are

$$P_1(\Delta\phi) = \frac{2}{\pi} \left(\frac{-\Delta\phi}{\pi} + 1 \right) \quad (4.6)$$

$$P_2(\Delta\phi) = \frac{2\Delta\phi}{\pi^2}. \quad (4.7)$$

Since one or the other of the conditions (3.8) and (3.9) is always satisfied, but never both,

$$P(\Delta\phi) = P_1(\Delta\phi) + P_2(\Delta\phi) = 2/\pi. \quad (4.8)$$

$P(\Delta\phi)$ is constant with respect to $\Delta\phi$ for $0 \leq \Delta\phi \leq \pi/2$. When computing a difference, $\Delta\phi$, the observer actually calculates

$$\Delta\phi = \min(|\phi_{PPA} - \phi_{EA}|, |\phi_{EA} - \phi_{PPA}|). \quad (4.9)$$

A Monte Carlo simulation of (4.9) verified that $P(\Delta\phi)$ is constant with respect to $\Delta\phi$. So, the probability density function of the difference between the projections of the polarization and elongation angles is constant if the polarization and elongation angles are random with respect to each other.

The cumulative distributions of the observed and theoretical ($\Delta\phi$)s are plotted in Figure 4.2. Only $\geq 3\sigma$ polarization detections, and only elongated cores, moderately elongated cores, and IRAS16293-2422 and NGC1333 IRAS4 were included. The latter two were included because the systems are elongated by material bridging the components of the binaries. In the cases where there were multiple, consistent polarization observations, the highest signal to noise observations were used. Although the number of observations is small, it appears that the observed distribution is not significantly different from a distribution with polarization position angles and elongation angles randomly oriented with respect to each other.

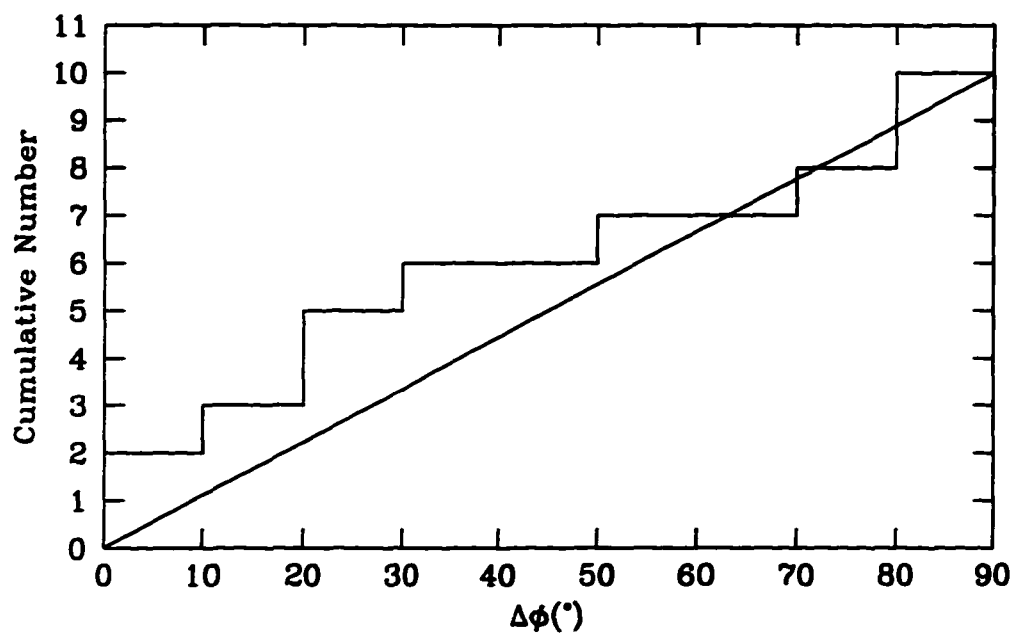


Figure 4.2 Cumulative distribution of the difference between cloud core elongation angles and polarization position angles. The stepped line is the observational data and the smooth line is the theoretical distribution assuming cloud elongation angles are randomly distributed with respect to magnetic field line orientations.

A statistical comparison is dubious because ten points are not sufficient to perform a reliable analysis and the sample is inhomogeneous. As an example of the inhomogeneity, the masses derived from the dust emission from IRAS16293-2422 and NGC1333 IRAS 4A to DR 21 are different by a factor of 10^3 . Nevertheless, a Kolmogorov-Smirnov test yields a 0.4 probability that a cumulative distribution of ten random $\Delta\phi$ s would deviate more from the theoretical distribution than the observed distribution deviates from the theoretical distribution. If NGC1333 IRAS4A and IRAS16293-2422 are removed from the sample, leaving bright, high mass cores, the probability becomes 0.9. Including IRAS21391+5802, which is slightly elongated and might have an instrumental contribution to the polarization, changes the probabilities both to 0.7 with and without NGC1333 IRAS4 and IRAS16293-2422. We conclude that the inferred magnetic field lines are approximately orthogonal to the elongations of the morphologically simple clouds (and the disks of IRAS 16293-2422 and NGC1333 IRAS 4A), but for the ensemble of cloud cores there is no convincing evidence that the field lines are not randomly distributed with respect to the cloud core elongations.

Sweeping conclusions are provisional because the polarimetry sample is small and projection effects, multiple outflows, and selection effects make interpretation difficult. However, the evidence in this survey indicates that there is no clear tendency for any preferred alignment of molecular outflows or cloud core elongations with respect to magnetic field lines, especially for the bright, high mass protostars and star forming regions. In particular, the lack of a correlation between the cloud core elongations and magnetic fields suggests that the massive cloud cores are magnetically supercritical, which is not at all surprising since high mass stars are forming in the cores. Polarization observations of many protostars with both interferometers and single-dish telescopes are needed to test accretion and outflow

models. The survey must be extended to include many low mass protostars and cores to determine if they are magnetically subcritical or supercritical.

4.3.5. Polarization Percentages and Cloud Core Elongations

If we assume a parent population of randomly oriented oblate clouds with their short axes parallel to uniform magnetic field lines permeating them, we might expect the polarization to increase with increasing axial ratio projected on the plane of the sky. This is because the projection of the magnetic field lines onto the plane of the sky, and therefore the polarization, would be maximum for edge on clouds. The data set compiled here is too inhomogeneous in terms of beam sizes and distances to the objects to calculate reliable axial ratios. So, rather than rigorously test for a correlation between elongation and percentage polarization, we use the simple (subjective) morphology classes introduced in Chapter 4.3.4. Not elongated corresponds roughly to an axial ratio close to 1, moderately elongated corresponds roughly to an axial ratio of approximately ≤ 2 , and elongated corresponds roughly to an axial ratio of approximately ≥ 2.0 . The axial ratios refer to the map contours levels of 25-50% of the peak flux.

The percentage polarization is plotted as a function of morphology class in Figure 4.3. Each point is plotted with its own 1σ error bars. The unweighted average of the polarization observations in each bin is indicated with a horizontal line segment across the width of the bin. The scatter within each bin is large, which is expected given the inhomogeneity of the sample. There is a suggestion of a trend of increasing polarization with increasing elongation going from the “Not Elongated” cores to the “Elongated” cores. Such a trend would be consistent with cores with large projected elongations also having large magnetic field projections on the plane of the sky. Including IRAS00494+5617, IRAS05332-0624, and

IRAS21391+5802, however, increases the average in the “Not Elongated” bin to 2.0%, eliminating the trend in polarization. This highlights the need to observe these sources again. A set of maps with a homogeneous spatial resolution is needed to do a proper statistical analysis.

One might expect polarization to depend on the optical depth and temperature in cloud cores. The optical depths and temperatures derived from photometry of dust emission have large uncertainties, however. For example, in the case of L1551 IRS 5 and IRAS 16293-2422, the derived optical depths and temperatures vary by an order of magnitude and a factor of two, respectively, depending on the beam size of the observations and whether one or two components are fit to the dust emission (e.g., Mezger, Wink, and Zylka 1990). The optical depths and temperatures were derived for IRAS 16293-2422, Cep A, Mon R2, and L1551 IRS 5 by Walker, Adams, and Lada (1990). Those observations were made at 1.3 mm with a beam size (27" FWHM) similar to ours (33" FWHM). Within this small subsample the 1.3 mm polarization is independent of temperature and optical depth. To properly test for polarization dependence on physical conditions in clouds, a set of photometry and polarimetry maps must be made with the same spatial resolution.

4.3.6. Distribution of Polarization Position Angles in the Plane of the Galaxy

Radio observations of synchrotron emission from spiral galaxies indicate that in most cases interstellar magnetic field lines are well ordered and follow the spiral arms almost perfectly (Beck 1996). The highest fractional polarizations are found in the interarm regions, probably because turbulent cloud motions and supernovae in the arms tangle the field lines and depolarize the emission. Heiles (1996) examined the Galactic magnetic field using observations of pulsars, diffuse synchrotron emission,

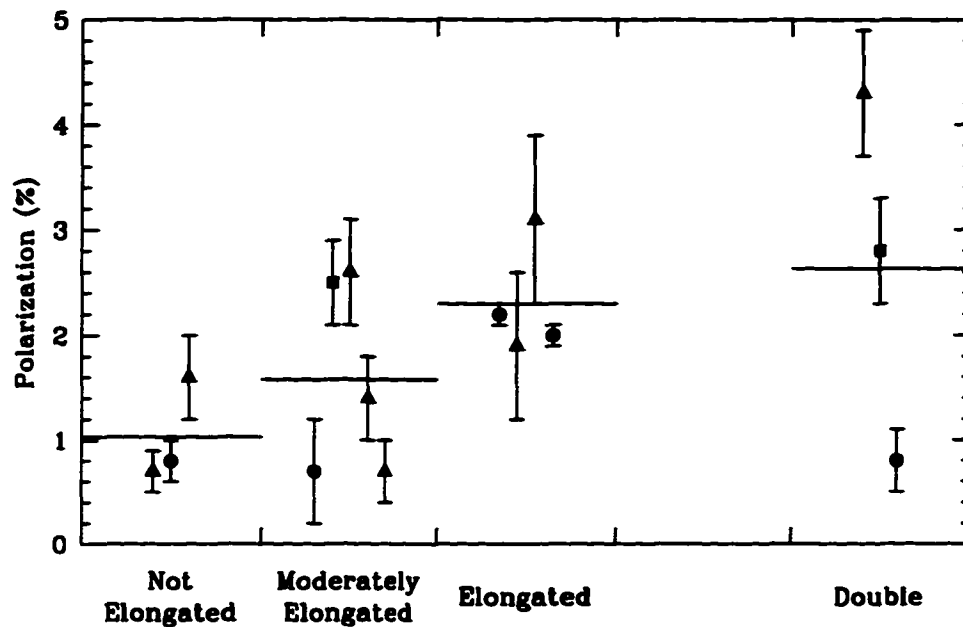


Figure 4.3 Percentage polarization versus cloud elongation. The elongation classes are described in the text. Triangles are 800 μm observations, squares are 1.1 mm observations, and circles are 1.3 mm observations. The error bars are 1σ uncertainties. The horizontal line segments are the unweighted averages of the observations in the bins. The “Double” bin, which includes star formation regions with multiple resolved cores (Sgr B2, IRAS16293-2422, and NGC1333 IRAS4A), has been offset from the other bins because we are not suggesting the multiple sources are part of the same possible trend.

and polarized starlight. Although the conclusions derived from the various data sets disagreed somewhat, Heiles found that the field lines follow a spiral pattern. The inclination of the magnetic spiral may be different from the inclination of the Galaxy's spiral arms. Motivated by the observations, Heiles adopted a field strength of $3.6 \mu\text{G}$ for the azimuthal average of the random component of the field near the Solar circle, $2.2 \mu\text{G}$ for the uniform component, and $4.2 \mu\text{G}$ for the total, with the total strength increasing to $\sim 5.9 \mu\text{G}$ in the spiral arms. Ruzmaikin, Sokoloff, and Shukurov (1988) reviewed the generation of large scale magnetic fields in spiral galaxies by dynamo action.

Since the Galaxy is mostly optically thin at $\lambda = 1 \text{ mm}$, using the combined observations from this survey and compiled from the literature, we can test if the inferred magnetic field lines tend to lie in the plane of the Galaxy. The observations with the smallest polarization uncertainty were used for those objects with observations at multiple wavelengths, and the object with the highest S/N was used if observations of neighboring objects were available. This left a total of twelve independent measurements. We point out that the observations do not sample the Galactic plane well: many of the objects are nearby and most are clustered near $l^{II} \sim 80^\circ$, $b^{II} \sim 0^\circ$ or $l^{II} \sim 110^\circ$, $b^{II} \sim 0^\circ$.

The distribution of the differences between the position angles of the field lines and the local position angles of the Galactic plane is plotted in Figure 4.4. Within this sample, the magnetic fields appear randomly oriented with respect to the Galactic plane, implying that the random component of the field dominates in this sample. The dust emission observations probe the densest part of the interstellar medium, denser than the diffuse interstellar medium probed by the optical polarimetry included in the study by Heiles, and are consistent with a trend

of increasing disorder in the fields from the interarm regions, to the spiral arms, to the molecular cloud cores. This could be a manifestation of decreasing energetic importance of magnetic fields relative to local gas dynamics (i.e., stellar outflows) and gravitation from size scales of kiloparsecs to size scales of parsecs.

4.3.7. Distribution of Polarization Percentages

Hildebrand (1996) compiled the 100 μm polarization observations made from the Kuiper Airborne Observatory. He included all detections of $\geq 3\sigma$ significance and for which $\sigma_P < 1\%$. The distribution of polarization peaks at 2%, declines rapidly to 6%, and has a tail to a maximum of 9%. Hildebrand pointed out that the distribution would increase monotonically from $P = 0\%$ to $P(\text{max}) = 9\%$ if the number of occurrences of a given polarization depended only on the inclination of the field to the line of sight. Other factors, such as grain alignment efficiency and the uniformity of field lines along the line of sight, also affect the observed polarization.

Histograms of the number of occurrences of 800 μm and 1.1-1.3 mm polarization percentages are shown in Figure 4.5. Observations listed in Tables 4.2 and 4.3 that have uncertainties of $\leq 0.5\%$ are included. Because the bins are 1% wide, the requirement that the uncertainties are less than 0.5% gives a high probability that the real (exact) polarizations fall within the bins to which they are assigned. For objects with multiple observations at 1.1-1.3 mm, the observation with the smallest uncertainty was selected. Since only a single observation (toward the peak of the source) per wavelength is included for each source, all sources are represented equally. The 800 μm distribution has the same overall shape as the 100 μm distribution. There is a suggestion of an excess in the number of polarizations less than 1% in the 1.1-1.3 mm distribution compared to the 100 and

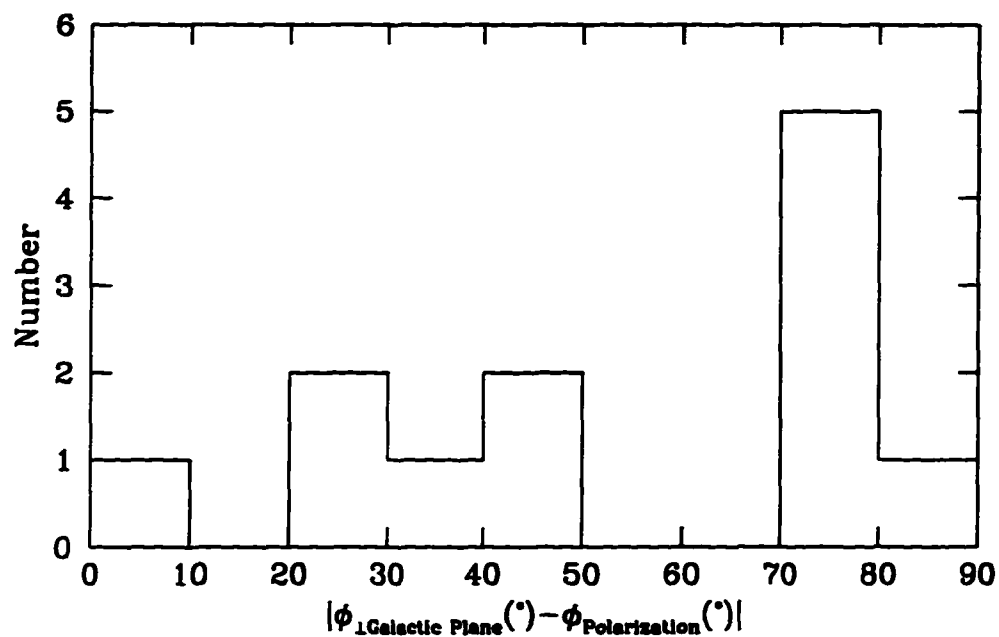


Figure 4.4 Distribution of the difference between the polarization position angles and the local normals to the Galactic plane. A difference of 0° would mean the projections of the magnetic field lines and the plane of the Galaxy are colinear on the plane of the sky.

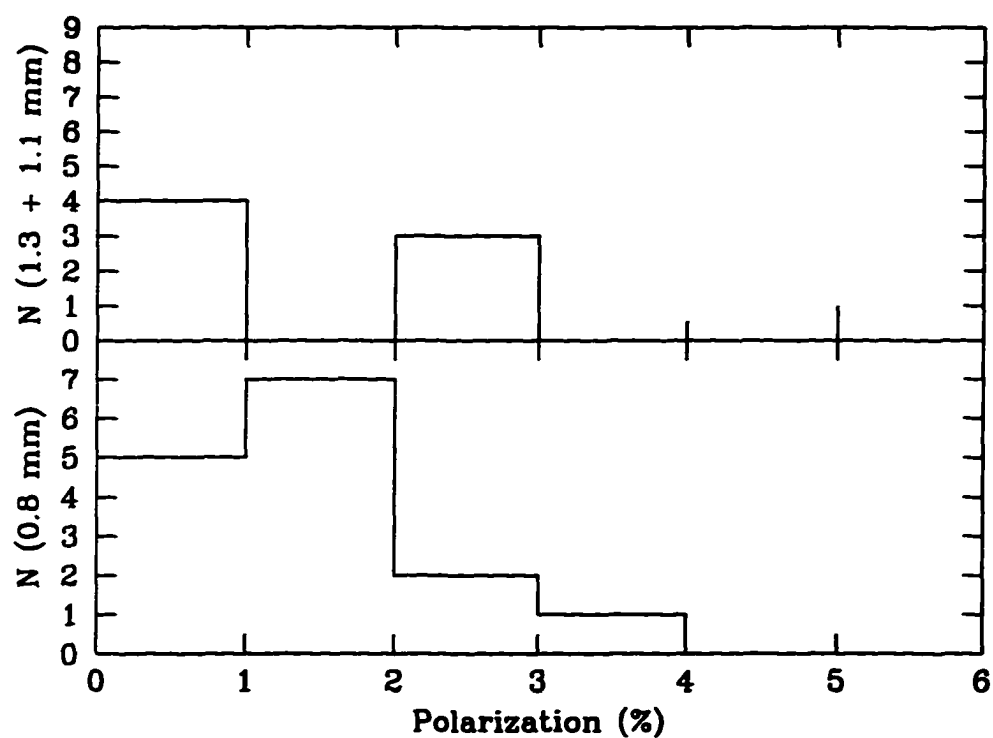


Figure 4.5 800 μm and 1.1-1.3 mm percentage polarization histograms. Only observations toward the emission peaks and with $\sigma_P < 0.5\%$ are included.

800 μm distributions. The objects in this bin are bright HII regions unresolved, or barely resolved, at 1.3 mm. The low polarization could result from complicated, unresolved magnetic field line structures. More observations are necessary to test the significance of this excess. Since there is little polarization dependence on wavelength expected on the Rayleigh-Jeans side of the emission peak (Chapter 4.3.1), it is not surprising that the percentage polarization distributions are similar at 100 μm and 1 mm.

4.4. Summary

The principal results of the polarimetry survey of star formation regions composed of observations from this thesis and compiled from the literature are:

- 1) The observations do not rule out the possibility that protostellar outflows are randomly oriented with respect to the magnetic field lines observed from the protostars.
- 2) For a few simply elongated cloud cores, the magnetic field lines projected onto the plane of the sky are approximately orthogonal to the elongations of dust emission. However, there is no clear tendency for any preferred alignment of cloud core elongations with respect to magnetic field lines, especially for the bright, high mass star forming regions. This confirms that the massive cloud cores are magnetically supercritical, which is expected since stars are forming in the cores. There is possible evidence that the percentage polarization of cloud cores increases with their elongation on the plane of the sky, but more observations of polarization are needed to test this trend and theories of star formation in general.

- 3) Although the observations do not sample the Galactic plane well, the magnetic fields in the cloud cores appear randomly oriented with respect to the Galactic plane, implying that the random component of the Galactic magnetic field dominates the spiral component in this sample.
- 4) Again, the number of millimeter observations is small, but the distribution of 0.8-1.3 mm polarization percentages does not differ significantly from the distribution at 100 μm .

CHAPTER 5

HCO⁺ AND CS SPECTROPOLARIMETRY OF MOLECULAR OUTFLOWS FROM PROTOSTARS

5.1. Introduction

Magnetic fields are an important parameter in the physics of molecular clouds. They are partially responsible for cloud support and may affect the collapse dynamics of low mass, prestellar cloud cores by ambipolar diffusion (e.g., Mouschovias 1976; Shu, Adams, & Lizano 1987; McKee et al. 1993). Despite their fundamental importance, there are few observations of magnetic fields in molecular clouds. Polarization in rotational emission lines of molecules is expected in molecular clouds where there is a gradient in the line optical depth (τ_{line}). The gradient can be caused by a velocity gradient or an anisotropic radiation field. A gradient

in τ_{line} produces a non-LTE population of the Zeeman sublevels. If the magnetic field along the line-of-sight is predominantly uniform, spontaneous decay from the differentially populated sublevels adds to produce a linear polarization in the line. For significant polarization to occur, τ_{line} must be $\lesssim 1$.

There are several models that quantitatively predict this polarization. A large velocity gradient (LVG) model using two molecular rotational levels was proposed by Goldreich & Kylafis (1981, 1982). They predicted polarizations up to 14% and pointed out that the direction of the magnetic field in the plane of the sky could be derived with spectropolarimetry. A multi-level model also using the LVG approximation was developed by Deguchi & Watson (1984). They found that adding more levels reduced the predicted level of polarization to $\lesssim 7\%$. Lis et al. (1988) developed a model that abandoned the LVG approximation and did not require the presence of a magnetic field. They concluded that polarizations of a few percent should be observable.

All attempts to observe this polarization have yielded only upper limits. Wannier, Scoville, & Barvainis (1983) observed the hot cores of several molecular clouds, and the centers and edges of dark clouds in rotational transitions of CO, ^{13}CO , HCN, and CS. They found in all cases that polarization, if present, was less than one-third of the theoretical predictions, and achieved upper limits as low as 0.5% in a few cases. They suggested that the lack of polarization could be the result of unresolved kinematic or magnetic structure. Barvainis and Wootten (1987) observed NH_3 in OMC-1 and were also unsuccessful in detecting polarization. Lis et al. (1988) observed four dark clouds and placed upper limits as low as 2% on the polarization.

We chose DR 21 as the primary target in our search for spectral line

polarization because it has several promising characteristics. One would expect the LVG approximation to be appropriate to outflows if ambient material is progressively accelerated along the outflow, or if the outflow is stalled in snowplow fashion as momentum is transferred to progressively more ambient mass. The molecular outflow associated with DR 21 has been mapped in the HCO^+ $J=1-0$ transition with the Hat Creek interferometer (Garden & Carlstrom 1992). Further, the outflow is almost perpendicular to the line of sight, maximizing the predicted line polarization. The molecule HCO^+ was chosen because its high dipole moment ($\mu = 4.5$ Debye) and abundance (fractional abundance typically $\sim 10^{-8}$) maximize the expected degree of polarization (Lis et al. 1988).

We performed $\lambda = 3.3$ mm spectropolarimetry towards the peak of the brightness distributions of the DR 21, Mon R2, and IRAS 16293-2422 molecular outflows. Section 5.2 presents details of our observations and data analysis. Section 5.3 presents the results of the observations. These results are discussed in section 5.4. A summary is given in section 5.5.

5.2. Observations and Calibrations

The observations were made with the facility polarimeter and dual polarization 3 mm receiver at the NRAO 12 m telescope (Emerson, Jewell, & Payne 1995; Prigent, Abba, & Cheudin 1988) on 1994 June 1–5 and 1995 May 1–3. Polarization modulation was achieved by rotating a parallel mirror and wire grid unit. The spacing between the wire grid and reflector was tuned to provide $\lambda/2$ modulation at the observation wavelength. The observations were performed using position-switching mode with the polarization modulator moved in 16 steps per rotation for both the on-source and off-source positions.

The spectra were binned in ~ 4 km/s wide bins to improve the signal to noise ratio. For each bin of each scan, the normalized Stokes parameters, Q and U , were calculated and the parallactic angle removed. In theory, by using both orthogonal channels simultaneously, polarization dependent sky variations are removed. In practice, one receiver had a lower noise temperature than the other, causing the signal to noise ratio to be lowered when both channels were reduced together. Therefore, the Stokes parameters were calculated and averaged for each receiver independently and then coadded with a weighted average. The polarimetric efficiency was measured by “observing” the polarized calibration noise tube mounted at the secondary mirror of the NRAO 12 m telescope. The observed polarization was nearly 100%, so no corrections for efficiency were applied to the data.

No direct measurement of the systematic instrumental polarization was made with the 3 mm receivers during these observing runs. This is of no concern however, since we do not believe we detected any polarization from any of the molecular outflows. The systematic instrumental polarization of the NRAO 12 m observations is addressed in more detail in Chapters 3 and 6, where detections are reported. Likewise, the position angle indexing is moot since we did not detect polarization, but it is also discussed in Chapter 3.

5.3. Results

The 1995 May flux spectrum and the coadded 1995 May and 1994 June normalized Stokes parameters spectra of DR 21 are plotted in Figure 5.1. Figures 5.2 and 5.3 are the Mon R2 and IRAS16293-2422 spectra. The line averaged polarization for each object is listed in Table 5.1. The second and third columns are the coordinates

of the observations, which were toward the emission peaks of the outflows. Three- σ upper limits are given for Mon R2 and IRAS 16293-2422, and the bias is subtracted from the DR 21 polarization.

We concentrate our analysis on DR 21 because of the high quality HCO⁺ J=1-0 interferometry and H₂ images and spectra available for comparison. The absorption in the flux spectrum at $v_{LSR} \sim 10 \text{ km s}^{-1}$ is due to the intervening cloud W75N (Phillips et al. 1981). The line integrated, normalized Stokes parameters are $Q = -0.0002 \pm 0.0004$ and $U = 0.0024 \pm 0.0004$, with $P = 0.24\% \pm 0.04\%$ and $PA = 47^\circ \pm 5^\circ$. Since Q is nearly zero, $P(\%) = 100 \times (Q^2 + U^2)^{\frac{1}{2}}$, and the PA is nearly 45° , the percentage polarization is well represented by $P(\%) = 100 \times U$. Although this polarization could be intrinsic to DR 21, it is probably dominated by instrumental polarization¹. Therefore, we do not claim it as a detection. What the data clearly demonstrate is that DR 21, Mon R2, and IRAS 16293-2422 do not exhibit significant emission line polarization. Indeed, *the upper limits of the line-integrated polarizations are an order of magnitude less than predicted by the theoretical models.*

¹This is discussed more in Section 6.2 regarding the implications for the observations of IRC+10216.

Table 5.1. Outflow Spectropolarimetry

Source	α_{B1950}	δ_{B1950}	Transition	P(%)	PA(°)
DR 21	20:37:10.5	+42:08:38	HCO ⁺ 1-0	0.24±0.04	47±5
Mon R2	06:05:22.0	-06:23:30	HCO ⁺ 1-0	< 0.4	...
IRAS 16293-2422	16:29:18.7	-24:22:13	CS 2-1	< 1.2	...

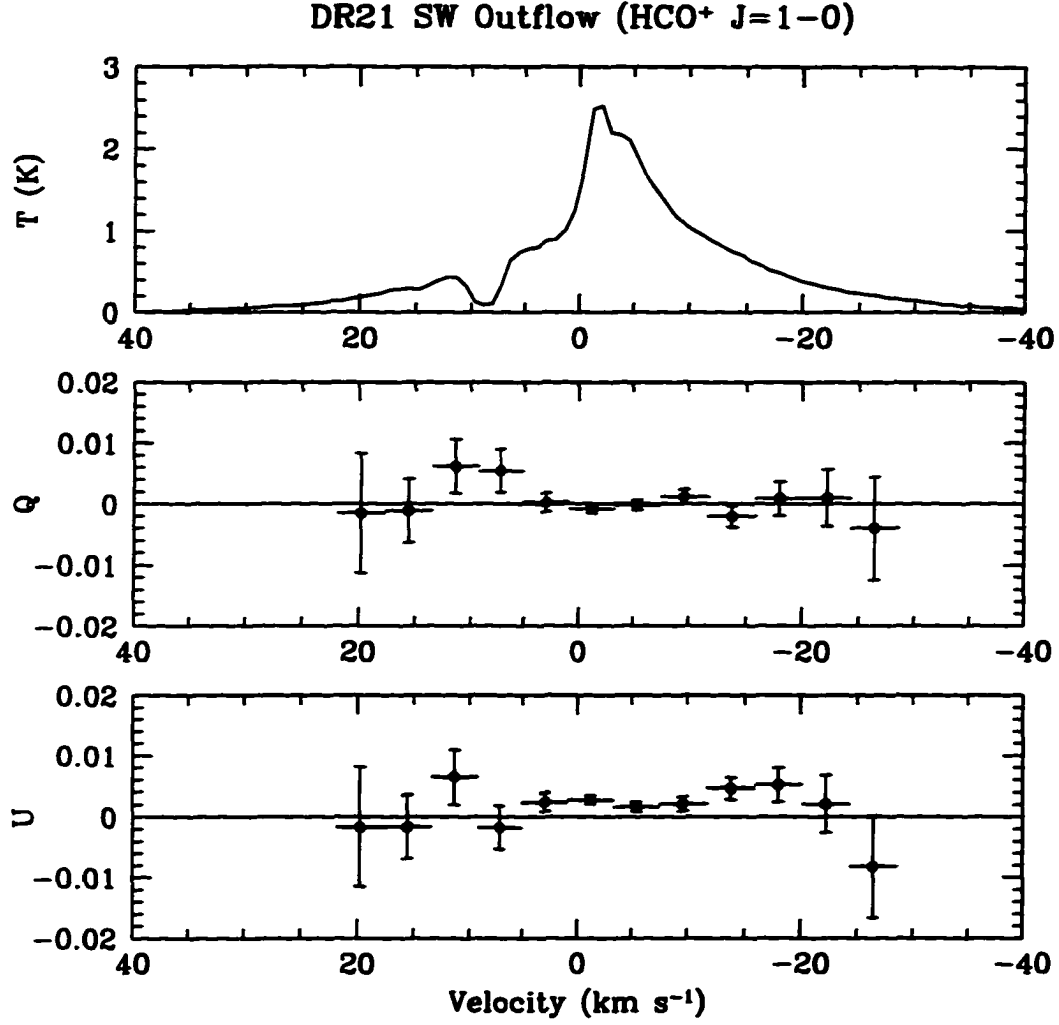


Figure 5.1 $\text{HCO}^+ J = 1-0$ (89.188518 GHz) spectropolarimetry toward the southwestern outflow lobe of DR 21. The top panel is the antenna temperature and the bottom panels are the normalized Stokes parameters Q and U . The error bars denote the 1σ uncertainties and the horizontal lines through the points denote the widths of the bins for each point. For clarity, the data for $v_{\text{lsr}} > 20 \text{ km s}^{-1}$ and $v_{\text{lsr}} < -30 \text{ km s}^{-1}$, which have very large uncertainties, have been omitted.

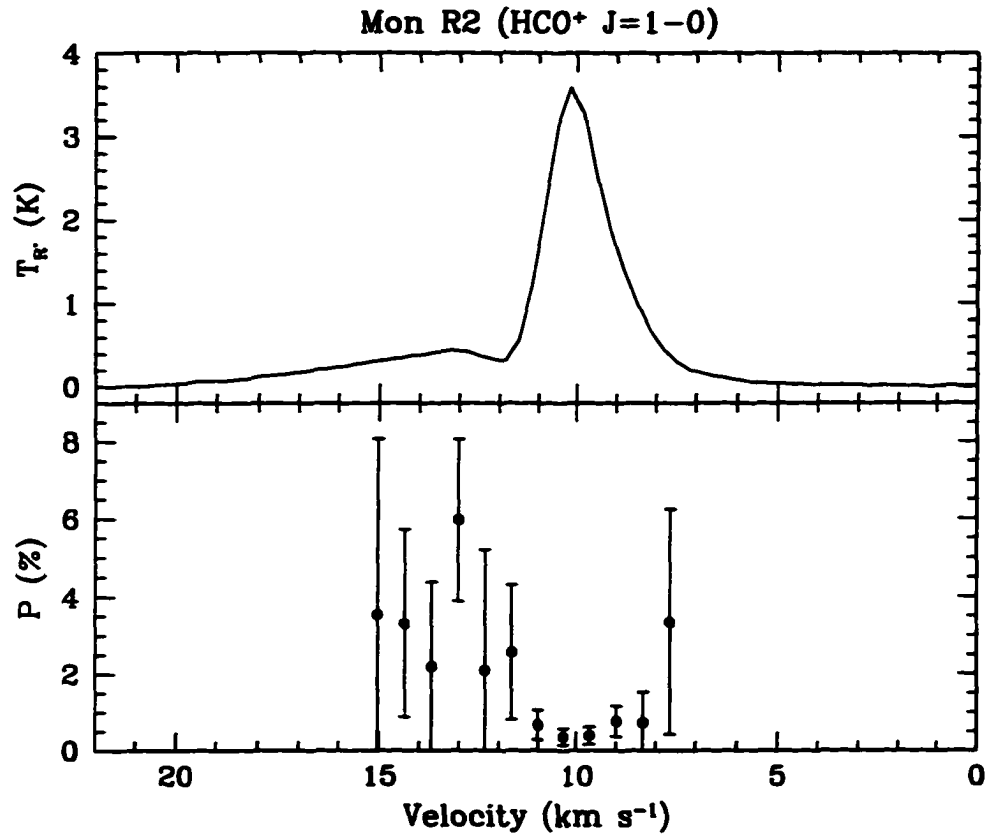


Figure 5.2 $\text{HCO}^+ J = 1-0$ spectropolarimetry of Mon R2. The top panel is the antenna temperature and the bottom panel is the polarization. The error bars are the 1σ uncertainties.

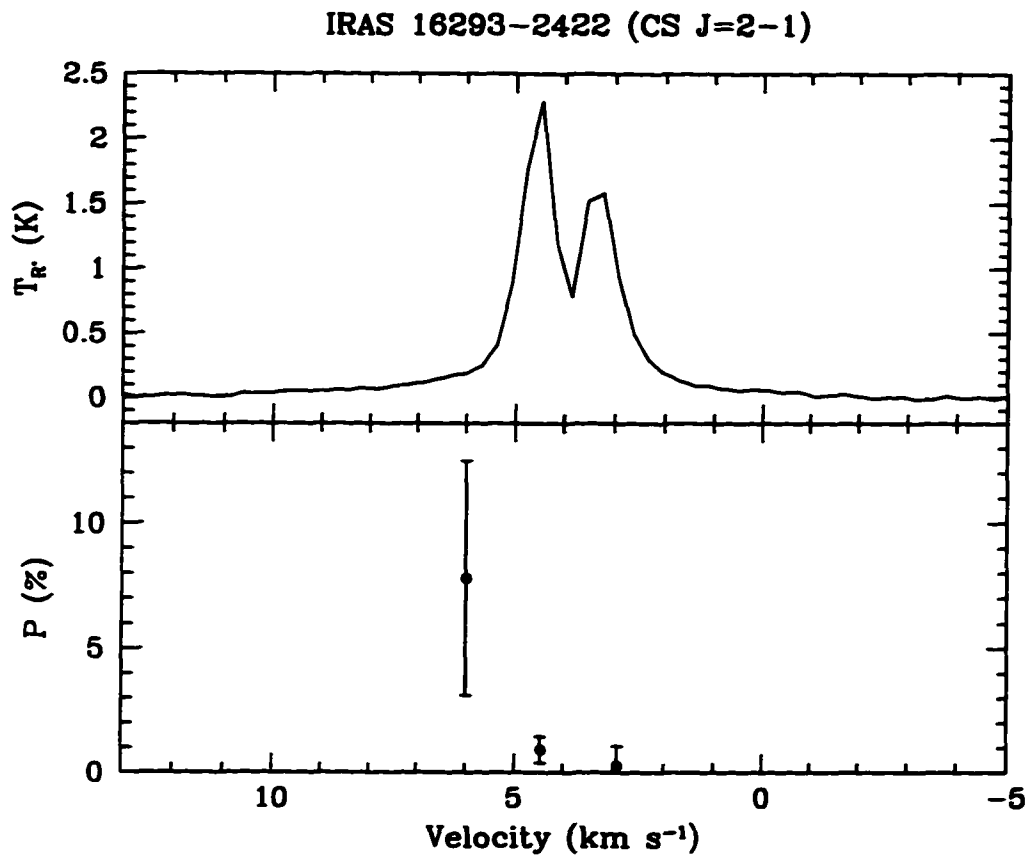


Figure 5.3 CS $J = 2-1$ spectropolarimetry of IRAS16293-2422. The top panel is the antenna temperature and the bottom panel is the polarization. The error bars are the 1σ uncertainties.

The level of polarization is expected to vary through the line because the optical depth presumably decreases from the line center to the line wings. In the case of DR 21, the emission is so strong that polarization can be searched for far into the line wings. We find the upper limit of the polarization is less than the few percent generally predicted by the models at velocities as high as $\sim 25 \text{ km s}^{-1}$ from the line center.

5.4. Discussion

5.4.1. The Lack of Emission Line Polarization

We begin our explanation of the lack of observed polarization in the $\text{HCO}^+ \text{ J}=1-0$ line by analyzing the basic physical assumptions of the models. The relevant basic assumptions of the Goldreich & Kylafis and Deguchi & Watson models are essentially the same: 1) The optical depth in the observed transition is ~ 1 . 2) Radiative decay rates are competitive with collisional deexcitation rates. 3) Systematic velocity differences are much greater than the thermal velocities of molecules, meaning a large velocity gradient model (LVG) is appropriate. In their spherically symmetric models with smooth excitation gradients Lis et al. assume: 1) The molecular transition is optically thin, meaning a single scattering calculation is justified. 2) An excitation gradient is created by a dense core with an envelope in which density decreases with distance from the core. 3) The Zeeman splitting is much less than the Doppler line width and much larger than the natural line width (this corresponds to the strong field limit of the Goldreich & Kylafis model). 4) The magnetic field is either radial or zero. 5) There is a uniform, turbulent velocity dispersion of 1 km s^{-1} FWHM.

The conditions in the DR 21 outflow meet many of the above criteria. Garden

and Carlstrom (1992; hereafter G&C) performed interferometric observations of the core and outflow lobes of DR 21 in the HCO^+ $J=1-0$ transition with a beam of $10.''3 \times 9.''4$. They argue that the HCO^+ $J=1-0$ optical depth is < 1 everywhere within the southwest lobe. Their analysis also shows that the abundance and excitation of HCO^+ varies in the outflow, indicating the optical depth is anisotropic. There are no good estimates of the magnetic field in the DR 21 molecular outflow, but if the local magnetic field strength does not exceed $\sim 100 \mu\text{G}$, the Zeeman splitting will be much smaller than the Doppler width. Finally, based on the moderate optical depths and densities found in the DR 21 outflow by G&C, it is reasonable to expect that the radiative rates are at least competitive with the collisional deexcitation rates in the HCO^+ $J=1-0$ transition.

Emission line polarization at the levels predicted by the models was not observed. Therefore, one or more of the model assumptions must be inappropriate for the DR 21 outflow. One possible reason for a lack of polarization is multiple scattering: for optical depths $\lesssim 1$ single scattering is not strictly satisfied. Also, the polarization will be reduced if the magnetic field lines are not uniform within our beam². The G&C interferometry indicates the HCO^+ distribution is clumpy, which

²Rotation of the outflow could twist the magnetic field lines and reduce the beam-integrated polarization near the protostar (for a review of molecular outflow generation theories see Königl and Ruden 1993). However, beyond the Alfvén radius the inertia of the gas dominates the magnetic field and the wind streamlines should be essentially straight. The Alfvén radius is typically a few stellar radii and our beam was centered on the emission peak of the outflow, $\sim 2 \times 10^5$ AU from the protostar, so it is unlikely that rotation of the outflow leads to the lack of observed polarization.

probably results from the interaction of the outflow with the ambient cloud. If the ion fraction is sufficiently high, the field lines may be jumbled by the gas motions. We believe this clumpy, turbulent distribution is probably the primary factor leading to the small upper limits to the line polarization. A clumpy distribution precludes the smooth velocity or excitation gradient required by the models. The G&C velocity channel maps show that the gas emitting the HCO^+ line in the southwest outflow is in several distinct clumps. These clumps fall within our $70''$ beam and occur over a wide range of velocities (as high as 30 km s^{-1} from the systemic velocity). The clumps become more numerous as the velocity offset nears the systemic velocity, which is consistent with the broad, low-level wing emission we observe in the line. We note that the G&C observations did not include any zero spacing data, and a smooth envelope of outflow emission could be resolved out by the interferometer.

Further evidence for a turbulent, clumpy distribution in the DR 21 outflow that could lead to diminished polarization is provided by H_2 spectroscopy. G&C show the shock excited infrared ($v=1-0$) H_2 line emission is spatially well correlated with the high velocity HCO^+ emission. They argue that the HCO^+ abundance is a factor of 3–10 higher in the shocked gas compared to the ambient gas. Davis and Smith (1996) present additional H_2 $v=1-0$ narrow band images and spectroscopy of the outflow lobes. They find the H_2 emission is clumpy, with clump linear dimensions smaller than $10''$, corresponding to 2% of our beam area. Their spectroscopy revealed that the H_2 emission lines are very asymmetric, with peaks shifting as much as 30 km s^{-1} within the FWHM of our beam. If the HCO^+ emission arises largely from gas with the same spatial and velocity distributions, the LVG model is inappropriate because there are many unresolved velocity gradients within the beam. When integrated by the beam, the polarization produced by summing the

individual clumps would tend to zero. Similarly, the turbulence and clumpiness would wash out the smooth excitation gradients that produce polarization in the Lis et al. model.

If we assume that there are clumped regions of HCO^+ emission with randomly oriented magnetic fields, we can estimate the number of clumps required to reduced the polarization from some theoretical level produced in each clump to the observed beam-averaged polarization of $\sim 0.25\%$. This is easily addressed with a Monte Carlo simulation. The number of clumps needed to reduce the polarization is estimated by converting the polarizations with random position angles to Stokes parameters and averaging them until the coadded polarization drops to 0.25% . The polarization is given by

$$P = \sqrt{\left(\frac{1}{N}\sum Q_i\right)^2 + \left(\frac{1}{N}\sum U_i\right)^2}. \quad (5.1)$$

As $N \rightarrow \infty$, $\langle P \rangle \rightarrow 0$.

Guided by the theoretical polarization models, we assume a polarization of 1% is produced by each clump for one set of simulation runs and 5% for a second set. The algorithm was repeated repeated 1000 times for each polarization. We found $\langle N \rangle = 10$ and $\langle N \rangle = 119$ for $P = 1\%$ and $P = 5\%$, respectively. There are approximately 10-20 resolved clumps of emission in the Davis and Smith (1996) H_2 image. If each clump produces a polarization of $\sim 1\%$ and the magnetic fields are randomly oriented from clump to clump, the beam-averaged polarization is 0.25% , which is consistent with our observations. If instead 5% polarization is produced by unresolved clumps, there must be ~ 120 distinct regions within our beam, indicating the magnetic field must be uncorrelated on scales larger than $3''$, or ~ 0.04 pc. In any case, since at least a dozen clumps are observed, it is possible for a disordered magnetic field in the outflow to reduced the theoretically predicted

polarization to 0.25%.

What optical depth is required to depolarize the line emission by multiple scattering? To make an order of magnitude estimate, we assume the polarization is produced in a region that is surrounded by molecules that scatter the line emission. The observed polarization is given by

$$P_o = \frac{P_i I_i e^{-\tau_s}}{I_t}, \quad (5.2)$$

where P_i is the “intrinsic” polarization produced in the theoretical models, P_o is the observed polarization, τ_s is the line optical depth to scattering, I_i is the intensity of the polarized line emission, and I_t is the total observed intensity. I_t is given by the polarized line emission attenuated by scattering, $I_i e^{-\tau_s}$, plus the line emission scattered into our beam, I_s . We assume that the emission scattered into the beam is unpolarized, however this is only strictly true for a large number of scatterings. We also assume no photons are lost by collisional deexcitation. If the amount of emission scattered into the beam is the same as the amount that is scattered out of the beam, $I_s = I_i(1 - e^{-\tau_s})$, so $I_t = I_i$ and $P_o = P_i e^{-\tau_s}$. For $P_i = 5\%$ and $P_o = 0.25\%$, $\tau_s = 3.1$ and the probability of a photon escaping without scattering is 0.05. For $P_i = 1\%$, $\tau_s = 1.4$ and the probability of a photon escaping without scattering is 0.25. These optical depths correspond to $N \approx \tau^2 + \tau \approx 13$ and 3 scatterings, respectively.

What density is implied by $\tau \geq 1$? In the presence of a velocity gradient, line photons can only scatter within a region over which the velocity changes by only a thermal line width. This is written

$$\left(\frac{dv}{dl} \right) L < v_{th}, \quad (5.3)$$

where L is the size of the region and dl is a differential length. For an assumed kinetic temperature of 30 K (this is the CO excitation temperature, Garden et al.

1991) $v_{th} \sim 0.16 \text{ km s}^{-1}$. The largest $\left(\frac{dv}{dl}\right)$ between neighboring clumps observed by Davis and Smith (1996) is $\sim 3 \text{ km s}^{-1}$. A simple division of the HCO^+ line width from our observations, 80 km s^{-1} , by the beam FWHM, $71''$, is $\sim 1.1 \text{ km s}^{-1}$ per arcsecond. Since equation (5.3) yields an upper limit for L , we choose a conservative 1 km s^{-1} for $\left(\frac{dv}{dl}\right)$. L is then $0.16''$, or $7 \times 10^{15} \text{ cm}$ for a distance of 3 kpc to DR 21. The line optical depth is given by

$$\tau_\nu = \int_0^L \alpha_\nu dl, \quad (5.4)$$

which we set equal to $\alpha_\nu L$, where α_ν is the absorption coefficient. α_ν is given by

$$\frac{h\nu}{4\pi} B_{01} \phi(\nu) n_{0,\text{HCO}^+}. \quad (5.5)$$

n_{0,HCO^+} is the abundance of HCO^+ molecules in the ground rotational state, $B_{01} = 8.6 \times 10^9 \text{ g}^{-1}\text{s}$, and $\phi(\nu)$ is the line profile. For $\tau_\nu > 1$, equations (5.4) and (5.5) can be rearranged as

$$n_{0,\text{HCO}^+} > \frac{4\pi\Delta\nu 10^8}{h\nu B_{01} L}, \quad (5.6)$$

where $\Delta\nu$ is the thermal velocity width of the line, and the fractional abundance of HCO^+ is $\sim 10^{-8}$ relative to H_2 (Garden and Carlstrom 1992). Evaluating equation (5.6) we derive $n_{\text{H}_2} > 1.7 \times 10^3 \text{ cm}^{-3}$. However, not all of the HCO^+ molecules are in the $J = 0$ state. G&C observed the $J = 4-3$ transition of HCO^+ in the southwestern outflow lobe of DR 21. Assuming local thermodynamic equilibrium and only including the $J = 0$ to $J = 4$ states, $< 20\%$ of the HCO^+ molecules are in the ground state. Although LTE may not be appropriate, this is certainly a reasonable upper limit since there are certainly some molecules are excited beyond the $J = 4$ state. Therefore, $n_{\text{H}_2} > 10^4 \text{ cm}^{-3}$ is required for the HCO^+ $J = 1-0$ optical depth to be > 1 in a length scale over which the velocity gradient is smaller than the thermal line width. Since we chose conservatively for $\left(\frac{dv}{dl}\right)$ and the fraction

of HCO^+ molecules in the ground state, $n_{\text{H}_2} > 10^5 \text{ cm}^{-3}$ may be more realistic. A H_2 density of $\sim 10^5 \text{ cm}^{-3}$ was observed in the outflow (Garden et al. 1991) and the $\text{HCO}^+ J = 4-3$ detection of G&C implies the presence of some gas with a density of $> 10^7 \text{ cm}^{-3}$. Consequently, multiple scattering is a feasible mechanism for line depolarization.

The molecular outflow lobes of Mon R2 and IRAS 16293-2422 are not polarized at the level expected from theory. The lack of a few-percent polarization in any of the outflows suggests that molecular outflows, in general, do not have the appropriate characteristics to produce linear polarization in rotational emission lines as observed with large beams. If $\text{HCO}^+ J=1-0$ interferometry and H_2 mapping of Mon R2 were to reveal the same clumpy, turbulent gas distribution as is observed in the DR 21 outflow, further support for our explanation invoking a clumpy outflow with a disordered magnetic field would be provided. Indeed, interferometric maps of the CS $J=2-1$ emission toward IRAS 16293-2422 do indicate the presence of clumpy, turbulent gas entrained in the outflow (Walker et al. 1990). These results suggest a better class of objects in which we should search for emission line polarization would be AGB stars. The expanding shells of gas associated with these objects are often bright in millimeter emission lines and are generally less turbulent than the outflows from young stars.

5.4.2. Magnetic Field Strength in DR 21

If we combine the lack of line polarization with the continuum polarization map of DR 21 from Chapter 3, we can derive an upper limit to the average magnetic field in DR 21. The uniformity of the continuum polarization position angles over the cloud core indicates that the magnetic field lines are ordered along the line of sight throughout the cloud. In contrast, the clumpiness in the post-shock gas

observed by G&C and Davis and Smith (1996), and the lack of HCO^+ polarization, suggest that the field lines could be jumbled in the molecular outflow. Since the line-of-sight averaged DR 21 field is uniform, it is likely that the magnetic field lines in the volume the outflow shock has passed through were aligned with the ambient field lines before the passing of the shock. If the protostellar wind is not smooth or if the ambient, pre-shock gas is clumpy, instabilities could arise when the wind interacts with the ambient material, jumbling the magnetic field lines in the post-shocked gas. If we assume that the lines were ordered and the outflow has disrupted that order, the mechanical energy density of the outflow has to exceed the energy density (magnetic pressure) in the magnetic field orthogonal to the outflow vector. This can be expressed as

$$\frac{B_{\perp OF}^2}{8\pi} < \frac{1}{2}\rho v^2, \quad (5.7)$$

where $B_{\perp OF}$ is the component of the magnetic field strength orthogonal to the outflow (not to be confused with B_{\perp} , the magnetic field component in the plane of the sky in Chapter 3.3.3), ρ is the mass density in the outflow, and v is the outflow velocity. The number density of H_2 in the outflow is $\sim 10^5 \text{ cm}^{-3}$ and a representative outflow velocity is 20 km s^{-1} (Garden et al. 1991). Therefore, the average magnetic field strength in the DR 21 molecular cloud must be less than 4 mG. In Chapter 3, an approximate upper limit of 4 mG was placed on the magnetic field (projected on the plane of the sky) based on the small dispersion in the continuum polarization position angles.

5.5. Summary

An upper limit of 0.4% was placed on the HCO^+ $J = 1-0$ linear polarization from the DR 21 and Mon R2 outflows, and an upper limit of 1.2% was placed on the

IRAS 16293-2422 CS $J = 2-1$ polarization. The polarization of $0.24\% \pm 0.04\%$ in DR 21 is statistically significant, but instrumental polarization may contribute to this. This level of polarization is almost an order of magnitude less than predicted by theoretical models. In the case of DR 21, the lack of polarization could be due to the clumpy, turbulent nature of the outflow. Specifically, if the $\sim 10-20$ clumps resolved in $\text{H}_2 v = 1-0$ observations each produce a polarization of 1% and the magnetic fields are randomly oriented from clump to clump, the beam-integrated polarization could be reduced to the observed level. Multiple scattering may also play a role in diminishing the polarization in the emission lines. By comparing the HCO^+ polarimetry and dust continuum polarimetry, we derived an upper limit of 4 mG for the average DR 21 magnetic field component orthogonal to the molecular outflow vector.

CHAPTER 6

MILLIMETER-WAVE SPECTROPOLARIMETRY OF EVOLVED STARS: EVIDENCE FOR POLARIZED MOLECULAR LINE EMISSION

6.1. Introduction

Radiative transfer models of the extended envelopes of AGB stars predict that the molecular rotational emission lines should be several-percent polarized. In one model (Morris, Lucas, and Omont 1985), molecules in the envelopes are excited by absorption of infrared photons from the central star. This leads to polarization because there is a preferred local rotation axis for the molecules since the exciting

photons impart their angular momentum along the radial direction. Other models that incorporate a smooth velocity gradient in a molecular gas produce an anisotropic optical depth in the Zeeman sublevels of rotational states when coupled with a magnetic field. Such models predict polarization from the winds of evolved stars (Goldreich & Kylafis 1981, 1982, Deguchi and Watson 1984). Because the model envelopes are spherically symmetric, polarization should only be present when the observations of the envelope are pointed away from the central star.

Wannier, Scoville, and Barvainis (1983; hereafter WSB) attempted to observe polarization in CO $J = 1-0$ from IRC+10216. IRC+10216 is a carbon rich star on the asymptotic giant branch (see Sloan and Egan 1995 and references therein). WSB found that the 3σ upper limits on the polarization observed at four positions offset from the central star by $40''$ were $< 1\%$. We observed IRC+10216 in CS $J = 2-1$ (97.981 GHz) both toward the central star and with the beam center pointed $30''$ to the south (IRC+10216 has a spatial extent of $\sim 40''$; Guélin, Lucas, and Neri 1997). The model of Lis et al. (1988) predicts that polarization should be greatest for molecules that have large permanent dipole moments and for which the envelope has a small optical depth. Therefore, although CS emission from IRC+10216 is fainter than CO, its dipole moment is much larger (2.0 vs. 0.1 Debye), and polarization is more likely to be observed.

We also observed the CS $J = 2-1$ and HCN $J = 1-0$ (88.632 GHz) transitions from CRL 2688 to search for polarization. CRL 2688 (the Egg Nebula) is a bipolar protoplanetary nebula with lobes that exhibit high optical polarization from scattering of central star light (Schmidt et al. 1978). CRL 2688 is much fainter than IRC+10216 and has a spatial extent of only $\sim 30''$ in HCN $J = 1-0$ (Bieging and Nguyen-Q.-Rieu 1996). Given the bipolar structure of the envelope there is a

strong possibility of line polarization. We observed HCN toward CRL 2688 because it is brighter than CS $J = 2-1$ and has a high permanent dipole moment of 3.0 Debye.

6.2. Observations and Data Analysis

We made the observations at the NRAO 12-meter telescope using the facility polarimeter and 3-millimeter receivers on June 1–4, 1994, July 9, 1996, and September 24–27, 1996. The polarimeter is described in detail in Emerson, Jewell, and Payne (1995). Polarization was modulated using a wire grid and mirror with a tunable separation based on a design by Prigent and Abba (1988). The separation between the grid and mirror was adjusted to provide $\lambda/2$ modulation at the frequency of observation. We used the orthogonal channels of the dual polarization receivers to observe both senses of polarization simultaneously to reduce our susceptibility to variations in atmospheric transmission and emission. We binned the data into the normalized Stokes parameters, Q and U , for each polarization modulator rotation and averaged the scans¹. The uncertainties in the Stokes parameters were derived from the standard deviations from the means.

¹For the protostar observations reported in Chapter 5, the Stokes parameters were derived from the receivers independently, then coadded. We experienced variable weather during the latter two evolved star observing runs, however, and found that the signal to noise ratios were improved when the Stokes parameters were derived from the simultaneous observations of the orthogonal polarizations. Rereduction of the protostar spectra using the simultaneous measurements did not significantly improve their signal to noise ratios.

Polarization efficiencies and position angle zero point offsets were measured by observing a polarized noise tube mounted on the subreflector of the telescope. The radiation from the noise tube is known to be horizontally polarized to within 4° . Since the observed noise tube polarization was nearly 100%, and therefore the polarization efficiency was nearly 100%, we made no corrections for efficiency to the observed source polarizations. During the September 1996 run we observed the Crab Nebula toward the pulsar repeatedly to check our position angle zeroing and parallactic angle corrections. The Crab has a $\lambda = 3.4$ mm polarization position angle of $\sim 150^\circ$ for beam sizes similar to ours of $70''$ FWHM (see Chapter 4.2 and Barvainis 1984). An average of our entire Crab data set yields a position angle of $155^\circ \pm 2^\circ$. Two degrees have been added to all 1σ position angle uncertainties reported in Tables 6.1 and 6.2 to account for the uncertainty in the position angle indexing.

Because the levels of polarization we observed are so low, it is important that we remove the effects of systematic, instrumental polarization (hereafter IP) from our data. IP can be caused by differing reflectivities of mirrors for orthogonal senses of polarization or by the polarization modulator itself. A constant IP can be measured by observing an unpolarized celestial source: the observed polarization is the IP. The IP can be expressed as an additive term to the normalized Stokes parameters and simply subtracted from the observed Stokes parameters to reveal the real source polarization. Since the polarimeter is reinstalled and removed each observing run, the IP is not expected to be the same on different runs. Consequently, we treated the IP separately for each run.

In June 1994 we observed the molecular outflows of DR 21 and Mon R2 in the HCO^+ $J = 1-0$ transition, and IRAS 16293-2422 in the CS $J = 2-1$ transition

(Chapter 5). We derived line-averaged polarizations of $0.23\% \pm 0.08\%$, $< 0.9\%$, and $< 1.2\%$, respectively, where the latter two are 3σ upper limits. Because we had no direct measurement of the IP, we concluded the apparent detection of polarization toward DR 21 could be partially or completely caused by IP. In order to account for the possibility of IP in the IRC+10216 data, we *assume* that the observed DR 21 polarization is entirely instrumental and subtract it from the IRC+10216 data². The DR 21 polarization is presented in Table 6.1 with and without the parallactic angle removed (the latter case represents the IP and is denoted as “DR 21 IP”). For each polarization in Tables 6.1 and 6.2 for which $P > \sigma_P$, the bias in the polarization (which arises because $P = \sqrt{Q^2 + U^2}$ is a positive definite quantity) was removed approximately with $P = \sqrt{P_{obs}^2 - \sigma_P^2}$ (see e.g., Wardle and Kronberg 1974). Biases were not subtracted from the polarization spectra in Figure 6.1, so those polarizations with large uncertainties are overestimated. Because the parallactic angle subtracted DR 21 polarization is smaller than for the unsubtracted case, the polarization is likely largely systematic and not intrinsic to DR 21³.

There was a pointing problem encountered in the June 1994 run. We

²The IP can be imagined as a fixed vector in the reference frame of the Alt-Az NRAO 12-m telescope. We normally account for sky rotation by removing the parallactic angle from each scan. To estimate the IP from the DR 21 observations, we simply did not remove the parallactic angle from the scans before averaging them.

³DR 21 and IRC+10216 were observed with different receivers. However, the receiver optics preceding the polarization modulator were the same, so the DR 21 observations should be an accurate indicator of the IP.

Table 6.1. Instrumental Polarization

Source	Transition	Date	P (%)	θ (°)
DR 21	HCO ⁺ $J = 1-0$	June 94	0.23 ± 0.08	25 ± 12
DR 21 IP			0.66 ± 0.08	-80 ± 5
Jupiter	continuum	Sept 96	0.05 ± 0.10	...
Jupiter IP			0.24 ± 0.09	59 ± 13
Jupiter (S)			0.26 ± 0.05	59 ± 10
Jupiter IP (S)			0.29 ± 0.07	38 ± 9

Table 6.2. Observations of Evolved Stars

Source	Transition	Date	P (%)	θ (°)
IRC+10216	CS $J = 2-1$	June 94	0.97 ± 0.08	-84 ± 4
IRC+10216 ^a			0.89 ± 0.09	-65 ± 5
IRC+10216		July 96	1.5 ± 0.3	-87 ± 8
IRC+10216 ^b		Sept 96	0.67 ± 0.13	-8 ± 8
IRC+10216 ^{ab}			0.49 ± 0.14	-14 ± 10
IRC+10216(S) ^b			0.6 ± 0.4	11 ± 21
IRC+10216(S) ^{ab}			0.7 ± 0.4	12 ± 18
CRL 2688	HCN $J = 1-0$		$< 0.9(3\sigma)$...
CRL 2688 ^b	CS $J = 2-1$		5.1 ± 1.5	-28 ± 10

^a Instrumental polarization removed.

^b θ may be 90° off.

intended to make two sets of observations: toward the central star of IRC+10216 and 30" north of the central star. Line-averaged polarization was detected in both data sets: $P = 0.73\% \pm 0.13\%$ with $\theta = -75^\circ \pm 7^\circ$ toward the central star and $P = 1.03\% \pm 0.10\%$ with $\theta = -61^\circ \pm 5^\circ$ north of the central star. The line brightnesses, profiles, and polarizations are indistinguishable within the uncertainties for the two data sets, however, implying that the observations were not offset. Further, the peak line brightness temperature from these observations is intermediate ($T \sim 1.5$ K) between our observations toward the central star and 30" south as observed in September 1996 ($T \sim 2.0$ K and $T \sim 1.1$ K, respectively). Consequently, we consider the June 1994 observations together as one set and make no conclusions about polarization structure in the envelope. These data are presented in Figure 6.1 with the systematic polarization removed. The error bars do not include a contribution from the uncertainty in the IP because all the bins are affected equally by the IP subtraction, which does not increase the bin to bin dispersion. The line-averaged polarizations with (denoted "IP") and without the IP subtracted are listed in Table 6.2. The contribution from the IP subtraction has been included in the uncertainties in Table 6.2 where appropriate.

A line-averaged polarization of $P = 1.5\% \pm 0.3\%$ with $\theta = -87^\circ \pm 8^\circ$ was detected during the July 1996 observing run. Because the weather was poor we were unable to measure the IP. Within the uncertainties the polarization and position angle are consistent with the June 1994 observations.

We observed Jupiter in September 1996 to measure the IP. Jupiter is polarized at millimeter and centimeter wavelengths by emission from non-thermal electrons. From a direct linear interpolation of observations of Jupiter's polarization (compiled in Clemens et al. 1990 and Dickel, Degioanni, and Goodman 1970) we should have

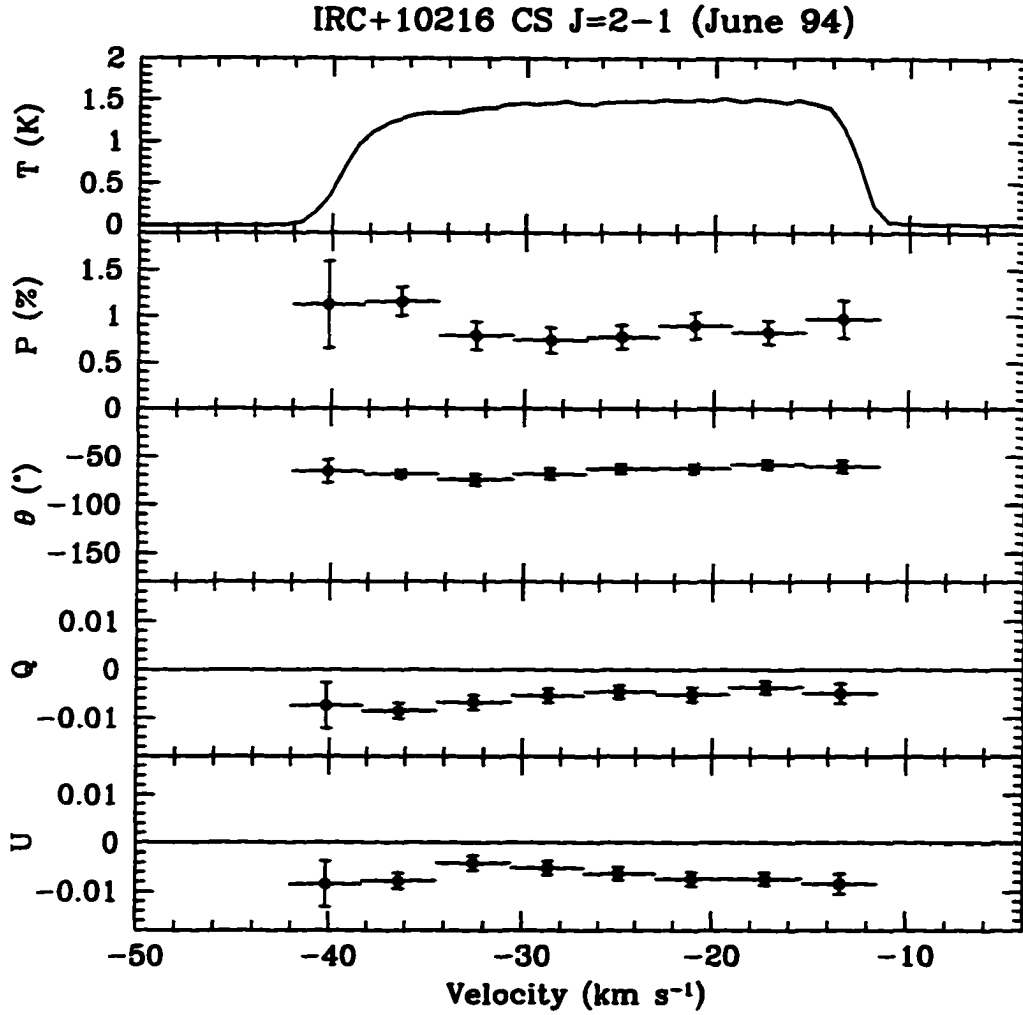


Figure 6.1 CS $J = 2-1$ spectropolarimetry of IRC+10216 from June 1994. The antenna temperature (T_R , as defined by Kutner and Ulich (1981)), normalized Stokes parameters, polarization and position angle are plotted versus the local standard of rest velocity. The error bars are the 1σ uncertainties and the horizontal bars denote the widths of the bins. For clarity, only the bins for which there is sufficient line flux to calculate a meaningful polarization are shown.

observed a polarization of $\sim 0.3\%$. The coadded set of observations reported in Table 6.1 with the parallactic angles removed is listed as “Jupiter” and the coadded set with the parallactic angles not removed (the IP) is reported as “Jupiter IP”. We did not detect polarization toward Jupiter, but our results are statistically consistent with the predicted polarization. We did detect polarization pointed $30''$ south of Jupiter (denoted as “Jupiter (S)”). Not removing the parallactic angles from the observations yields significant detections of polarization both toward Jupiter and $30''$ south, which agree very well. We conclude that the observed polarization of Jupiter is at least partially instrumental and is $\sim 0.3\%$ both on- and off-axis.

Line-averaged polarization was detected toward the central star of IRC+10216 in September 1996, but not $30''$ south of the central star (“IRC+10216 (S)” in Table 6.2). Within the uncertainties, the polarization of IRC+10216 (S) is consistent with the polarization toward the central star. Admittedly this is not a strong test, but we find no evidence for polarization structure in the envelope of IRC+10216. The IP-corrected position angles differ by $\sim 60^\circ$ from the June 1994 IP-corrected and July 1996 angles ($\Delta\theta \sim 85^\circ$ for the IP-uncorrected angles). Given that the emitting region is ~ 5000 AU in extent (for a distance of 180 pc; Herbig and Zappala 1970, Zuckerman, Dyck, and Claussen 1986) and CS $J = 2-1$ is not a masing transition, it is unlikely that the polarization position angle changed by nearly 90° . We did not use our standard backend configuration in September 1996, however, and it is possible the discrepancy in the position angles arose from a misassignment of the orthogonal receivers to the spectral line backends. This would cause a 90° offset in the position angles. It is likely that the detections of polarization toward IRC+10216 are real despite the position angle discrepancy because: 1) The line-averaged polarization is statistically significant in each case,

even after the removal of the IPs. 2) The position angles from June 1994 and July 1996 are consistent. 3) It is unlikely that there is an undiscovered instrumental polarization of 1% because our 3σ upper limits are 0.9% for CRL 2688 in HCN and Mon R2.

The CS $J = 2-1$ 5% polarization observed toward CRL 2688 is barely statistically significant (Figure 6.2). We made no corrections for IP because polarization was not detected in HCN and the IP is smaller than the CS 1σ polarization uncertainty (Figure 6.3).

6.3. Discussion

Why did we detect molecular line polarization since previous attempts have failed? There are three likely reasons: 1) Due to improvements in receiver sensitivity, we achieved uncertainties in the line polarization which are smaller than the uncertainties in previous surveys. 2) We observed IRC+10216 in CS, which has a permanent dipole moment of almost 20 times the dipole moment of CO. Molecules with large permanent dipole moments should exhibit greater polarization than molecules with small dipole moments because radiative decay rates exceed collisional deexcitation rates by a greater factor for large dipole moments. 3) The physical conditions in the extended envelopes of evolved stars might be more conducive to detection of polarization than are molecular clouds. WSB suggested that the lack of polarization seen toward molecular clouds could be due to unresolved kinematics and disordered magnetic field lines. Evidence was presented in Chapter 5 that polarization was not observed toward molecular outflows because the emitting gas is clumpy and has large clump-to-clump velocity dispersions. Unlike molecular outflows from protostars, winds from evolved stars

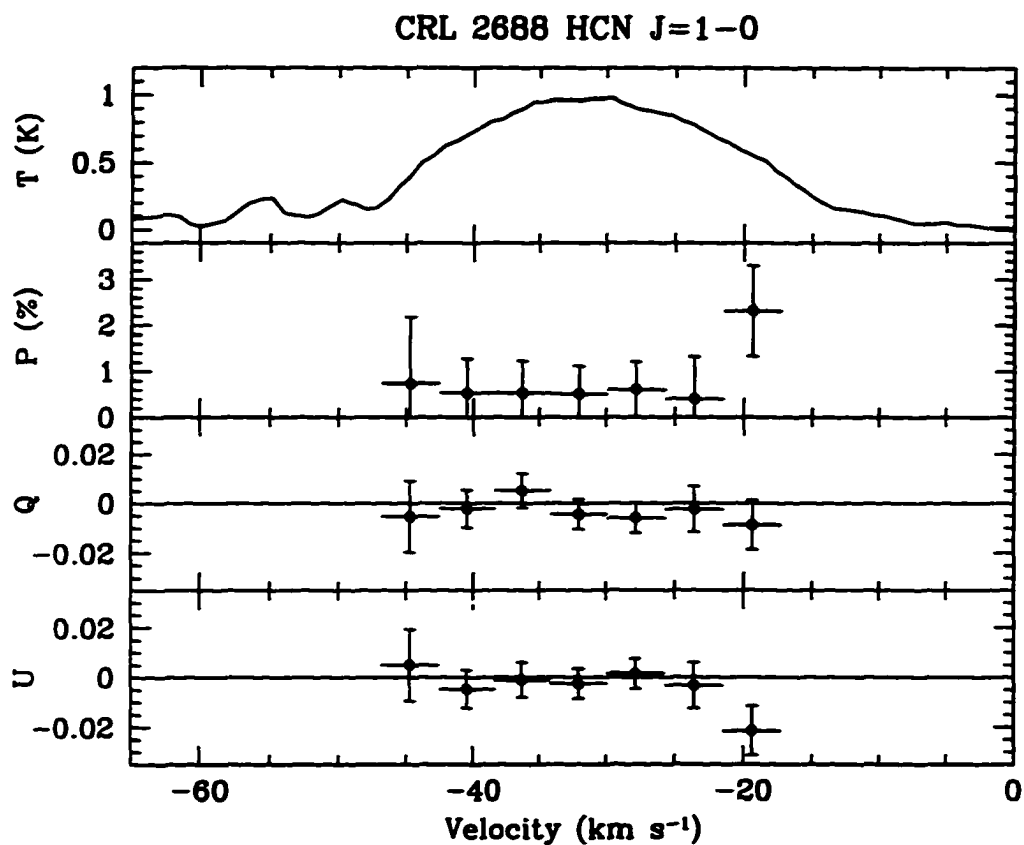


Figure 6.2 HCN $J = 1-0$ spectropolarimetry of CRL 2688. The antenna temperature (T_{R^*} as defined by Kutner and Ulich (1981)), normalized Stokes parameters, polarization and position angle are plotted versus the local standard of rest velocity. The error bars are the 1σ uncertainties and the horizontal bars denote the widths of the bins. For clarity, only the bins for which there is sufficient line flux to calculate a meaningful polarization are shown. The position angle is not plotted since no polarization was detected.

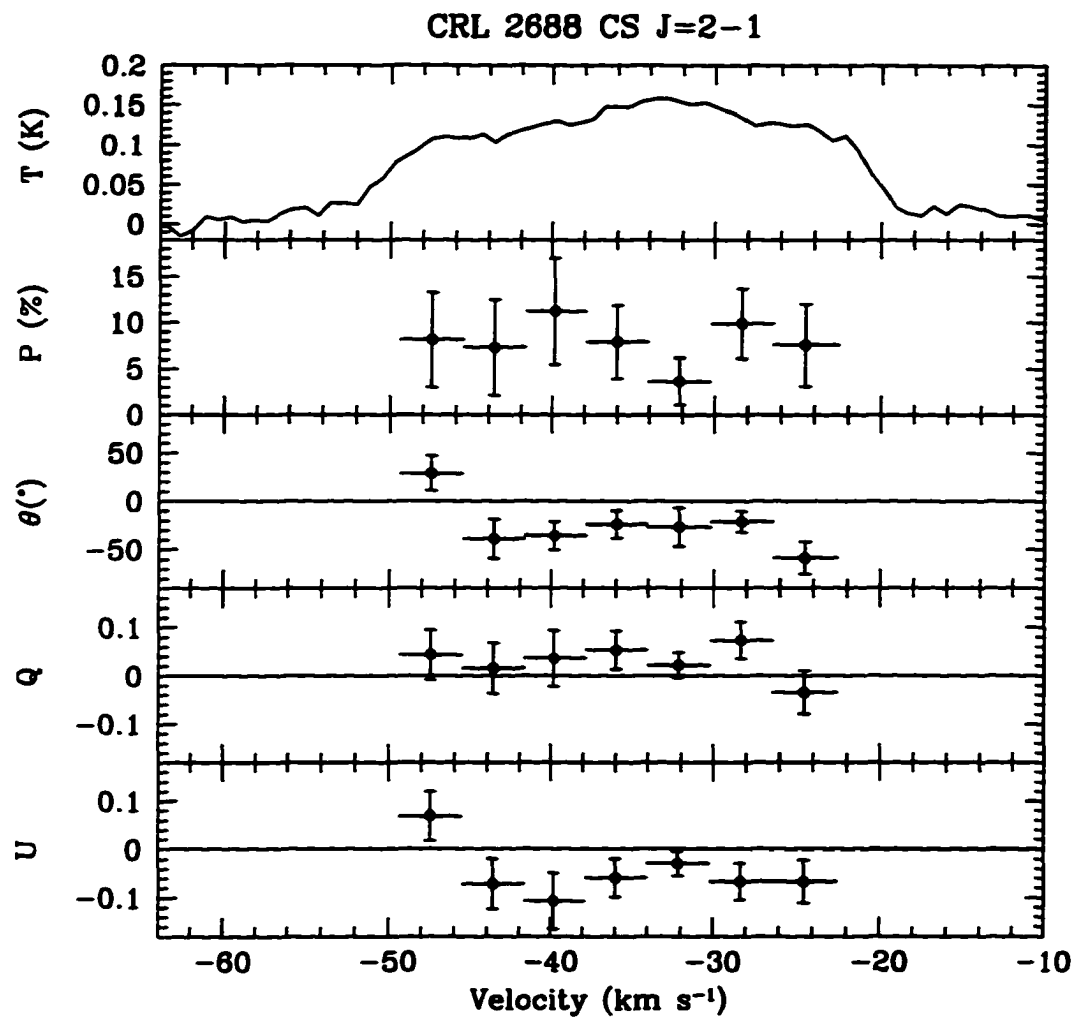


Figure 6.3 CS $J = 2-1$ spectropolarimetry of CRL 2688. The antenna temperature (T_R , as defined by Kutner and Ulich (1981)), normalized Stokes parameters, polarization and position angle are plotted versus the local standard of rest velocity. The error bars are the 1σ uncertainties and the horizontal bars denote the widths of the bins. For clarity, only the bins for which there is sufficient line flux to calculate a meaningful polarization are shown.

are not expanding into a dense interstellar medium. Winds of AGB stars are dominated by radial outflow and show no evidence for large turbulent velocities, so the gas motions are smooth on large scales.

One would expect the polarization percentage to depend on velocity if the optical depth varies with velocity. In our best IRC+10216 data set (from June 1994) we find the average polarization of the four blue-shifted bins in Figure 6.1a is $P = 0.86\% \pm 0.08\%$ with $\theta = -61^\circ \pm 5^\circ$. In the four red-shifted bins $P = 0.93\% \pm 0.13\%$ with $\theta = -69^\circ \pm 6^\circ$. There is no evidence for polarization dependence on velocity.

The $\sim 0.8\%$ polarization observed toward IRC+10216 is small compared to the polarization of several percent predicted by models. If the envelope is spherically symmetric however, no linear polarization should be detected when the observations are pointed directly toward the central star and the magnetic field lines are radial. Therefore, our observations suggest the magnetic field lines are not predominantly radial and/or the envelope is not spherically symmetric.

Is it possible the field lines are not predominantly radial? If the mechanical energy density of the stellar wind exceeds the energy density in the magnetic field (and the gas has a high conductivity), the field line configuration will be dominated by the gas motion, which is predominantly radial. This is satisfied for $\alpha \gg 1$ (Mihalas 1978), where

$$\alpha = \frac{0.5\rho(r)v^2}{B^2(r)/8\pi}. \quad (6.1)$$

$\rho(r)$ is the mass density in the wind, v is the wind velocity, and $B^2(r)/8\pi$ is the energy density of the magnetic field. This can be rearranged in terms of the observable quantities D , the distance to IRC+10216 (~ 180 pc; Herbig and Zappala 1970, Zuckerman, Dyck, and Claussen 1986), \dot{m} , the mass loss rate ($\sim 2 \times 10^{-5}$

$M_{\odot} \text{ yr}^{-1}$ at $D = 180 \text{ pc}$; Knapp 1985), v_t , the terminal velocity of the wind (15 km s^{-1} ; Knapp 1985), and Ω , an angular radius encompassing a substantial fraction of the CS emission ($\sim 10''$; Guélin, Lucas, and Neri 1997):

$$B \ll (\dot{m}v_t)^{\frac{1}{2}}(D\Omega)^{-1}. \quad (6.2)$$

With the observed quantities $B \ll 1.6 \text{ mG}$. So, unless there is a mechanism for magnetic field generation in the envelope or there was an extreme magnetic field at the progenitor main-sequence star's surface (i.e., 10 kG at a radius of $1 \times 10^{13} \text{ cm}$), the geometry of the magnetic field lines will be dominated by the stellar wind and radial in most of the envelope.

There is evidence of asymmetry in the envelope of IRC+10216 from interferometry of molecular gas, and evidence for a disk and asymmetry of the inner envelope from near and mid-infrared observations of dust. Guélin, Lucas, and Neri (1997) found evidence of a symmetry axis at a position angle of $\sim 25^\circ$ in SiS and C_2H . Their map of CS emission is complicated, with an east-west elongated central source and perhaps a ring. Takano, Saito, and Tsuji (1992) observed SiC_2 and found that the intensity is greatest in the northeastern and southwestern parts of the envelope, with a position angle of the maximum intensity of $\sim 40^\circ$. Dayal and Bieging (1995) found that the CN emission has a clump in the southwest part of the envelope and the H^{13}CN emission seems slightly elongated with a position angle of $\sim 15^\circ$. Kastner and Weintraub (1995) found that the dust envelope appears elongated with a position angle of $\sim 20^\circ$. They also found an elliptical symmetry in the J-band polarization and concluded that their polarimetric observations imply the presence of an equatorial disk orthogonal to the nebular elongation. From their $10 \mu\text{m}$ observations of thermal dust emission, Sloan and Egan (1995) concluded that the outer shell is elongated ($2'' \times 4''$) along a position angle of $\sim 25^\circ$. Our

observed CS $J = 2-1$ polarization position angle of $\sim -70^\circ$ is approximately orthogonal to the elongation position angles, which are all similar.

Could asymmetry in the envelope of IRC+10216 be responsible for the CS polarization? With some simplifying assumptions we can estimate the asymmetry required to produce the observed polarization. For simplicity, we divide the envelope into four quadrants on the plane of the sky: the NE, NW, SW, and SE. We further assume the envelope is symmetric about lines from the NE to SW and from the NW to SE. If there is no magnetic field, or a radial magnetic field, then: 1) the polarization position angles of the NE and SW quadrants should be the same, and likewise for the polarization position angles of the NW and SE quadrants, and 2) the NE/SW and NW/SE quadrants should have orthogonal position angles. The observed polarization can then be expressed as

$$P_{obs} = \frac{T_{NE,SW}P_{NE,SW} - T_{NW,SE}P_{NW,SE}}{T_{NE,SW} + T_{NW,SE}}. \quad (6.3)$$

P_{obs} is the observed polarization, $T_{XX,XX}$ are the beam-integrated brightness temperatures of each quadrant, and $P_{XX,XX}$ are the beam-integrated polarizations from each quadrant. Two extremes arise from this equation, with the real case probably a combination of both. For example, if we assume the integrated polarization produced in each quadrant is 5%, we find that $T_{NE,SW} = 1.38T_{NW,SE}$ produces $P_{obs} = 0.8\%$. In other words, if the polarization mechanism works equally throughout the envelope, the emission from two opposing quadrants must be $\sim 40\%$ larger than the other two quadrants. If the brightness temperature is symmetric about the central star, however, then $P_{NW,SE} = P_{NE,SW} + 0.016$ (the polarization produced in two opposing quadrants exceeds the polarization produced in the other quadrants by 1.6%) yields $P_{obs} = 0.8\%$. This could occur naturally in the context of the infrared excitation models of Morris, Lucas, and Omont (1995) if the optical

depth to escape for infrared photons is anisotropic in the inner envelope. The dusty disk proposed by Kastner and Weintraub (1995) could be the source of anisotropy.

CRL 2688 has a well-defined optical bipolar structure with an axis at a position angle of 15° (Ney et al. 1975). Kasuga, Yamamura, and Deguchi (1997) obtained interferometry of CS $J = 2-1$ and found evidence for two concentrations of emission separated by $5''$ along an angle of $\sim 45^\circ$. Bieging and Nguyen-Q.-Rieu (1996) found that there are extensions of HCN emission both along the bipolar structure and along the dark equatorial lane. Because the deviation from spherical symmetry is so well-pronounced compared to IRC+10216, it would not be surprising if the 5% polarization is real. Within the uncertainty the polarization position angle of $-28^\circ \pm 10^\circ$ is nearly orthogonal to the line joining the CS concentrations, however the position angle could be 90° off. The 3σ upper limit of HCN $J = 1-0$ polarization is probably so low compared to the possible CS polarization because the HCN line is optically thick (Dayal and Bieging 1995) and has hyperfine splitting comparable to the velocity width of the line. Both of these conditions could reduce polarization.

Since the large beams of single aperture telescopes may reduce the observed polarizations by beam averaging, a higher level of polarization should be observed with millimeter interferometers. With greater sensitivity to polarization expected from millimeter interferometers, a larger number of objects could be surveyed to improve our understanding of radiative transfer in extended stellar envelopes.

6.4. Summary

The principal results from our polarization observations of evolved stars are:

1) Our observations indicate a $\sim 0.8\%$ polarization from the central star of IRC+10216 in the CS $J = 2-1$ transition. However, the position angle in our third data set is nearly orthogonal to the position angle in previous observations. This discrepancy could be the result of a change in the instrumental setup between observing runs. The CS $J = 2-1$ line from CRL 2688 shows a polarization of 5% at the 3σ level. The HCN $J = 1-0$ line toward CRL 2688 is unpolarized with a 3σ upper limit of 0.9%.

2) There is no evidence for a velocity dependence of the polarization in CS $J = 2-1$ from IRC+10216. The signal-to-noise ratios of the CRL 2688 observations are too low to investigate a velocity dependence.

3) The IRC+10216 CS $J = 2-1$ polarization position angle is approximately orthogonal to the elongation of the envelope.

4) The polarization observed toward the central star of IRC+10216 could be produced by a substantial asymmetry of polarized emission from the envelope or by an optical depth distribution which is anisotropic to escape of infrared photons from the central star, perhaps caused by a toroidal dust distribution. Models of the radiative transfer designed to predict polarization should incorporate the asymmetries observed in the envelope.

CHAPTER 7

CONCLUSIONS AND FUTURE WORK

7.1. Conclusions

The results are listed in detail in the conclusion sections of the chapters. The most significant results of this thesis are:

1. *A 1.3 mm continuum polarimeter, Cyclops, was constructed. A 1σ polarization uncertainty of 0.25% can be achieved toward a 5 Jy/beam source under average, clear observing conditions at the HHT in a few hours of integration time.* This sensitivity is adequate to observe bright star formation regions but not isolated cloud cores undergoing only low mass star formation. The sensitivity is limited primarily by sky noise and secondarily by receiver sensitivity. The systematic polarization of the telescope plus polarimeter is 1.1% and the polarization efficiency is 84%.

2. *A nine point polarization map covering approximately one square arcminute was made toward the DR 21 star formation region with Cyclops. Except for the southernmost point, the polarization percentage and position angle are remarkably constant. The inferred magnetic field lines projected on the plane of the sky are nearly orthogonal to the cloud core elongation as traced by dust emission. Based on the small dispersion in the position angles, an approximate upper limit of the component of the magnetic field in the plane of the sky is 4 mG. Turbulent gas motions are a more significant source of support against self gravity in the molecular cloud core than thermal pressure or magnetic fields.*
3. *The polarization toward the DR 21 cloud core increases slightly with wavelength from $\lambda = 100 \mu\text{m}$ to $\lambda = 2 \text{ mm}$ and is consistent with the standard grain composition of silicates and graphite.*
4. *The continuum polarization observations reported in this thesis were combined with observations reported in the literature. Projected onto the plane of the sky, the magnetic fields of a few of the clouds with simple millimeter dust emission morphologies are nearly orthogonal to their elongations. However, there is no clear tendency for any preferred alignment of cloud core elongations with respect to magnetic field lines, especially for the bright, high mass star forming regions. This confirms that the massive cloud cores are magnetically supercritical, which is expected since stars are forming in the cores. There is possible evidence that the percentage polarization tends to be greater for elongated cloud cores than clouds that are unresolved or not elongated. The magnetic field lines in the clouds appear randomly oriented with respect to the Galactic plane, implying that the random component of*

the Galactic magnetic field dominates the spiral component in this survey.

This is consistent with a trend of increasing disorder in fields from interarm regions, to spiral arms, to molecular cloud cores.

5. *3 σ upper limits of 0.4% and 1.2% were placed on the polarization of the HCO⁺ J=1-0 emission line from the DR 21 and Mon R2 molecular outflows. A 3 σ upper limit of 1.2% was placed on the polarization of the CS J = 2-1 line from the IRAS 16293-2422 molecular outflow. These polarizations are an order of magnitude lower than predicted by theoretical models.* In the case of DR 21, the lack of polarization is probably due to a disordered magnetic field in clumpy, turbulent gas. Multiple scattering may also play a role in diminishing the polarization. If the lack of emission line polarization in the DR 21 outflow is indeed due to a disordered magnetic field within the outflow, an upper limit of 4 mG can be placed on the average magnetic field orthogonal to the outflow.
6. *A CS J = 2-1 polarization of $\sim 0.8\%$ was detected from the envelope of IRC+10216.* A marginally statistically significant CS J = 2-1 polarization of 5% (3 σ) was observed toward CRL 2688. The 3 σ upper limit of the CRL 2688 HCN J = 1-0 polarization is 0.9%. An anisotropic optical depth to the escape of infrared photons from the central star, perhaps caused by a toroidal dust distribution, could generate the IRC+10216 CS polarization.

7.2. Questions That Remain and Strategies to Answer Them

Although there are now polarization observations of thermal dust emission from more than a dozen star formation regions, many questions still remain. Some

of these questions regarding the role of magnetic fields in the dense interstellar medium, and strategies to answer them, are listed below. New telescopes coming on line in the next decade, including SOFIA, the Submillimeter Array, and the proposed Millimeter Array will be well suited to address these issues.

1. Observations indicate that magnetic field lines are typically well ordered in molecular clouds. Do magnetic fields provide substantial anisotropic support against self gravity? A polarization survey of several dozen more cloud cores with a homogeneous set of flux maps is needed to definitively test for correlations between cloud elongations and polarization percentages, and polarization position angles and cloud elongation angles. In particular, the orientation of magnetic fields with respect to cloud elongations should be investigated as a function of cloud core mass.
2. Do magnetic fields help collimate and drive molecular outflows from protostars? Polarization observations with single dish telescopes that detect appreciable flux from envelopes should be compared with interferometric polarization observations that are sensitive to disks. These observations can test if field line orientations are conserved in the infall.
3. Are magnetic fields more important for low mass star formation than high mass star formation? Because they are brighter, primarily high mass star-forming regions have been observed with polarimetry thus far. Observations of low mass protostars require greater sensitivity (e.g., polarized flux uncertainties of < 5 mJy/beam at $\lambda = 1.3$ mm). Although it will have a comparatively small collecting area of 4.9 m^2 , far infrared observations from SOFIA will have excellent sensitivity by virtue of flying above most of the Earth's attenuating atmosphere. Specifically, one could test for a correlation

between magnetic fields and other cloud core and protostar properties toward low mass and high mass protostars separately.

4. Do magnetic field lines in molecular clouds tend to lie in the plane of the Galaxy? Novak (1997) is constructing a submillimeter polarimeter for use at the South Pole where the atmospheric attenuation is minimal. With the large field of view of this instrument it will be possible to map magnetic fields in large sections of the Galactic plane.
5. What are magnetic field strengths in molecular clouds? Observations of both line-of-sight field strengths (from Zeeman splitting) and field lines projected onto the plane of the sky are necessary to construct three dimensional models of magnetic fields.
6. What combinations of grain alignment efficiency, grain composition, grain topology, and magnetic field strength lead to the largely ubiquitous 2% continuum polarization observed from $\lambda = 100 \mu\text{m}$ to $\lambda = 1.3 \text{ mm}$? Complementary near, mid, and far infrared polarimetry can be used to constrain grain alignment efficiencies, compositions, and topologies (Hildebrand and Dragovan 1995).
7. Do the magnetic field lines in spiral galaxies inferred from dust emission observations match the field lines inferred from observations of synchrotron emission? Observations of dust emission probe the dense interstellar medium and observations of synchrotron emission probe the diffuse interstellar medium. Polarization maps of dust in galaxies will require greater resolution and sensitivity than are now available. Typical galaxies have integrated flux densities of $\sim 100 \text{ mJy}$ at a distance of 40 Mpc for $\lambda = 1.3 \text{ mm}$ (Chini et al.

1995). The Submillimeter Array, Millimeter Array, and an array polarimeter on SOFIA are the most realistic opportunities for observing galaxies.

8. Since magnetic field lines are apparently well ordered in molecular clouds, why is the molecular line polarization predicted by models not observed? Models predicting polarization should incorporate random components of gas velocities and magnetic field orientations, as well as multiple scattering.
9. Can we observe the polarization of molecular lines to help us understand radiative transfer in extended stellar envelopes? Contemporary millimeter interferometers equipped with polarimeters, such as the Owens Valley Radio Observatory, have adequate sensitivity and resolution to observe IRC+10216 and CRL 2688. Other AGB stars will require the Millimeter Array. The emission and polarization maps should be compared with models that incorporate asymmetries in envelope radiative transfer to understand the nature of the polarization.

7.3. Cyclops Upgrade

7.3.1. Continuous Waveplate Rotation

The polarization uncertainties derived with Cyclops are about a factor of two larger than expected from the NEFD of the telescope and 1.3 mm bolometer. Additionally, for a given source flux density and atmospheric optical depth, the polarization uncertainties have been observed to vary a factor of several. At millimeter wavelengths the sky opacity varies on time scales of seconds. It takes ~ 2.5 minutes to observe a Stokes parameters set with the current Cyclops observing mode. This suggests that the polarimetry observations are very sensitive

to the stability of the atmosphere and the Stokes parameters should be sampled more rapidly.

The ideal way to minimize sensitivity to atmospheric fluctuations is to observe both senses of polarization simultaneously. However, this would require two bolometers and a wire grid in the same dewar to analyze the polarization. This is impractical for the HHT facility bolometers. Another solution that would improve the S/N of observations is to rotate the waveplate rapidly, i.e. once per second, and coadd successive rotations to derive the polarization. Rotating the waveplate at 60 rpm would modulate the polarization at 4 Hz, thereby reducing the sensitivity to sky variations on timescales longer than 250 ms. Cyclops could be modified to operate in this mode by replacing the stepper motor with a DC motor. With more sophisticated data acquisition software, an optointerrupter and a chopper wheel mounted to the waveplate could trigger the A/D to read a burst of data values many times per waveplate rotation. Alternatively (referring to Figure 2.1), the lock-in amplifier could be retained and an optointerrupter with a 4-tooth chopper wheel mounted to the waveplate could generate the reference signal. In this case, the data acquisition rate from the A/D could be very slow: ~ 1 Hz with a 3 second time constant.

7.3.2. 800 μm to 1300 μm Achromatic Rexolite Half-Waveplate

Because there are an increasing number of multiple wavelength bolometer systems on submillimeter telescopes (SCUBA–Cunningham & Gear 1990, and a 4-color system at the HHT), there is a need for achromatic half-waveplates. Waveplates can be used at room temperature down to a wavelength of $\sim 800 \mu\text{m}$ without creating excessive thermal background. Murray et al. (1996) constructed a room temperature, submillimeter achromatic half-waveplate for the SCUBA instrument

on the James Clerk Maxwell Telescope. Their design is of the Pancharatnam type and uses crystalline quartz. Pancharatnam waveplates (Pancharatnam 1955) are composite waveplates that are constructed of multiple, identical half-waveplates with offset fast axes. Title and Rosenberg (1981) describe a theoretical composite waveplate in which the optical axes of the first and last plates are parallel, and the optical axis of the middle plate is offset from them by 60° .

We designed a composite Rexolite waveplate for use on the HHT. An achromatic waveplate would be particularly useful at the HHT because the facility four color bolometer can be switched back and forth from $800\ \mu\text{m}$ to $1.3\ \text{mm}$ operation in 10 minutes. Observing conditions often change multiple times in the course of a day. $800\ \mu\text{m}$ observations could be made whenever the sky is favorable and $1.3\ \text{mm}$ observations otherwise. With an achromatic waveplate, no optics have to be removed or inserted to switch wavelengths, so only one angle calibration is necessary.

The retardation of a composite waveplate is given by Serkowski (1974):

$$\tau = 2\cos^{-1} \left[\cos\tau_1 \cos(\tau_2/2) - \frac{\sin\tau_1 \sin(\tau_2/2)}{\cos 2c} \right]. \quad (7.1)$$

τ is given by $\pi\nu/\nu_0$, τ_1 is the retardation of the outer plates, τ_2 is the retardation of the central plate, and c is the angle separating the optical axes of the first/third plate and the middle plate. The theoretical retardation is plotted in Figure 7.1. A very high polarimetric efficiency is achieved over almost an octave of wavelength.

A large, clear aperture Rexolite waveplate of composite construction would be easy to fabricate. Machining Rexolite is inexpensive, and all three plates used in the composite would be identical. Since the dielectric constant of Rexolite is 2.51 from $\lambda = 800\ \mu\text{m}$ to $\lambda = 1300\ \mu\text{m}$ (Giles, Gatesman, & Waldman 1990), the groove depth, maximum width, and maximum separation for such a plate would be

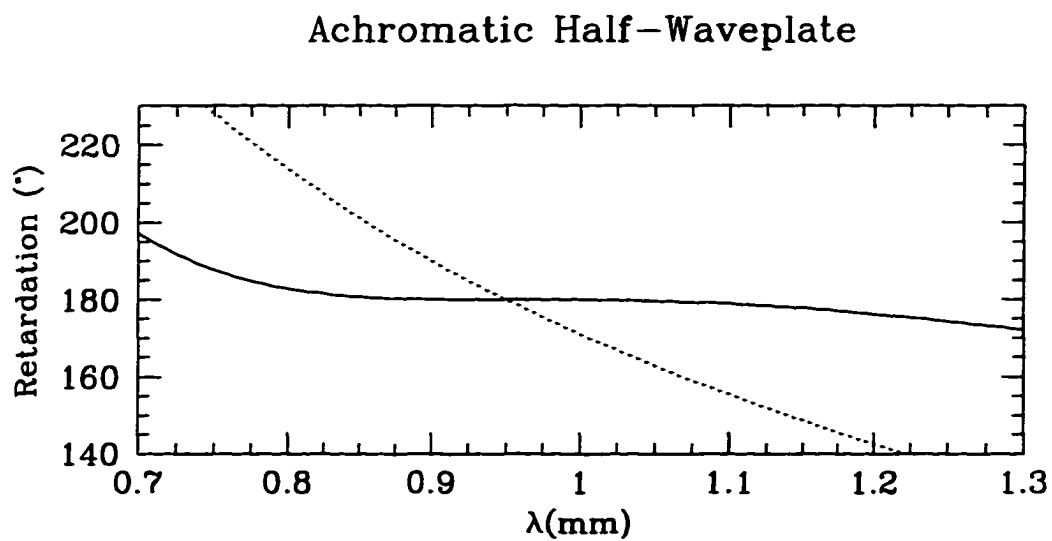


Figure 7.1 Composite Rexolite half-waveplate retardation. The thick solid line is the retardation for an achromatic waveplate optimized for $\lambda = 0.95$ mm. For comparison the retardation for a monochromatic waveplate optimized for $\lambda = 0.95$ mm is plotted as the dashed line.

3.68 mm, 0.32 mm, and 0.32 mm, respectively². Additionally, because the Rexolite blanks can have arbitrary shapes, the substrates could have flanges. Mounting the waveplates together would be done mechanically requiring no polarization inducing, radiation absorbing cements. The total transmission of the composite plate, accounting for reflective and absorptive losses, and with a minimal substrate thickness of ~ 2.5 mm, would be $\sim 75\%$ at $\lambda = 1.3$ mm. At $800\text{ }\mu\text{m}$ the power attenuation coefficient is $\sim .37\text{ cm}^{-1}$, approximately twice that at 1.3 mm (Simonis et al. 1984), and the total transmission would be $\sim 65\%$. The absorption decreases with temperature (Geyer & Krupka 1995) and the transmissions would be $\sim 80\%$ and $\sim 73\%$ at 1.3 mm and $800\text{ }\mu\text{m}$, respectively, at 77 K . We conclude that composite achromatic Rexolite waveplates would be advantageous in that they can be fabricated in large clear apertures inexpensively, but have the disadvantage that they are lossy compared to monochromatic Rexolite plates for $\lambda \leq 800\text{ }\mu\text{m}$.

²Rexolite waveplates are subject to similar requirements as naturally birefringent waveplates to minimize systematic polarization. Platt et al. (1991) provide a thorough discussion of the sources of systematic errors and necessary tolerances of waveplates. Since the grooves are machined, and saw blade wear and frictional heating occur during machining, there are two additional pitfalls particular to Rexolite waveplates. The grooves must be the same depth over the entire plate and the groove thickness cannot vary over the plate. If these conditions are not met, the retardation will vary over the surface of the plate causing unwanted signal modulation when the waveplate is rotated.

APPENDIX A. MIRROR FABRICATION

A.1. Motivation

With the growth in submillimeter astronomy there has been an increase in the need for inexpensive optics. Room temperature lenses are lossy and emit thermal radiation, increasing instrumental background. Since the reflectivity of aluminum exceeds 99% at submillimeter wavelengths, and aluminum is easy to cut and polish, it is an excellent choice for submillimeter optics. To minimize scattering losses, the rms surface accuracy of mirrors should be $\leq \lambda/50$, which is $20\text{ }\mu\text{m}$ at $\lambda = 1\text{ mm}$. The technique described here is based on earlier techniques to cut ellipsoidal and parabolic mirrors. This technique differs from Chamberlain (1993) and Dragovan (1988) in that the mill is commanded by a program with a loop, thereby reducing the program length two orders of magnitude, and no approximations to the surface are made, respectively. The reflective surface shape derivation is based on a similar derivation for parabolic mirrors in Plume, Jaffe, and Wesley (1994).

This technique was used to make mirrors for instruments at the submillimeter South Pole AST/RO telescope and the University of Arizona and Max Planck Institut für Radioastronomie Submillimeter Telescope Observatory.

A.2. Materials

TS6 aluminum is a standard choice for this type of application. It is sufficiently uniform throughout large pieces to make surfaces of high quality. If mirrors are going to be operated at cryogenic temperatures ($T \leq 77\text{ K}$), they can be stress relieved before milling the final surfaces to minimize warping when they are cooled. One method of relieving stresses is to alternately submerge the mirror blank in liquid nitrogen and boiling water. The blank should be kept completely submerged

in liquid nitrogen until the nitrogen stops boiling. Likewise, the blank should be kept in the boiling water until it has reached the water temperature. The transfer time between the nitrogen and water should be as short as possible.

Ball endmills are used to cut the reflective surfaces. Two-flute endmills are best for cutting aluminum because they prevent chips from accumulating on the surface. Endmills of the largest practical diameter are recommended to minimize the deflection of the endmill during cutting.

A.3. Reflective Surface Shape Derivation and CNC Program

CNC mill programming languages are similar to the computer control key stroke sequences used to operate the mill. Some mill control computers are capable of performing only very simple mathematical operations. For example, trigonometric functions, such as sine and cosine, are not always available. Consequently, trigonometric equations must be written in algebraic form. In addition, only one math operation can be performed per line of code. Some controllers are, however, capable of performing loops. The basic algorithm of this technique is (starting from the top of the mirror): 1) calculate the next starting position and arc radius, 2) move the endmill to the start of the arc and make the cut, and 3) repeat steps 1 and 2 until the bottom of the mirror is reached.

The mill setup is displayed in Figure A.1 and the tool path derivation refers to Figure A.2. The endmill cuts an arc of radius equal to the circular cross section radius of the ellipse at each position along the major axis. A correction must be made for the contact point of the endmill, since the contact point is not usually the tip. The following derivation, specifically the expression for θ , is made with the approximation that the endmill radius is much smaller than the radius of curvature

of the mirror. Z refers to the contact point, z is the coordinate of the bottom tip of the endmill, and R is the endmill's radius. $R - R \cos(\theta)$ is the vertical distance between the contact point and the bottom of the tool. From Figure A.2,

$$\theta = \tan^{-1} \left(\frac{dz}{dy} \right). \quad (\text{A1})$$

The vertical coordinate of the contact point is

$$Z = -z + [R - R \cos(\theta)]. \quad (\text{A2})$$

From the equation of an ellipse,

$$\frac{y^2}{a^2} + \frac{z^2}{c^2} = 1, \quad (\text{A3})$$

$$\frac{dz}{dy} = \frac{c^2}{az} \left(1 - \frac{z^2}{c^2} \right)^{\frac{1}{2}}. \quad (\text{A4})$$

So, R_{eff} , the effective radius at which the endmill contacts the aluminum, is given by

$$R_{eff} = R \sin \left\{ \tan^{-1} \left[\frac{c^2}{az} \left(1 - \frac{z^2}{c^2} \right)^{\frac{1}{2}} \right] \right\}. \quad (\text{A5})$$

The radius of the tool path is $r_{arc} = r_{ell} - R_{eff}$, where

$$r_{ell} = a \left(1 - \frac{z^2}{c^2} \right)^{\frac{1}{2}}. \quad (\text{A6})$$

Using the trigonometric identity

$$\cos \left[\tan^{-1}(\alpha) \right] = (1 + \alpha^2)^{-\frac{1}{2}}, \quad (\text{A7})$$

$$r_{arc} = \frac{a^2 z}{c^2} \alpha - R \alpha (1 + \alpha^2)^{-\frac{1}{2}}, \quad (\text{A8})$$

where

$$\alpha = \frac{c^2}{az} \left(1 - \frac{z^2}{c^2} \right)^{\frac{1}{2}}. \quad (\text{A9})$$

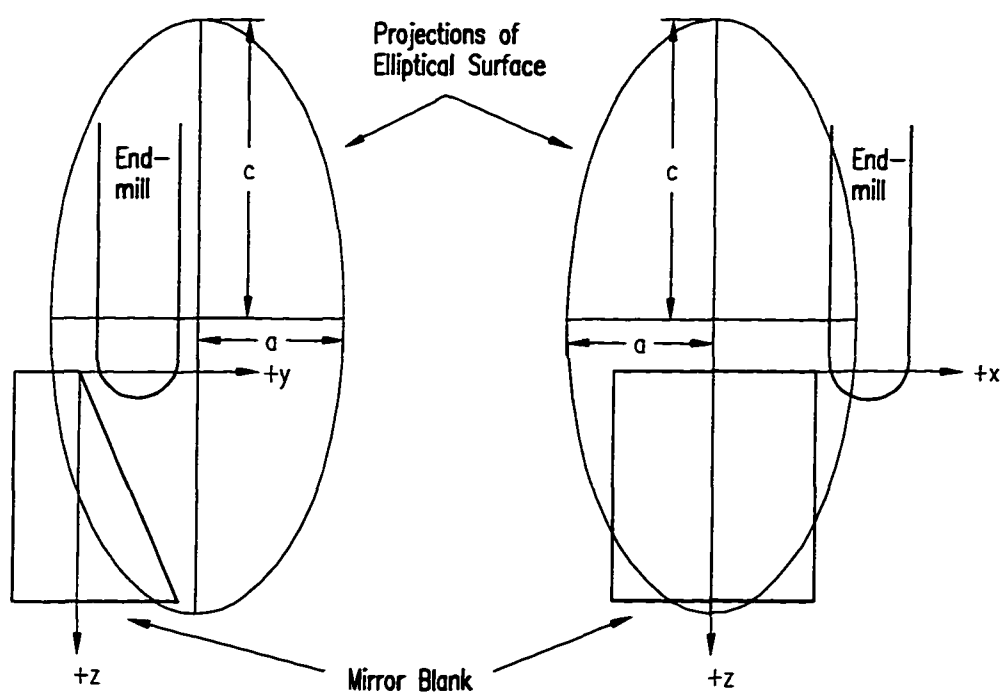


Figure A.1 Setup of the blank on the mill. Views of the left side and front of the mirror blank are shown. Vertical on the figure is vertical on the mill, but the $+z$ axis on the mill is downward. The endmill is shown in the starting position.

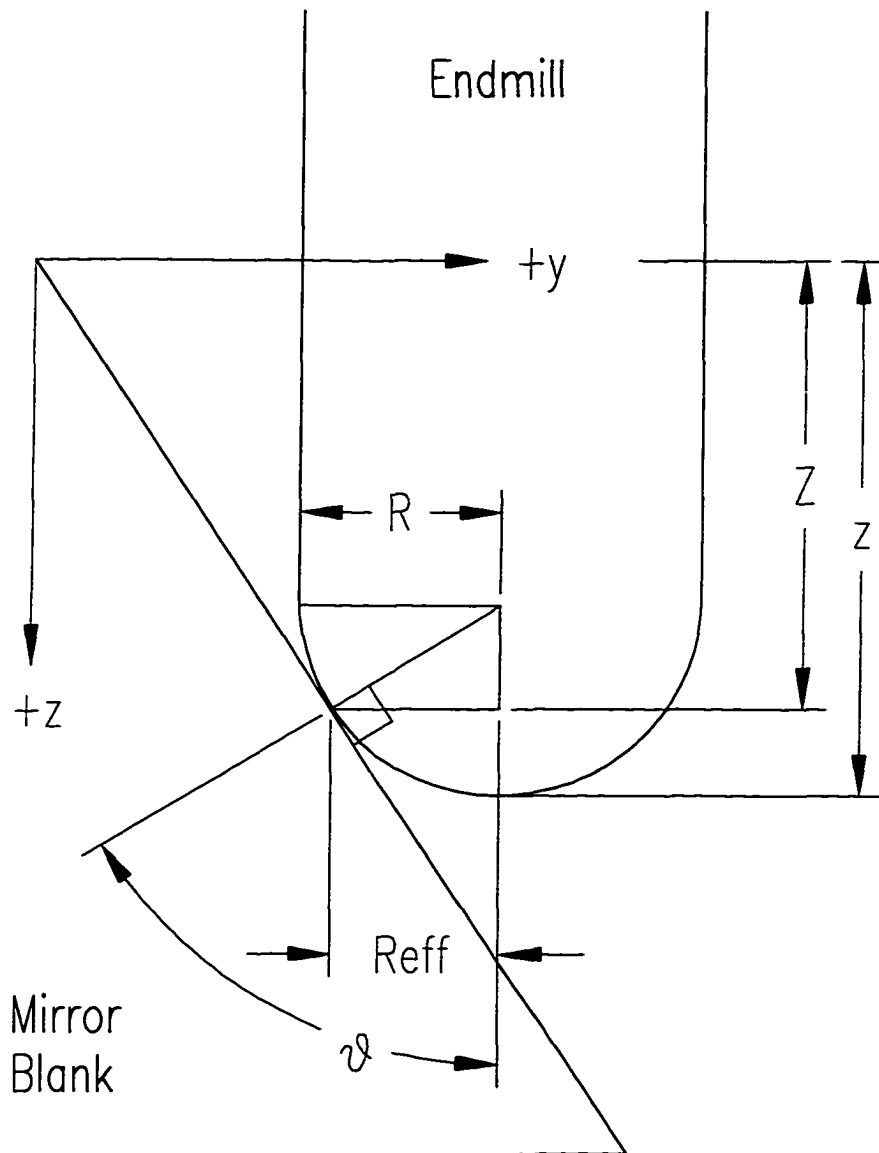


Figure A.2 Schematic for calculating the path of the endmill and correcting for the contact point of the ball endmill.

In terms of α ,

$$Z = -z + R \left[1 - (\alpha^2 + 1)^{-\frac{1}{2}} \right]. \quad (\text{A10})$$

Referring to Figure A.3, the step distance of the mill, d , must be calculated as a function of the target rms. Using the approximation $2 \text{ rms} \equiv R - y$ and the equation of the circle describing the profile of the scallops created by the ball endmill ($x^2 + y^2 = R^2$; where the x - and y -axes are not the same as in Figures A.1 and A.2), the rms is given by

$$\text{rms} = \frac{1}{2} \left[R - (R^2 - x^2)^{\frac{1}{2}} \right]. \quad (\text{A11})$$

With $d = 2x$ this is

$$\text{rms} = \frac{R}{2} - \frac{1}{4}(4R^2 - d^2)^{\frac{1}{2}}. \quad (\text{A12})$$

With $\text{rms} \ll R$, the step distance is given by

$$d \approx 4(R\text{rms})^{\frac{1}{2}}. \quad (\text{A13})$$

The vertical step distance is

$$d_{\text{vert}} \approx 4(R\text{rms})^{\frac{1}{2}} \sin(\theta). \quad (\text{A14})$$

There are a couple practical considerations. First, the ball endmill should have the largest possible radius (a large radius enables large steps, and therefore fewer steps), while still satisfying the requirement that the endmill radius is much smaller than the radius of curvature of the mirror. Second, at least one rough cut should be made before the final cut. Experience has shown that reasonable rough cut and final cut step sizes are 0.15 inches and .025 inches, respectively.

A.4. Testing

A few methods for testing the surface accuracies of mirrors are described below. Paper templates can be cut from AutocadTM drawings and placed against the

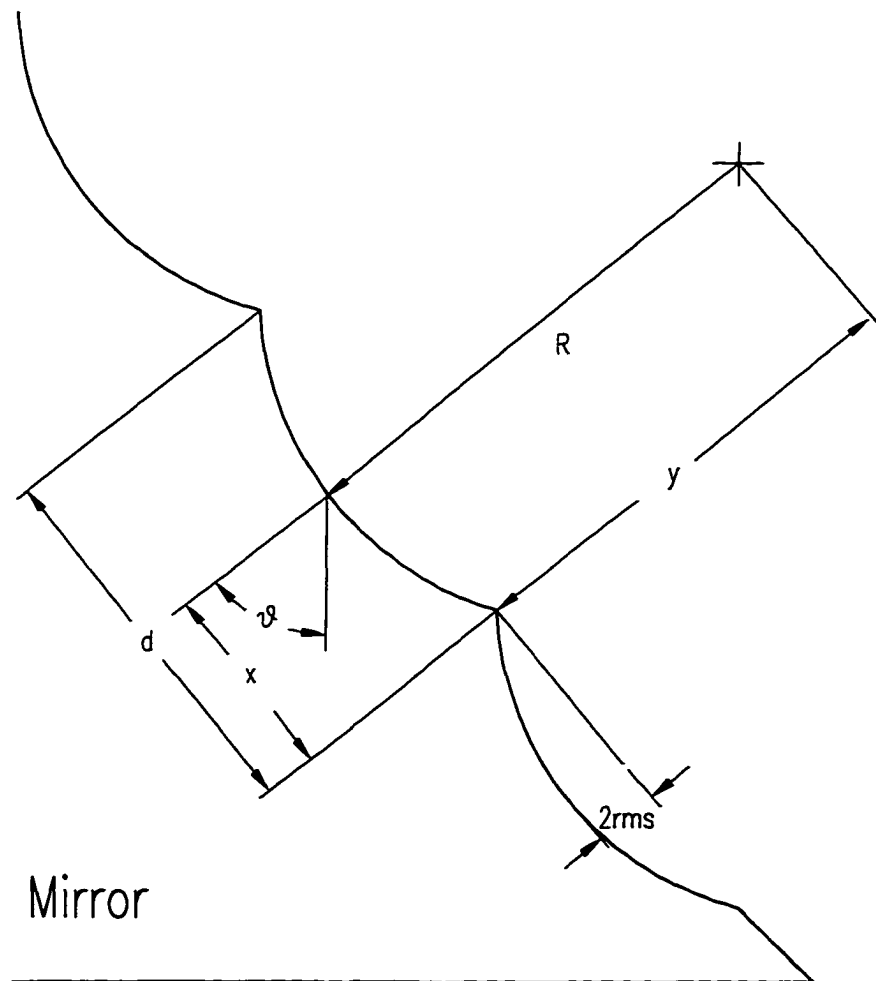


Figure A.3 Schematic for calculating the step distance of the endmill. The rms is “defined” as half of the scallop height. The x and y axes are not the same x and y axes used in the surface shape derivation.

mirror while it is still mounted on the mill. If the printer lines are sufficiently thin the fit can be tested to an accuracy of $250\text{ }\mu\text{m}$. Three templates are useful: 1) a cross section of the ellipse parallel to its major axis, 2) the circular arc perpendicular to the major axis at the top of the mirror, and 3) the circular arc perpendicular to the major axis at the bottom of the mirror.

The surface rms can be determined by comparing points on the surface of the mirror to a theoretical model of the surface. Points on the surface can be measured in three dimensions using the mill itself, a coordinate measuring machine, or by focussing a microscope of sufficiently small depth of focus on the surface. To test the surface of the mirror with a coordinate measuring machine or the mill, a dial gauge can be mounted in the quill and touched down on the surface. Just like cutting with the endmill, the contact point of the dial gauge must be taken into account. To use a microscope with an electronic table, one simply has to focus the microscope on the mirror surface and read the coordinates from the table.

Both deviation of the surface from the theoretical surface and scalloping from the ball endmill contribute to the rms. If the parameters of the model ellipse are allowed to vary, a maximum likelihood algorithm can be used to find the best fit surface for comparison to the theoretical surface. Measurements of the rmss of three mirrors are reported in Table A.1. The lowest rms ($20\text{ }\mu\text{m}$) was achieved with the microscope¹. It is likely that the large rms measured with the CMM resulted from and unintentional deflection of the mirror during the measurement.

¹Vertical grooves with depths $< 25\text{ }\mu\text{m}$ appear near the centers of the mirrors. These arise because there is a small amount of gear lash in the mill and the horizontal motion changes sign in the y -direction at the center of the mirror.

The focal lengths and spot sizes of polished elliptical mirrors can be tested using an incandescent lamp with a small filament. We polished our mirrors with wet/dry sandpaper under running water. Number 600 sandpaper was used first, and small steps were made to number 2000 sandpaper. Mirrors should be polished until they are smooth but not until the scallops are no longer visible. We made the surfaces optically reflective by polishing with SimichromeTM polish. Table A.1 lists the results of testing two mirrors with an incandescent lamp. Δf denotes the offset of the focus from the theoretical position. For both mirrors, the focal lengths were correct within 5 mm, which is the measurement error, and the spot sizes were less than 1 mm in diameter. By moving a mask over the mirror and observing the image, the form of the mirror can be checked.

A.5. Conclusion

In this appendix a technique to fabricate aluminum ellipsoidal mirrors for submillimeter and millimeter wavelengths was described. RMS surface accuracies as low as 20 μm were achieved with respect to the theoretical surfaces.

Table A.1. Mirror Test Results

Mirror #	Surface Test	RMS (μm)	Δf (mm)	Spot Size (mm)
1	Mill	50
1	Microscope	20
1	CMM ^a	175
2	Microscope	35	< 5	< 1
3	< 5	< 1

^aCoordinate measuring machine

REFERENCES

- Akeson, R.L., Carlstrom, J.E., Phillips, J.A., & Woody, D.P. 1996, *ApJ*, 456, L45
- André, P. Ward-Thompson, D., & Barsony, M. 1993, *ApJ*, 406, 122
- Anthony-Twarog, B.J. 1982, *AJ*, 87, 1213
- Barvainis, R.E. 1984, Ph.D. thesis, Univ. of Massachusetts
- Barvainis, R.E., Clemens, D.P., & Leach, R. 1988, *AJ*, 95, 510
- Barvainis, R. & Predmore, C.R., 1984, *ApJ*, 282, 402
- Barvainis, R.E., & Wootten, A. 1987, *AJ*, 92, 168
- Bastien, P. 1996 in A.S.P. Conf. Ser., Vol. 97, Polarimetry of the Interstellar Medium, eds. W.G. Roberge and D.C.B. Whittet (San Francisco: Astronomical Society of the Pacific), 297
- Basu, S., & Mouschovias, T.Ch. 1995, *ApJ*, 453, 271
- Beck, R. 1996 in A.S.P. Conf. Ser., Vol. 97, Polarimetry of the Interstellar Medium, eds. W.G. Roberge and D.C.B. Whittet (San Francisco: Astronomical Society of the Pacific), 475
- Bieging, J.H., & Nguyen-Q.-Rieu. 1996, *AJ*, 112, 706
- Blake, G.A., Sandell, G., van Dishoeck, E.F., Groesbeck, T.D., Mundy, L.G., & Aspin, A. 1995, *ApJ*, 441, 689
- Bonifácio, V.H.R., & Emerson, J.P. 1996 in A.S.P. Conf. Ser., Vol. 97, Polarimetry of the Interstellar Medium, eds. W.G. Roberge and D.C.B. Whittet (San Francisco: Astronomical Society of the Pacific), 363
- Campbell, M.F., Hoffmann, W.F., Thronson, H.A., Jr., Niles, D. Nawfel, R., & Hawrylycz, M. 1982, *ApJ*, 261, 550
- Chamberlain, R. 1993, Oct. 13, AST/RO memo No. 16, A Surface of Revolution Method for Fabrication of Ellipsoidal Mirrors at Boston University
- Chandrasekhar, S., & Fermi, E. 1953, *ApJ*, 118, 116
- Chini, R., Krügel, E., Lemke, R., & Ward-Thompson, D. 1995, *A&A*, 295, 317
- Clemens, D.P., Leach, R.W., Barvainis, R., & Kane, B.D. 1990, *PASP*, 102, 1064
- Colomé, C., Harvey, P.M., Lester, D.F., Campbell, M.F., & Butner, H.M. 1995, *ApJ*, 447, 236

- Cudlip, W. Furniss, I., King, K.J., & Jennings, R.E. 1982, MNRAS, 200, 1169
- Cunningham, C.R. & Gear, W.K. 1990, Instrumentation in Astronomy VII, Proc. SPIE, 1235, 515
- Davis, J., & Greenstein, J.L. 1951, ApJ, 114, 206
- Davis, C.J., & Smith, M.D. 1996, A&A, 310, 961
- Dayal, A., & Bieging, J.H. 1993, ApJ, 407, L31
- Dayal, A., & Bieging, J.H. 1995, ApJ, 439, 996
- Deguchi, S., & Watson, W.D. 1984, ApJ, 285, 126
- Dickel, J.R., Degioanni, J., & Goodman, G. 1970, Radio. Sci., 5, 517
- Dickel, J.R., Dickel, H.R., & Wilson, W.J. 1978, ApJ, 223, 840
- Dowell, C.D. 1997, private communication
- Dowell, C.D., Hildebrand, R.H., Schleuning, D.A., Dotson, J.L., & Novak, G. 1997, ApJ, submitted
- Dowell, C.D., Schleuning, D., & Hildebrand, R.H. 1996, private communication
- Dragovan, M. 1988, Appl. Optics, 27, 4076
- Dragovan, M. 1986, ApJ, 308, 270
- Draine, B.T. 1996 in A.S.P. Conf. Ser., Vol. 97, Polarimetry of the Interstellar Medium, eds. W.G. Roberge and D.C.B. Whittet (San Francisco: Astronomical Society of the Pacific), 1
- Emerson, D.T., Jewell, P.R., & Payne, J.M. 1995 May, NRAO 12 m memo
- Flett, A.M., and Murray, A.G. 1991, MNRAS, 249, 4
- Fuller, G.A., Ladd, E.F., Padman, R., Myers, P.C., & Adams, F.C. 1995, ApJ, 454, 862
- Galli, D., & Shu, F.H. 1993, ApJ, 417, 243
- Garden, R.P., Hayashi, M., Gatley, I., Hasegawa, T., & Kaifu, N. 1991, ApJ, 374, 540
- Garden, R.P., & Carlstrom, J.E. 1992, ApJ, 392, 602
- Geyer, R.G. & Krupka, J. 1995, IEEE Trans. Inst. Meas., 44, 329

- Giles, R.H., Gatesman, A.J., & Waldman, J. 1990, *Int. J. Infrared. Mill. Waves*, 11, 1299
- Glenn, J., Walker, C.K., & Young, E.T., 1996, *International Journal of Infrared and Millimeter Waves*, 18(2), 285
- Gold, T. 1951, *Nature*, 169, 322
- Goldreich, P., & Kylafis, N.D. 1981, *ApJ*, 243, L75
- Goldreich, P., & Kylafis, N.D. 1982, *ApJ*, 253, 606
- Goldsmith, P.F., Lis, D.C., Hills, R. & Lasenby, J. 1990, *ApJ* 350, 186
- Goodman, A.A., Jones, T.J., Lada, E.A., & Myers, P.C. 1995, *ApJ*, 448, 748
- Goodman, A.A. 1996 in *A.S.P. Conf. Ser., Vol. 97, Polarimetry of the Interstellar Medium*, eds. W.G. Roberge and D.C.B. Whittet (San Francisco: Astronomical Society of the Pacific), 325
- Gonatas, D.P., Wu, X.D., Novak, G., & Hildebrand, R.H. 1989, *Appl. Opt.*, 28, 1000
- Gordon, M.A. 1995, *A&A*, 301, 853
- Gordon, M.A., Jewell, P.R., Kaftan-Kassim, M.A., & Salter, C.J. 1986, *ApJ*, 308, 288
- Greaves, J.S., Holland, W.S., & Murray, A.G. 1995, *A&A*, 297, L49
- Greaves, J.S., Holland, W.S., Murray, A.G., & Nartallo, R. 1995, *MNRAS*, 272, L1
- Greaves, J.S., Holland, W.S., and Ward-Thompson, D. 1997, *ApJ*, 480, 255
- Greaves, J.S., Murray, A.G., & Holland, W.S. 1994, *A&A*, 284, L19
- Groesbeck, T.D. 1995, Ph.D. Thesis, Caltech
- Guélin, M., Lucas, R., & Neri, R. 1997, in *IAU Symp. 170*, eds. W. Latter et al., Springer, p.359
- Haese, N.N. & Woods, R.C. 1979, *Chem. Phys. Lett.*, 61, 396
- Harris, S. 1973, *MNRAS*, 162, 5
- Heiles, C. 1996 in *A.S.P. Conf. Ser., Vol. 97, Polarimetry of the Interstellar Medium*, eds. W.G. Roberge and D.C.B. Whittet (San Francisco: Astronomical Society of the Pacific), 457
-

- Henning, Th., Martin, K., Reimann, H.-G., Launhardt, R., Leisawitz, D., and Zinnecker, H. 1994, *A&A*, 288, 282
- Herbig, G.H., and Jones, B.F. 1983, *AJ*, 88, 1040
- Herbig, G.H., and Zappala, R.R. 1970, *ApJ*, 162, L15
- Hildebrand, R.H. 1996 in *A.S.P. Conf. Ser.*, Vol. 97, *Polarimetry of the Interstellar Medium*, eds. W.G. Roberge and D.C.B. Whittet (San Francisco: Astronomical Society of the Pacific), 254
- Hildebrand, R.H. 1988, *QJRAS*, 29, 327
- Hildebrand, R.H. 1983, *QJRAS*, 24, 267
- Hildebrand, R.H., & Dragovan, M. 1995, *ApJ*, 450, 663
- Hildebrand, R.H., Dragovan, M., & Novak, G. 1984, *ApJ*, 284, L51
- Hobson, M.P., Padman, R., Scott, P.F., Prestage, R.M., & Ward-Thompson, D. 1993, *MNRAS*, 264, 1025
- Holland, W.S., Greaves, J.S., Ward-Thompson, D., & André, Ph. 1996, *A&A*, 309, 267
- Kane, B.D., Clemens, D.P., Barvainis, R., & Leach, R.W. 1993, *ApJ*, 411, 708
- Kastner, J.H., & Weintraub, D.A., 1994, *ApJ*, 434, 719
- Kim, S.-H., Martin, P.G., & Hendry, P.D. 1994, *ApJ*, 422, 164
- Kirschbaum, H.S. & Chen, S. 1957, *IRE Trans. on Micro. Th. Tech.*, MTT-5, 199
- Knapp, G.R. 1985, *ApJ*, 293, 273
- Königl, A., & Ruden, S.P. 1993 in *Protostars and Planets III*, eds. E.H. Levy and J.I. Lunine (Tucson: University of Arizona Press), 641
- Kreysa, E. 1996 Oct., private communication
- Kutner, M.L., & Ulich, B.L. 1981, *ApJ*, 250, 341
- Ladd, E.F., Adams, F.C, Casey, S., Davidson, J.A., Fuller, G.A., Harper, D.A., Myers, P.C., & Padman, R. 1991, *ApJ*, 382, 555
- Ladd, E.F., Fuller, G.A., Padman, R., Myers, P.C. & Adams, F.C. 1995, 439, 771
- Lang, K.R. 1990, *Astrophysical Formulae*, 2nd ed., (Berlin: Springer-Verlag), p. 72

- Lay, O.P., Carlstrom, J.E., & Hills, R.E. 1995, *ApJ*, 452, L73
- Leach, R.W., Clemens, D.P., Kane, B.D., & Barvainis, R. 1991, *ApJ*, 370, 257
- Lesurf, J. 1990, *Millimetre-wave Optics, Devices, and Systems*, (Adam Hilder: Bristol), 141
- Lis, D.C., Goldsmith, P.F., Dickman, R.L., Predmore, C.R., Omont, A., & Cernicharo, J. 1988, *ApJ*, 328, 304
- Mathis, J.S., Rumble, W., & Nordsieck, K.H. 1977, *ApJ*, 217, 425
- McCutcheon, W.H., Sato, T., Purton, C.R., Mathews, H.E., & Dewdney, P.E. 1995, *AJ*, 110, 1762
- McKee, C.F., Zweibel, E.G., Goodman, A.A., Heiles, C. 1993, in *Protostars and Planets III*, eds. E.H. Levy & J.I. Lunine, (The University of Arizona Press: Tucson), 327
- Mezger, P.G., Wink, J.E., & Zylka, R. 1990, *A&A*, 228, 95
- Mihalas, D. *Stellar Atmospheres* (New York: W.H. Freeman and Company), p. 535
- Minchin, N.R., Bonifácio, V.H.R., & Murray, A.G. 1996, *A&A*, 315, L5
- Minchin, N.R., & Murray, A.G. 1994, *A&A*, 286, 579
- Minchin, N.R., Sandell, G., & Murray, A.G. 1995, *A&A*, 293, L61
- Morris, M., Lucas, R., & Omont, A. *A&A*, 142, 107
- Mouschovias, T.Ch. 1976, *ApJ*, 207, 141
- Murray, A.G., Ade, P.A.R., & Griffin, M.J. 1996, in *Astron. Soc. Pacific Conf. Ser., Polarimetry of the Interstellar Medium*, eds. Roberge & D.C.B. Whittet, (San Francisco: Astronomical Society of the Pacific), 97, 116
- Nakajima, Y., & Hanawa, T. 1996, *ApJ*, 467, 321
- Ney, E.P., Merrill, K.M., Becklin, E.E., Neugebauer, G., and Wynn-Williams, C.G. 1975, *ApJ*, 198, L129
- Novak, G. 1997, private communication
- Novak, G., Gonatas, D.P., Hildebrand, R.H., & Platt, S.R. 1989, *PASP*, 101, 215
- Novak, G., Predmore, C.R., & Goldsmith, P.F. 1990, *ApJ*, 355, 166

- Oldham, P.G., Griffin, M.J., Richardson, K.J., & Sandell, G. 1994, *A&A*, 284, 559
- Pancharatnam, S. 1955, *Proc. Ind. Acad. Sci.*, A41 130, 137
- Phillips, T.G., Knapp, G.R., Huggins, P.J., Werner, M.W., Wannier, P.G., Neugebauer, G., & Ennis, D. 1981, *ApJ*, 245, 512
- Platt, S.R., Dotson, J.L., Dowell, C.D., Hildebrand, R.H., Schleuning, D., & Novak, G. 1995, in *A.S.P. Conf. Ser.*, Vol. 73, *Airborne Astronomy Symposium on the Galactic Ecosystem*, eds. M.R. Haas, J.A. Davidson, & E.F. Erickson (San Francisco: Astronomical Society of the Pacific), 543
- Platt, S.R., Hildebrand, R.H., Pernic, R.J., Davidson, J.A., & Novak, G. 1991, *PASP*, 103, 1193
- Plume, R., Jaffe, D.T., & Wesley, G. 1994, Mar. 15, UT Austin Department of Astronomy, CNC Construction of Off-Axis Parabolic Mirrors for Submillimeter Wavelengths
- Press, W.H., Teukolsky, S.A., Vetterling, W.T., & Flannery, B.P. 1992, *Numerical Recipes in FORTRAN, The Art of Scientific Computing*, 2nd ed. (Cambridge: Cambridge University Press), 617
- Prigent, C., Abba, P., & Cheudin, M. 1988, *International Journal of Infrared and Millimeter Waves*, 9, 477
- Pudritz, R.E., & Norman, C.A. 1986, *ApJ*, 301, 571
- Purcell, E.M. 1979, *ApJ*, 231, 404
- Richardson, K.J., Sandell, G., & Krisciunas, K. 1989, *A&A*, 224, 199
- Richer, J.S., Padman, R., Ward-Thompson, D., Hills, R.E., & Harris, A.I. 1993, *MNRAS*, 262, 839
- Roberge, W.G. 1996, in *A.S.P. Conf. Ser.*, Vol. 97, *Polarimetry of the Interstellar Medium*, eds. W.G. Roberge and D.C.B. Whittet (San Francisco: Astronomical Society of the Pacific), 401
- Roberts, D.A., Crutcher, R.M., Troland, T.H., & Goss, W.M. 1993, *ApJ*, 412, 675
- Roberts, D.A., Dickel, H.R., & Goss, W.M. 1997, *ApJ*, 476, 209
- Ruzmaikin, A., Sokoloff, D., & Shukurov, A. 1988, *Nature*, 336, 341
- Sandell, G., Aspin, C., Duncan, W.D., Russell, A.P.G., Robson, E.I. 1991, *ApJ*, 376, L17

- Sandell, G. 1994, MNRAS, 271, 75
- Sandford, S.A. 1996, in A.S.P. Conf. Ser., Vol. 97, Polarimetry of the Interstellar Medium, eds. W.G. Roberge and D.C.B. Whittet (San Francisco: Astronomical Society of the Pacific), 29
- Schleuning, D., Dowell, C.D., & Platt, S.R. 1996, in A.S.P. Conf. Ser., Vol. 97, Polarimetry of the Interstellar Medium, eds. W.G. Roberge and D.C.B. Whittet (San Francisco: Astronomical Society of the Pacific), 285
- Schmidt, G.D., Angel, J.R.P., & Beaver, E.A. 1979, ApJ, 227, 106
- Serkowski, K. 1974, in Methods of Experimental Physics, Vol. 12 Part A, Astrophysics, Optical and Infrared, ed. N. Carleton (Academic Press: New York), 361
- Shu, F.H., Adams, F.C., and Lizano, S. 1987, ARA&A, 25, 23
- Shu, F.H., Lizano, S., Ruden, S.P., & Najita, J. 1988, ApJ, 328, L19
- Shu, F.H., Najita, J., Ruden, S.P., & Lizano, S. 1994, ApJ, 429, 797
- Sloan, G.C., & Egan, M.P. 1995, ApJ, 444, 452
- Simonis, G.J., Sattler, J.P., Worchesky, T.L., & Leavitt, R.P. 1984, Int. J. Infrared Mill. Waves, 5, 57
- Snell, R.L., Dickman, R.L., Huang, Y.-L. 1990, ApJ, 352, 139
- Sutton, E.C., Blake, G.A., Masson, C.R., & Phillips, T.G. 1984, ApJ, 283, L41
- Takano, S., Saito, S., & Tsuji, T. 1992, PASJ, 44, 469
- Tamura, M., Hayashi, S.S., Yamashita, T., Duncan, W.D., & Hough, J.H. 1993, ApJ, 404, L21
- Tamura, M., Hough, J.H., & Hayashi, S.S. 1995, ApJ, 448, 346
- Title, A.M & Rosenberg, W.J. 1981, in Polarizers and Applications, Proc. SPIE, 307, 120
- Valleé, J.P., & Bastien, P. 1995, A&A, 294, 831
- Valleé, J.P., & Bastien, P. 1996, A&A, 313, 255
- Vrba, F.J., Strom, S.E., & Strom, K.M. 1976, AJ, 81, 958
- Walker, C.K., Carlstrom, J.E., Bieging, J.H. 1993, ApJ, 402, 655

- Walker, C.K., Carlstrom, J.E., Bieging, J., Young, E.T., and Lada, C.J. 1990, ApJ, 364, 173
- Walker, C.K., Lada, C.J., Young, E.T., and Margulis, M. 1988, ApJ 332, 335
- Wannier, P.G., Scoville, N.Z., & Barvainis, R. 1983, ApJ, 267, 126
- Wardle, J.F.C., & Kronberg, P.P. 1974, ApJ, 194, 249
- Wilking, B.A., Blackwell, J.H., and Mundy, L.G. 1990, AJ, 100, 758
- Wilking, B., Mundy, L., McMullin, J., Hezel, T., and Keene, J. 1993, AJ, 106, 250
- Zuckerman, B., Dyck, H.M., & Claussen, M.J. 1986, ApJ, 304, 401
- Zweibel, E.G. 1996 in A.S.P. Conf. Ser., Vol. 97, Polarimetry of the Interstellar Medium, eds. W.G. Roberge and D.C.B. Whittet (San Francisco: Astronomical Society of the Pacific), 486